

國立交通大學

電信工程研究所

碩士論文

可抑制後波瓣的單一導體帶狀天線之設計

**A Technique for Back Lobe Suppression of  
Single-Conductor Strip Antenna**

研究生：林學群 (Hsueh-Chun Lin)

指導教授：周復芳 博士 (Dr. Christina F. Jou)

中華民國一百零二年六月

可抑制後波瓣的單一導體帶狀天線之設計

**A Technique for Back Lobe Suppression of  
Single-Conductor Strip Antenna**

研究生：林學群

Student : Hsueh-Chun Lin

指導教授：周復芳博士

Advisor : Dr. Christina F. Jou

國立交通大學

電信工程研究所

碩士論文

A Thesis

Submitted to Institute of Communication Engineering

College of Electrical Engineering and Computer Science

National Chiao Tung University

in Partial Fulfillment of the Requirements

for the Degree of

Master of Science

in communication Engineering

June 2013

Hsinchu, Taiwan, Republic of China

中華民國一百零二年六月

# 可抑制後波瓣的單一導體帶狀天線之設計

研究生：林學群

指導教授：周復芳 博士

國立交通大學 電信工程研究所

## 中文摘要

在本論文中，首先介紹了漏波的條件，接著在理論上採用全波分析法-頻域法(spectral domain approach)得到單一導體結構的第一高階洩漏模的傳播常數，其中在空間波輻射頻段，正規化的相位常數非常接近 1，透過洩漏波天線洩漏角度之關係式可得知此天線之主波束(main beam)幾乎固定在端射(end-fire)方向。由於單一導體結構的第一高階洩漏模的基本物理特性為完美電牆(perfect electric wall)中心對稱，表示縱向電流為奇對稱分布而橫向電流為偶對稱分布，所以我們使用平衡式微帶線和反向平衡式微帶線來饋入以激發此模態，並成功地設計出具有高增益與寬頻的單一導體帶狀洩漏波天線。

從此天線的輻射場型圖(radiation pattern)之模擬結果，我們觀察到後波瓣(back lobe)的輻射相當大。在分析了單一導體帶狀洩漏波天線的結構之後，我們推斷出饋入電路中的訊號回流機制會造成向天線左右兩端以及後端的輻射。為了抑制這種現象，我們利用兩個寬頻巴倫(balun)以上下顛倒的方式分別接在饋入電路的左右兩側，而實驗的結果也證實天線的前後輻射比(front-to-back ratio)確實有了明顯的改善(此一構想是將回流路徑中的訊號當作巴倫的輸入訊號，而在兩輸出端可產生大小相同、相位差卻為 $180^\circ$ 的反相訊號，最後將其匯合後來達到抵消的效果，因此向後端福射的效應也隨之減小)。

# A Technique for Back Lobe Suppression of Single-Conductor Strip Antenna

Student: Hsueh-Chun Lin

Advisor: Dr. Christina F. Jou

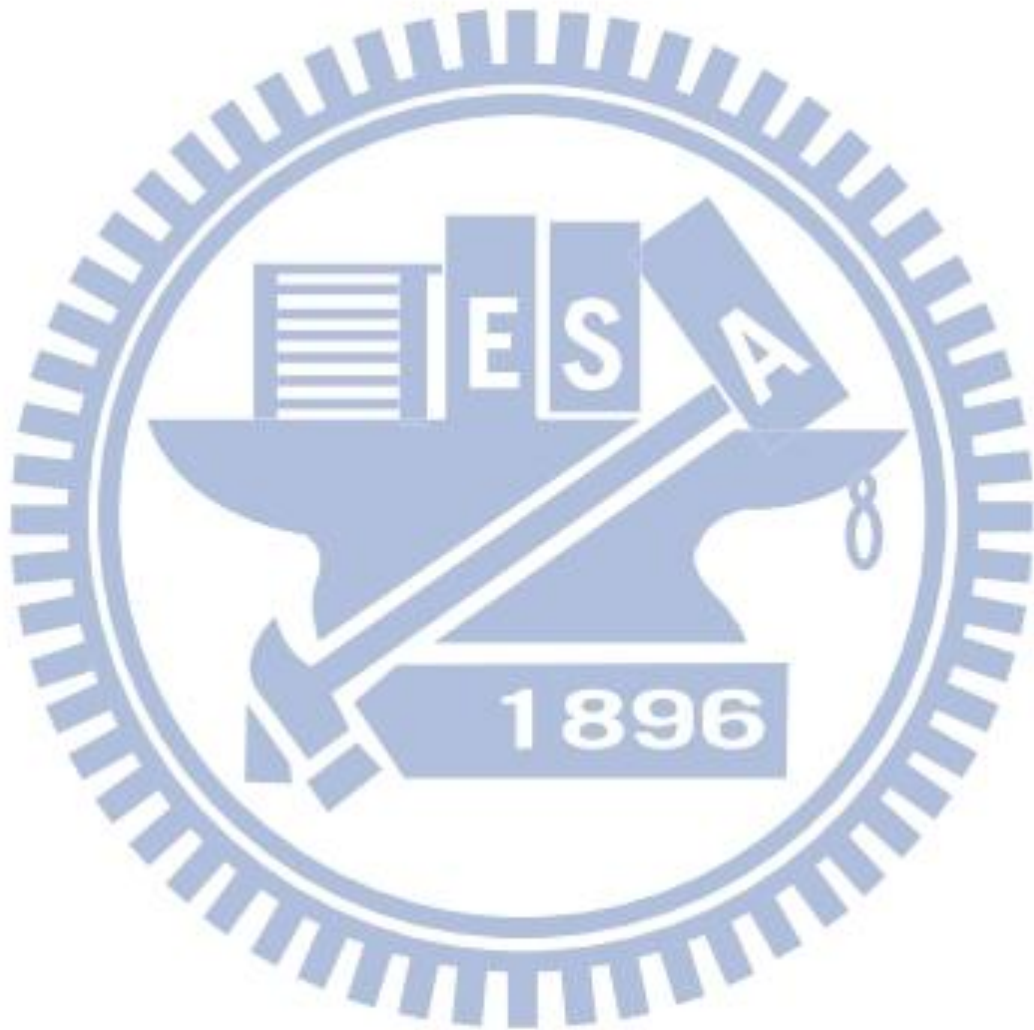
Institute of Communications Engineering  
National Chiao Tung University

## Abstract

This thesis presents the condition of leakage and mode distinction at first; then the well-known full-wave method, spectral domain approach, is applied to investigate the propagation characteristics of the first higher-order mode of the single-conductor strip structure. In this case, the normalized phase constant is very close to 1 in the space-wave leaky region. By the leakage angle equation of leaky-wave antenna, we find that the main beam of this antenna is fixed in the end-fire direction over a broadband region. For the first higher-order leaky mode in this structure, a virtual perfect electric wall is assumed at the center of the strip, this means that the longitudinal currents are odd-symmetric and the transverse currents are even-symmetric with respect to the center. A broadband planar feeding structure based on the balanced microstrip lines and the inverted balanced microstrip lines is developed to feed this single-conductor strip structure and thus excite the first higher-order leaky mode. Then, a high gain and wideband leaky-wave antenna is implemented.

From the radiation patterns of our single-conductor strip leaky-wave antenna, we observe that the back lobe is quite large. After analyzing the single-conductor strip leaky-wave antenna, we conclude that the feeding structure of this antenna causes this undesired effect. In

order to alleviate this undesired radiation from the feeding structure, we turn two broadband planar baluns upside down and attach themselves to the left and right sides of the feeding structure, respectively. Experimental results show significant improvement of the front-to-back ratio of this antenna.



## 誌謝

本論文的完成首先要感謝我的指導教授 周復芳博士，在研究所的求學過程中，提供我一個優良的學習環境，並且當我在研究上遇到瓶頸時，總是能夠適時地給予鼓勵和經驗上的分享，使我得而在兩年內完成碩士研究。同時也要非常感謝 林育德教授，無論在參考文獻上的推薦，或者在數學推導以及數值處理技巧上給我的指導與建議，讓我在微波及天線的領域得到相當多的知識與訓練。再者感謝吳霖堃教授、王健仁教授在口試的時候前來指導，由於他們的寶貴意見才使得本論文更臻完整。特別感謝吳霖堃教授在課餘時間仍不厭其煩地解答我修課上的任何問題。

接著要感謝的是已經畢業的學長奇哲，在研究上提供了很重要的靈感，並且耐心地教會我操作遠場量測室。也感謝奕心在修課時我們時常能互相幫助對方，也會一起討論各自的研究主題。當然還要感謝 925 實驗室的助理薔芸總是在我低潮的時候跳出來幫我打氣，也在實驗室扮演了保姆的角色照顧大家。和你們在碩一相處的這段日子才使得碩士生活變得更加多采多姿。也謝謝學弟昱升、育杰能夠適時地分擔實驗室的工作，讓我能更專心於研究上。

感謝超舜學長、玠瑾學長、政皓學長，無論是在學業上或是生活上給予我的指導與關心。感謝最常和我一起相互砥礪，一起度過許多困難的玠倫。感謝常陪我聊天和運動的學弟政緯。也感謝在 919 實驗室裡一起同甘共苦的各位，因為有你們，在這實驗室裡總是充滿著歡笑，讓我在面對研究壓力之餘，能夠感受到我們是一起奮鬥的夥伴，也讓我更有信心去面對接下來的挑戰。

感謝宜哲學長、正元學長以及科文、則宇等同學在課業和研究上的幫助。還有感謝時常有交集的 916、917 和 923 實驗室的各位學長、同學或學弟，謝謝你們在辦活動的時候總是會算我一份。也謝謝海睿、烜瑋、群明、子峻、觀文、佳龍、立維，你們是我在召喚峽谷上的好戰友。

最後要感謝最支持我的家人，我最親愛的爸爸、媽媽還有兩個姊姊，謝謝你們無條件的支持，讓我沒有後顧之憂地完成學業。

# Contents

中文摘要 .....	I
Abstract.....	II
誌謝.....	IV
Contents.....	V
List of Figures.....	VII
List of Tables.....	XIII
<b>Chapter 1 Introduction</b> .....	1
1.1 Motivation .....	1
1.2 Organization of This Thesis .....	2
<b>Chapter 2 Physical Properties of Leaky Waves</b> .....	3
2.1 Leakage Condition.....	3
2.1.1 Surface-Wave Leaky Mode .....	3
2.1.2 Space-Wave Leaky Mode.....	7
2.2 Mode Distinction .....	8
<b>Chapter 3 Analysis and Numerical Results</b> .....	10
3.1 Space Domain to Spectral Domain.....	10
3.2 SDA on Single-Conductor Strip Structure .....	12
3.2.1 Field Approach .....	12
3.2.2 Choice of Basis Functions .....	17
3.2.3 Method of Solution .....	19
3.2.4 Discussion of Integration Contours .....	21
3.2.5 Numerical Results.....	25

<b>Chapter 4 Antenna Design, Simulation and Measurement</b> .....	28
4.1 Design of Single-Conductor Strip Leaky-Wave Antenna.....	28
4.1.1 Broadband Planar Feeding Structure .....	28
4.1.2 Performance of Single-Conductor Strip Leaky-Wave Antenna.....	35
4.2 Reduction of the Back Lobe .....	44
4.2.1 Consideration during Design Procedure .....	44
4.2.2 Broadband Planar Balun .....	46
4.2.3 Comparison of Simulated Results Between Original and Modified Single-Conductor Strip Leaky-Wave Antenna .....	49
4.2.4 Fabrication and Measurement of Modified Single-Conductor Strip Leaky-Wave Antenna.....	55
<b>Chapter 5 Conclusion and Future Work</b> .....	62
5.1 Conclusion.....	62
5.2 Future Work.....	62
<b>References</b> .....	63
<b>Appendix A</b> .....	65
<b>Appendix B</b> .....	69
<b>Appendix C</b> .....	73
<b>Appendix D</b> .....	74
<b>Appendix E</b> .....	83



## List of Figures

Fig. 2.1	Coplanar waveguide structure.....	4
Fig. 2.2	Top view of a metal strip lying on the substrate, showing the angle $\theta$ of leakage into the surface wave $ks$ on the surrounding substrate. ....	4
Fig. 2.3	A typical dispersion plot for a CPW. For $f > fc$ the mode becomes leaky, in accordance with Eq. (2.3).....	5
Fig. 2.4	Conductor-backed coplanar waveguide structure. ....	6
Fig. 2.5	Dispersion curves of the normalized phase constant of the surface-wave leaky mode for a CBCPW. ....	6
Fig. 2.6	Conductor-backed slotline structure.....	6
Fig. 2.7	The amplitude decays in the $z$ direction ( $b' > a'$ ) due to leakage loss, but in the $x$ direction at a given $z$ , the amplitude increases exponentially ( $b > a$ ).....	6
Fig. 2.8	Microstrip line structure. ....	7
Fig. 2.9	Cross section of a microstrip line.....	7
Fig. 2.10	Radiation leakage in a microstrip line at the air-substrate interface. ....	8
Fig. 2.11	Behavior of the normalized phase constant $\beta k_0$ and the attenuation constant $\alpha k_0$ as a function of frequency for the first higher-order mode of the microstrip line.....	9
Fig. 3.1	Corss-sectional view of a shielded microstrip line. ....	11
Fig. 3.2(a)	Single-conductor strip structure.....	12
Fig. 3.2(b)	Cross-sectional view of a single-conductor strip structure.....	12
Fig. 3.3	Cross-sectional view of a single-conductor strip structure. A virtual perfect electric wall is placed at the center of this structure for the first	

	higher-order mode.....	17
Fig. 3.4	Shapes of basis functions .....	18
Fig. 3.5	Integral paths of the inverse Fourier transform on the $k_x$ plane.....	22
Fig. 3.6	Integral paths of the inverse Fourier transform on the $k_x$ plane.....	24
Fig. 3.7	Behavior of the normalized phase constants and the normalized attenuation constants as a function of frequencies for the first higher order mode of the single conductor strip structure with $\epsilon_r = 3.55$ and $h = 0.508$ mm for different strip widths. ....	25
Fig. 3.8	Behavior of the normalized phase constants and the normalized attenuation constants as a function of frequencies for the first higher order mode of the single conductor strip structure with $w = 40$ mm and $h = 0.508$ mm for different dielectric constants. ....	26
Fig. 3.9	Behavior of the normalized phase constants and the normalized attenuation constants as a function of frequencies for the first higher order mode of the single conductor strip structure with $w = 40$ mm and $\epsilon_r = 3.55$ for different substrate thicknesses. ....	27
Fig. 4.1	An appropriate feeding structure which generates two out-of-phase currents is used to feed the single-conductor strip structure and thus excites the first higher order leaky mode.....	29
Fig. 4.2(a)	Diagram of the broadband balun structure used to excite the first higher order leaky mode of the single-conductor strip line. The strips of the balun on the lower side of the substrate are connected to each other and returned back to the original ground plane of the microstrip line. This feeding structure consists of (I) a conventional microstrip line; (II) a microstrip-to-balanced-microstrip-line transition; (III) a balanced-microstrip-line T-junction power divider and (IV) one set of	

the balanced microstrip lines is changed to form the inverted balanced microstrip lines. ....	30
Fig. 4.2(c) The strip of the balun on the lower side of the substrate. ....	30
Fig. 4.2(b) The strip of the balun on the upper side of the substrate. ....	30
Fig. 4.3(a) Gradually tapering the ground plane to a width equal to the strip width $w$ makes conventional microstrip line a balanced microstrip line.....	31
Fig. 4.3(b) Cross-sectional view of a balanced microstrip line, with a strip of positive voltage on the upper side of the substrate and a strip of negative voltage on the lower side of the substrate. ....	31
Fig. 4.4(a) Top view of the inverted balanced microstrip line.....	32
Fig. 4.4(b) The width of the bent stubs: $Wm = 1.35$ mm; the length of the bent stubs: $lup = 0.9$ mm and $ldn = 0.9$ mm; the gap width: $lgp = 0.13$ mm; the diameter of vias: $rv = 0.3$ mm; the slanted angle is 45 degrees.....	33
Fig. 4.4(c) Signal flow graph of the inverted balanced microstrip line.....	33
Fig. 4.5 Two pairs of the broadband planar baluns on the upper and lower substrate sides, respectively. ....	34
Fig. 4.6 Geometry of the single-conductor strip leaky-wave antenna.....	35
Fig. 4.7(a) Side view of the broadband planar feeding structure. ....	36
Fig. 4.7(b) Top view of the broadband planar feeding structure. ....	36
Fig. 4.8(a) Simulated S-parameter magnitudes of the broadband planar feeding structure. ....	37
Fig. 4.8(b) Simulated phase difference of the broadband planar feeding structure...	37
Fig. 4.9 Normalized propagation constant of the single-conductor strip structure with a strip width of $w = 32.5$ mm, a dielectric constant of $\epsilon_r = 3.55$ , and a thickness of $h = 0.508$ mm. ....	38
Fig. 4.10 Simulated return loss of the single-conductor strip leaky-wave antenna.	39

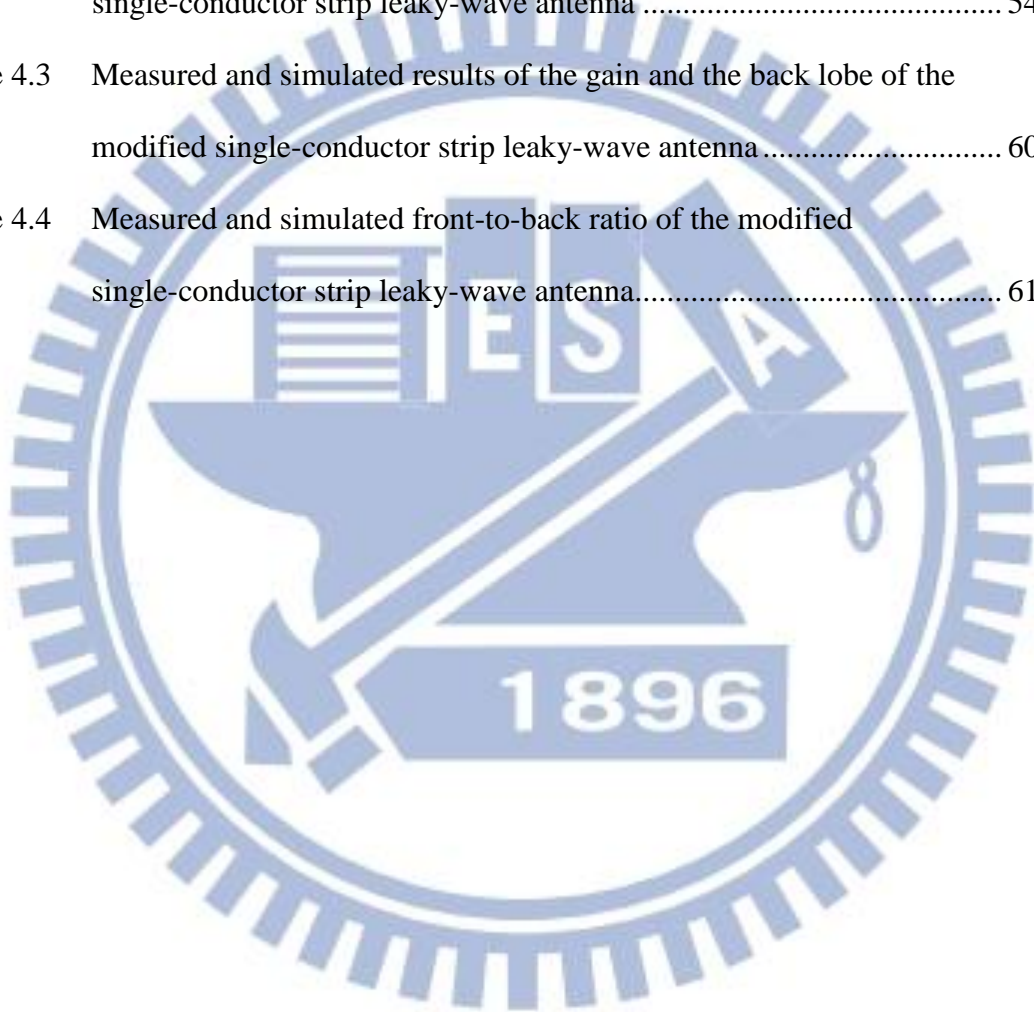
Fig. 4.11(a) Simulated E-plane ( $x$ - $y$ plane) radiation pattern of the single-conductor strip leaky-wave antenna with a gain of 6.24 dBi at 5.2 GHz. ....	40
Fig. 4.11(b) Simulated H-plane ( $y$ - $z$ plane) radiation pattern of the single-conductor strip leaky-wave antenna at 5.2 GHz. ....	40
Fig. 4.11(c) Simulated E-plane ( $x$ - $y$ plane) radiation pattern of the single-conductor strip leaky-wave antenna with a gain of 6.96 dBi at 5.4 GHz. ....	41
Fig. 4.11(d) Simulated H-plane ( $y$ - $z$ plane) radiation pattern of the single-conductor strip leaky-wave antenna at 5.4 GHz. ....	41
Fig. 4.11(e) Simulated E-plane ( $x$ - $y$ plane) radiation pattern of the single-conductor strip leaky-wave antenna with a gain of 7.23 dBi at 5.6 GHz. ....	42
Fig. 4.11(f) Simulated H-plane ( $y$ - $z$ plane) radiation pattern of the single-conductor strip leaky-wave antenna at 5.6 GHz. ....	42
Fig. 4.11(g) Simulated E-plane ( $x$ - $y$ plane) radiation pattern of the single-conductor strip leaky-wave antenna with a gain of 7.51 dBi at 5.8 GHz. ....	43
Fig. 4.11(h) Simulated H-plane ( $y$ - $z$ plane) radiation pattern of the single-conductor strip leaky-wave antenna at 5.8 GHz. ....	43
Fig. 4.12 Surface current in the current returning paths in the ground plane. ....	44
Fig. 4.13(a) Top view of the modified single-conductor strip leaky-wave antenna. ....	45
Fig. 4.13(b) Back view of the modified single-conductor strip leaky-wave antenna. ....	45
Fig. 4.14(a) Two microstrip-to-slotline transitions connected back-to-back for $180^\circ$ phase change and (b) mechanism for $180^\circ$ phase change. ....	46
Fig. 4.15(a) Top view of the broadband planar balun. ....	47
Fig. 4.15(b) Back view of the broadband planar balun. ....	47
Fig. 4.16(a) Simulated S-parameter magnitudes of the broadband planar balun. ....	48
Fig. 4.16(b) Simulated phase difference of the broadband planar balun. ....	48
Fig. 4.17 Comparison of the simulated surfaces current in the current returning	

paths in the ground plane between the original and the modified single-conductor strip leaky-wave antenna. ....	49
Fig. 4.18(a) Comparison of the simulated E-plane ( $x$ - $y$ plane) radiation patterns between the original and the modified single-conductor strip leaky-wave antenna at 5.2 GHz. ....	50
Fig. 4.18(b) Comparison of the simulated E-plane ( $x$ - $y$ plane) radiation patterns between the original and the modified single-conductor strip leaky-wave antenna at 5.3 GHz. ....	50
Fig. 4.18(c) Comparison of the simulated E-plane ( $x$ - $y$ plane) radiation patterns between the original and the modified single-conductor strip leaky-wave antenna at 5.4 GHz. ....	51
Fig. 4.18(d) Comparison of the simulated E-plane ( $x$ - $y$ plane) radiation patterns between the original and the modified single-conductor strip leaky-wave antenna at 5.5 GHz. ....	51
Fig. 4.18(e) Comparison of the simulated E-plane ( $x$ - $y$ plane) radiation patterns between the original and the modified single-conductor strip leaky-wave antenna at 5.6 GHz. ....	52
Fig. 4.18(f) Comparison of the simulated E-plane ( $x$ - $y$ plane) radiation patterns between the original and the modified single-conductor strip leaky-wave antenna at 5.7 GHz. ....	52
Fig. 4.18(g) Comparison of the simulated E-plane ( $x$ - $y$ plane) radiation patterns between the original and the modified single-conductor strip leaky-wave antenna at 5.8 GHz. ....	53
Fig. 4.19 Comparison of the simulated front-to-back ratio between the original and the modified single-conductor strip leaky-wave antenna. ....	54
Fig. 4.20(a) Top view of the fabricated modified single-conductor strip leaky-wave	

antenna. ....	55
Fig. 4.20(b) Back view of the fabricated modified single-conductor strip leaky-wave antenna. ....	55
Fig. 4.21 Measured and simulated return loss of the modified single-conductor strip leaky-wave antenna. ....	56
Fig. 4.22(a) Measured and simulated E-plane ( $x$ - $y$ plane) radiation patterns of the modified single-conductor strip leaky-wave antenna at 5.2 GHz.....	57
Fig. 4.22(b) Measured and simulated E-plane ( $x$ - $y$ plane) radiation patterns of the modified single-conductor strip leaky-wave antenna at 5.3 GHz.....	57
Fig. 4.22(c) Measured and simulated E-plane ( $x$ - $y$ plane) radiation patterns of the modified single-conductor strip leaky-wave antenna at 5.4 GHz.....	58
Fig. 4.22(d) Measured and simulated E-plane ( $x$ - $y$ plane) radiation patterns of the modified single-conductor strip leaky-wave antenna at 5.5 GHz.....	58
Fig. 4.22(e) Measured and simulated E-plane ( $x$ - $y$ plane) radiation patterns of the modified single-conductor strip leaky-wave antenna at 5.6 GHz.....	59
Fig. 4.22(f) Measured and simulated E-plane ( $x$ - $y$ plane) radiation patterns of the modified single-conductor strip leaky-wave antenna at 5.7 GHz.....	59
Fig. 4.22(g) Measured and simulated E-plane ( $x$ - $y$ plane) radiation patterns of the modified single-conductor strip leaky-wave antenna at 5.8 GHz.....	60
Fig. 4.23 Comparison of the measured and simulated front-to-back ratio of the modified single-conductor strip leaky-wave antenna. ....	61

## List of Tables

Table 4.1	Simulated gain and the back lobe of the original and the modified single-conductor strip leaky-wave antenna .....	53
Table 4.2	Simulated front-to-back ratio of the original and the modified single-conductor strip leaky-wave antenna .....	54
Table 4.3	Measured and simulated results of the gain and the back lobe of the modified single-conductor strip leaky-wave antenna .....	60
Table 4.4	Measured and simulated front-to-back ratio of the modified single-conductor strip leaky-wave antenna.....	61



# Chapter 1

## Introduction

### 1.1 MOTIVATION

The printed-circuit type antenna is the best choice for the trend in antenna development, which is compact, relatively inexpensive, and highly reliable. In RF and narrow-band applications, resonant type antennas are most widely used since the matching network design is simple, and the antenna size is small when using a higher dielectric constant substrate. However, in millimeter wave and wide band applications, the resonant type antenna (usually a patch one) is no longer the best choice due to its inherent nature such as a narrow operational bandwidth, complexity in matching network design for array applications, and serious tolerance requirement in fabrication. So the printed circuit type leaky wave antenna is a better candidate in millimeter wave applications owing to its advantages such as simplicity in array design, broad band, beam-scanning capability, and relaxed requirement of tolerance.

In [1], experimental verification of a microstrip-line higher order mode leaky-wave antenna was conducted without explaining the physics underlying the design of the antenna. In [2], [3], Oliner explained the physics underlying the leaky-wave antenna design constructed in [1], and presented analysis data for the antenna design. In [4], [5], the familiar spectral-domain analysis was used, with the appropriate choice of branch cuts and integration contours. Thus, numerous issues about leaky-wave antennas are subsequently investigated, such as full-wave analysis of leaky modes, feeding structures, antenna arrays, etc.

In [6], A leaky-wave broad band antenna that has only a single-conductor strip on a substrate but no ground plane was presented. That absence of a ground plane allows both  $TE_0$  and  $TM_0$  surface-wave modes to exist in this single-conductor strip structure. The main



feature of the single-conductor strip leaky-wave antenna is that the main beam is fixed in the end-fire direction over a broad band region. This pattern feature is useful in some applications that require a main beam in the end-fire direction. From the radiation patterns of this leaky-wave antenna, we observe that the back lobe is quite large. In this thesis, a novel method is proposed to alleviate this undesired radiation.

## **1.2 ORGANIZATION OF THIS THESIS**

This thesis is divided into four parts. In chapter 2, we introduce the condition of leakage and mode distinction. In chapter 3, the full-wave method, spectral domain approach is used to analyze the propagation characteristics of the first higher-order leaky mode of the single-conductor strip structure. The numerical results are calculated to decide the operating frequency band of leaky-wave antenna. In chapter 4, in order to alleviate the large back lobe of the single-conductor leaky-wave antenna, the feeding structure is modified with two broadband planar baluns. Finally, some conclusions and future work are made in Chapter 5.

# Chapter 2

## Physical Properties of Leaky Waves

Most planar transmission lines used in microwave and millimeter-wave frequency region can exhibit several new propagation phenomena. They have relevance to leaky modes that leak power in the form of the surface wave and/or the space wave. Both the surface wave leakage and the space wave leakage on planar transmission structures can produce unwanted crosstalk between neighboring parts of a circuit and undesired package effects, or can be used to create new circuit components and antennas. In this chapter, we will explain when leakage can occur.

### 2.1 LEAKAGE CONDITION

In general, leaky modes can be divided in two types: surface-wave leaky modes and space-wave leaky modes [3]. The surface-wave leaky modes are those modes that leak power in the form of surface waves on the surrounding substrate as they propagate. The space-wave leaky modes leak power in the form of space waves radiating into space as well as surface waves.

#### 2.1.1 Surface-Wave Leaky Mode

Fig. 2.1 illustrates the structure of a coplanar waveguide (CPW). As shown in Fig. 2.2, the surface wave leakage condition can be examined from the top view of a metal strip lying on the air-substrate interface, where this strip can represent the center strip of CPW, or the strip of microstrip line, or whatever. From the figure the relation below is observed

$$k_x^2 = k_s^2 - \beta^2 \quad (2-1)$$

where  $\beta$  is the phase constant of the dominant mode guided along the  $z$ -direction,  $k_x$  is the

transverse wavenumber, and  $k_s$  is the propagation wavenumber of the surface wave supported on the substrate in the vicinity of the guiding strip. If  $\beta > k_s$ , Eq. (2.1) results in  $k_x^2 < 0$ , then  $k_x$  is seen to be imaginary, it means that the modal field decays transversely in

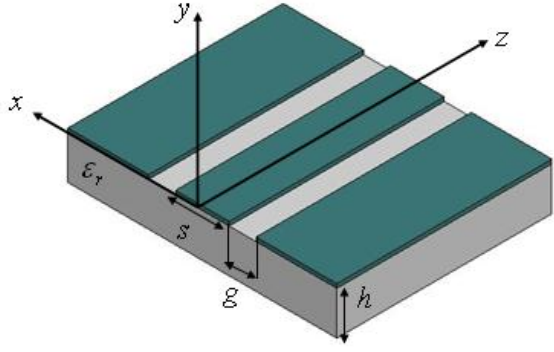


Fig. 2.1 Coplanar waveguide structure.

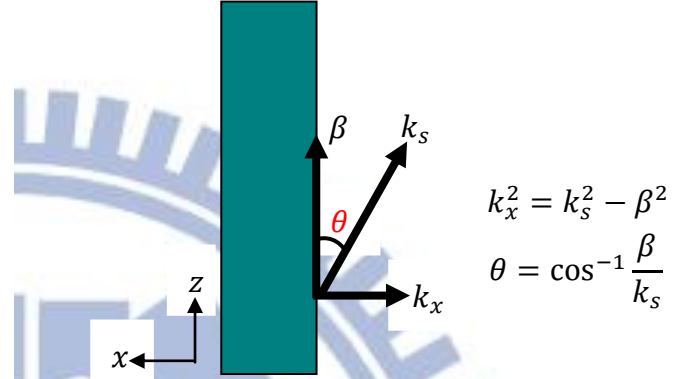


Fig. 2.2 Top view of a metal strip lying on the substrate, showing the angle  $\theta$  of leakage into the surface wave  $k_s$  on the surrounding substrate.

the  $x$ -direction and the mode guided in the  $z$ -direction is purely bound. On the other hand, if  $\beta < k_s$ , Eq. (2.1) results in  $k_x^2 > 0$ , then  $k_x$  is seen to be real, it means that power will leak from the guided mode at an angle  $\theta$  in the form of surface waves on the surrounding substrate, or a parallel-plate mode if there exists a top cover above the substrate. The angle  $\theta$  can be defined by

$$\cos\theta \cong \beta/k_s = (\beta/k_0)/(k_s/k_0) \quad (2-2)$$

where  $k_0$  is the free space wavenumber. For this reason, the surface wave leakage occurs when the condition  $\beta < k_s$  is satisfied, or, dividing both sides by  $k_0$ , that can be written as

$$\beta/k_0 < k_s/k_0 \quad (2-3)$$

Truly, when leakage occurs, the wavenumber of the guided mode becomes complex  $\beta - j\alpha$ , where  $\alpha$  is the attenuation constant. Eq. (2.2) is no longer exactly correct, but it is still a

good approximation.

We observe from the dispersion curves for a CPW in Fig. 2.3 that Eq. (2.3) is satisfied when frequency  $f$  is greater than the critical frequency  $f_c$  at which the two curves cross in Fig. 2.3 [7]. All of the uniplanar lines will leak power above some critical frequency. The power will radiate away in the lateral direction at an angle that varies with frequency, and the leakage rate is also frequency-sensitive. The manner in which the dominant mode becomes leaky, and the critical frequency at which this occurs, are quite different for each of the guiding structure. For example, the dominant mode of conductor-backed coplanar waveguide (CBCPW, see Fig. 2.4) is leaky at all frequency as shown in Fig. 2.5. Nevertheless, the fundamental physical idea for all various planar transmission line structures can be made easy with the illustration shown in Fig. 2.2.

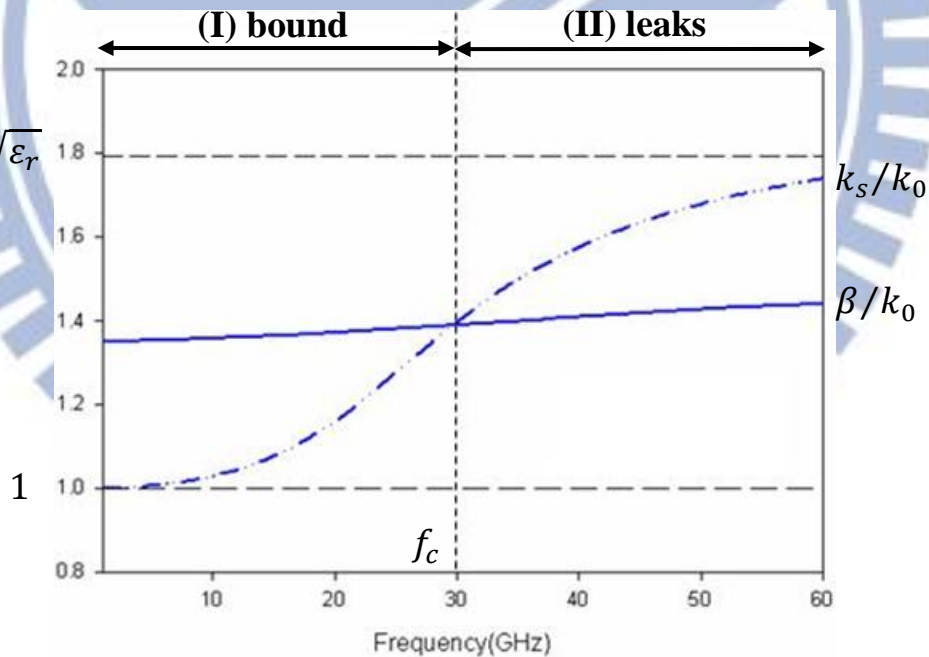


Fig. 2.3 A typical dispersion plot for a CPW. For  $f > f_c$  the mode becomes leaky, in accordance with Eq. (2.3).

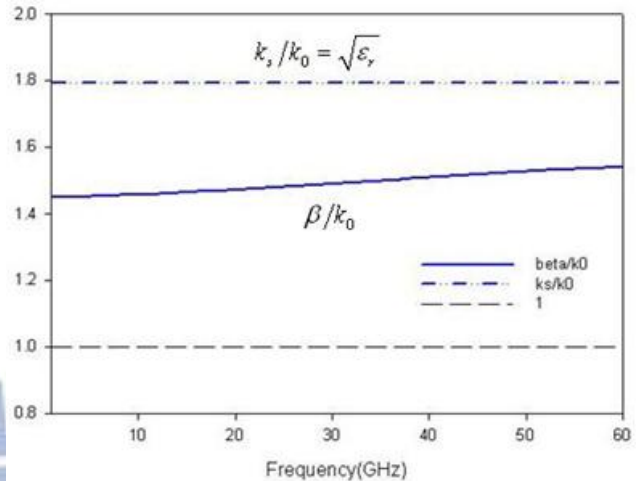
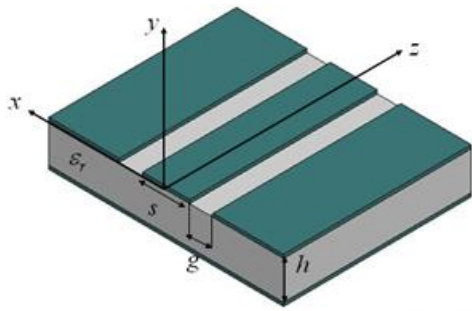


Fig. 2.4 Conductor-backed coplanar waveguide structure.

Fig. 2.5 Dispersion curves of the normalized phase constant of the surface-wave leaky mode for a CBCPW.

Fig. 2.6 depicts the structure of a conductor-backed slotline (CBSL), the effective dielectric constant,  $\epsilon_{eff}$ , of the slotline is between  $\epsilon_r$  and 1, where  $k_c = k_0\sqrt{\epsilon_r} > \beta = k_0\sqrt{\epsilon_{eff}} > k_0$  [8]. The characteristic parallel-plate propagation constant,  $k_c = k_0\sqrt{\epsilon_r}$ , is unconditionally greater than  $\beta$ , which results in an unconditional leakage effect, independent of frequency or parallel-plate thickness. We see the top view of a CBSL as shown in Fig. 2.7, the point a and b receive the characteristic waves originating respectively from the points a' and b' along the slot, where  $\theta = \cos^{-1}(\beta/k_s)$ . When the slotline is lossy because of the

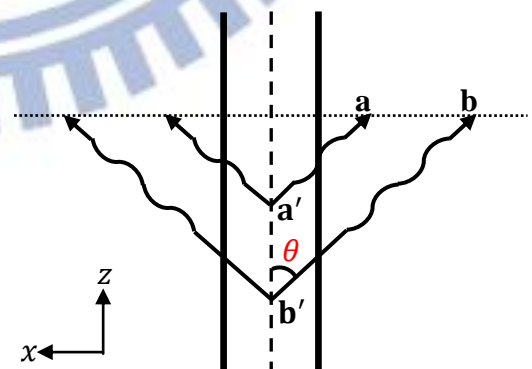
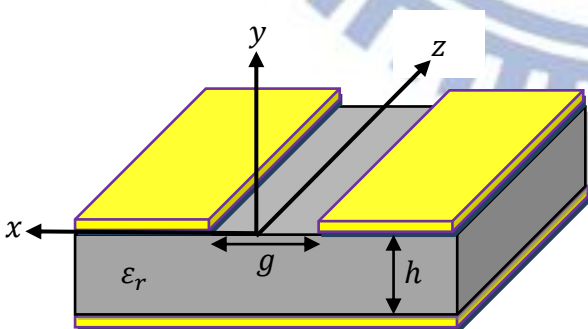


Fig. 2.6 Conductor-backed slotline structure.

Fig. 2.7 The amplitude decays in the z direction ( $b' > a'$ ) due to leakage loss, but in the x direction at a given z, the amplitude increases exponentially ( $b > a$ ).

leakage effect, the electric field on the slotline has an exponential decay along the propagation direction, resulting in a larger value at  $b'$  than at  $a'$ . Hence, the field magnitude at  $b$  tends to be larger than that at  $a$ , which explains an increasing trend of the electric field in the transverse direction.

### 2.1.2 Space-Wave Leaky Mode

Let us consider the microstrip line (see Fig. 2.8) as an example, of which the cross section is shown in Fig. 2.9. With similar discussion to explain the condition of surface wave leakage, the radiation condition into space wave is given, in good approximation, by  $\beta < k_0$ , or, dividing both sides by  $k_0$ , that can be expressed as

$$\beta/k_0 < 1 \quad (2-4)$$

On the other hand, the relation  $k_s > k_0$  is always held, so that the leakage condition into surface wave  $k_s > \beta$  is always satisfied, this new mode leaks power in the forms of both the surface wave propagating on substrate and space wave radiating into space. Therefore, this mode is physical in the fast-wave ( $\beta = \omega/v_p < k_0$ ) region, and we call it here the space-wave leaky mode that corresponds to radiation at an angle  $\theta = \cos^{-1}(\beta/k_0)$  (This again is not rigorously true for complex  $\beta - j\alpha$ , but provides a fairly good approximation), the value of this angle changing with the frequency.

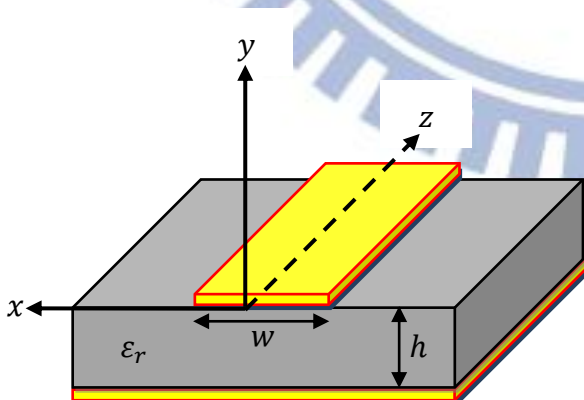


Fig. 2.8 Microstrip line structure.

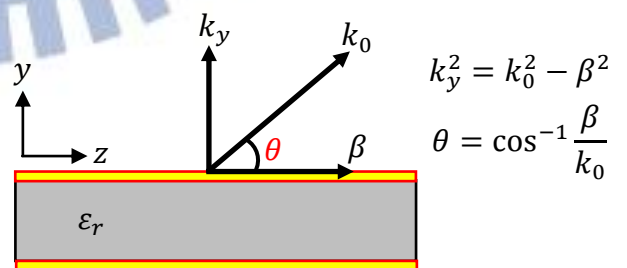


Fig. 2.9 Cross section of a microstrip line.

Also, with similar discussion to explain the exponential growth of the electric field in the transverse direction for the surface wave leakage case, one can explain in this case a nondecaying field in the normal direction ( $b > a$ ) (see Fig. 2.10) for the space wave leakage. Interestingly, any forward wave that decays in the longitudinal direction due to leakage loss must increase exponentially in the surrounding air region. The leaky wave is often described as being "improper" or "nonspectral", meaning exponentially increasing in the air region [9].

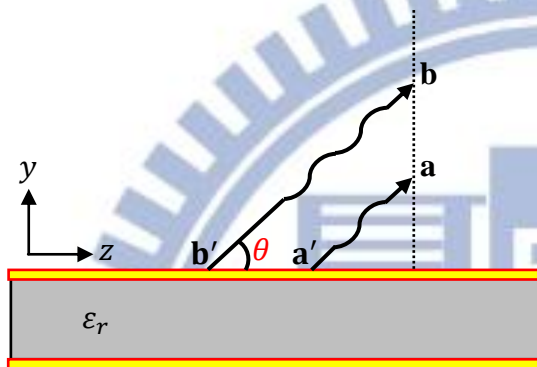


Fig. 2.10 Radiation leakage in a microstrip line at the air-substrate interface.

## 2.2 MODE DISTINCTION

After our previous discussions, we will follow the classification by Lin in [10], [11] to divide the frequency range into the following four regions:

1.  $\beta < k_0, \alpha > \beta$  (large  $\alpha$ ) -----reactive cutoff region.
2.  $\beta < k_0, \beta > \alpha$  (small  $\alpha$ ) -----surface wave and space wave leakage region.
3.  $k_s > \beta > k_0$ , (small  $\alpha$ ) -----surface wave leakage region.
4.  $\beta > k_s, \alpha = 0$  -----bound mode region.

In the radiation region ( $\beta < k_0$ ) with a larger attenuation constant is reactive and below cutoff, and has a different mode nature from that with a smaller attenuation constant. Therefore, this radiation-frequency region can further be divided into two regions with decreasing frequency: the antenna-mode region ( $\beta < k_0, \beta > \alpha$ ) where most of the guided power leaks away in the

forms of space wave and surface wave, and the reactive cutoff region, where most of the power is reflected back to the feed line, however, the propagation constant is still a complex number with a small real part,  $\beta$ , and a large imaginary part,  $j\alpha$ , indicating that the mode is not strictly cutoff, but a very small portion of energy still propagates down the transmission line. In design of leaky-wave antennas, this distinction of mode nature in the radiation region is essential since the antenna efficiency is low in the reactive-mode region. We can simply define the lower frequency edge ( $f_L$ ) and the upper frequency edge ( $f_H$ ) of the usable frequency range for the leaky wave antenna:

$$\beta(f_L) = \alpha(f_L) \quad (2-5)$$

$$\beta(f_H) = k_0 \quad (2-6)$$

Fig. 2.11 shows the normalized propagation constant for the first higher-order mode of microstrip line as an example. For this case ( $w = 15$  mm,  $h = 0.508$  mm,  $\epsilon_r = 3.55$ ), the usable frequency range for the leaky wave antenna is approximately 5.1 to 6.1 GHz.

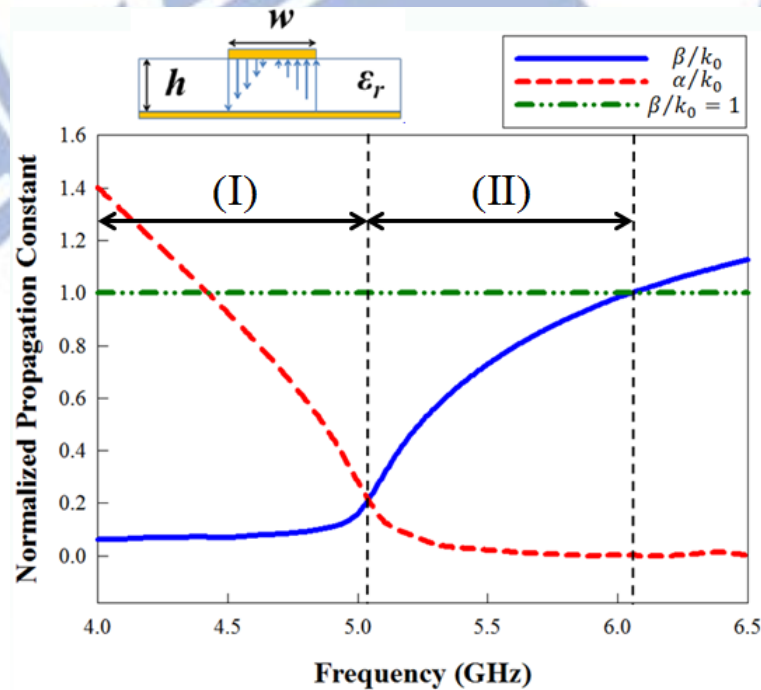


Fig. 2.11 Behavior of the normalized phase constant  $\beta/k_0$  and the attenuation constant  $\alpha/k_0$  as a function of frequency for the first higher-order mode of the microstrip line.



# Chapter 3

## Analysis and Numerical Results

Planar transmission line analysis in the Fourier transform domain (or spectral domain) is superior to many numerical methods in the spatial domain. The spectral domain approach (SDA) was presented by Itoh and Mittra [12], this method is basically a modification of Galerkin's approach adapted for application in the Fourier transform domain, or spectral domain (In SDA, Galerkin's method is used to yield a homogeneous system of equations to determine the propagation constant). The Fourier transform is taken along the direction parallel to the substrate and perpendicular to the strip. The main reason the SDA is numerically efficient is that it requires a significant analytical preprocessing. This feature in turn imposes a certain restriction on the applicability of the method. One of the limitations is that SDA requires infinitesimal thickness for the strip conductor. It is also difficult to treat the structure with a strip having finite conductivity. No discontinuity in the substrate in the sideward direction is allowed. In spite of these limitations, however, SDA is one of the most popular and widely used numerical techniques.

In this chapter, the general approach (field approach) is described [13].

### 3.1 SPACE DOMAIN TO SPECTRAL DOMAIN

Before the detailed formulation process is presented, let us compare the types of equations obtained by the SDA and those obtained by a typical space domain formulation [13]. Fig. 3.1 shows a shielded microstrip line with its cross-sectional view as an example. In conventional space domain analysis, the structure can be analyzed by first formulating the following coupled homogeneous integral equations.

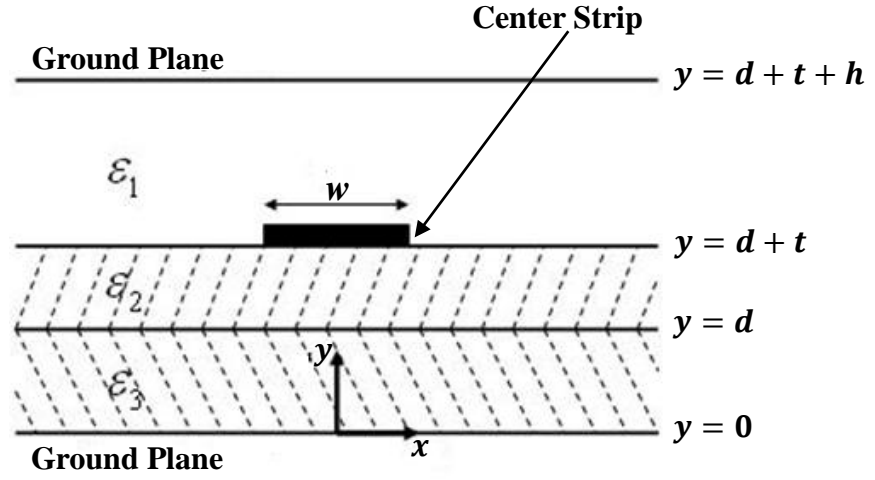


Fig. 3.1 Corss-sectional view of a shielded microstrip line.

The equations will then be solved for the unknown propagation constant  $\beta$ .

$$\int [Z_{zz}(x-x', y)J_z(x') + Z_{zx}(x-x', y)J_x(x')] dx' = E_z(x) \quad (3-1a)$$

$$\int [Z_{xz}(x-x', y)J_z(x') + Z_{xx}(x-x', y)J_x(x')] dx' = E_x(x) \quad (3-1b)$$

Where  $E_z$  and  $E_x$  are unknown electric fields on the boundary at  $y = d + t$ ,  $J_z$  and  $J_x$  are the longitudinal and transverse current components on the strip ( $y = d + t$ ), and the spatial Green's functions ( $Z_{zz}$ ,  $Z_{zx}$ ,  $Z_{xz}$ ,  $Z_{xx}$ ) are functions of  $\beta$ . The integration is over the strip where  $E_z(x)$  and  $E_x(x)$  are zero, as the strip is perfectly conducting. The left-hand sides of the equations are therefore required to be zero on the strip. These equations can be solved if  $Z_{zz}$ ,  $Z_{zx}$ ,  $Z_{xz}$  and  $Z_{xx}$  are given. As we will see shortly, the following algebraic equations, instead of the coupled integral equations, are obtained in the spectral domain formulation. These equations are Fourier transforms of the coupled integral equations.

$$\tilde{Z}_{zz}(k_x, d+t)\tilde{J}_z(k_x) + \tilde{Z}_{zx}(k_x, d+t)\tilde{J}_x(k_x) = \tilde{E}_z(k_x, d+t) \quad (3-2a)$$

$$\tilde{Z}_{xz}(k_x, d+t)\tilde{J}_z(k_x) + \tilde{Z}_{xx}(k_x, d+t)\tilde{J}_x(k_x) = \tilde{E}_x(k_x, d+t) \quad (3-2b)$$

Where quantities with tildes ( $\tilde{\phantom{x}}$ ) are Fourier transforms of corresponding quantities.

The Fourier and inverse Fourier transform are defined as

$$\tilde{\Phi}(k_x) = \int_{-\infty}^{\infty} \Phi(x) e^{jk_x x} dx \quad (3-3a)$$

$$\Phi(x) = \frac{1}{2\pi} \int_{-\infty}^{\infty} \tilde{\Phi}(k_x) e^{-jk_x x} dk_x \quad (3-3b)$$

The right-hand side of Eqs. (3-2) is no longer zero because the Fourier transform requires integration over all  $x$ , not only over the strip. The equations contain four unknowns  $J_z$ ,  $J_x$ ,  $E_z$ ,  $E_x$  with unknown  $\beta$ .  $E_z$  and  $E_x$ , however, will be eliminated in the solution process based on the Galerkin procedure.

## 3.2 SDA ON SINGLE-CONDUCTOR STRIP STRUCTURE

### 3.2.1 Field Approach

In this section, the Green's impedance functions  $Z_{zz}$ ,  $Z_{zx}$ ,  $Z_{xz}$ ,  $Z_{xx}$  will be derived for the single-conductor strip structure in Fig. 3.2. Only one perfect conducting and infinitely thin strip is located at the interface between a semi-infinite air layer and an isotropic lossless substrate, with a dielectric constant of  $\epsilon_r$  and a thickness of  $h$ . This structure is assumed to be uniform and infinite in both  $x$ - and  $z$ -directions. First, the hybrid fields are expressed in terms of Superposition of TE-to- $y$  and TM-to- $y$  expressions [14] with scalar potentials  $\tilde{\psi}^e$  and  $\tilde{\psi}^h$  as follows:

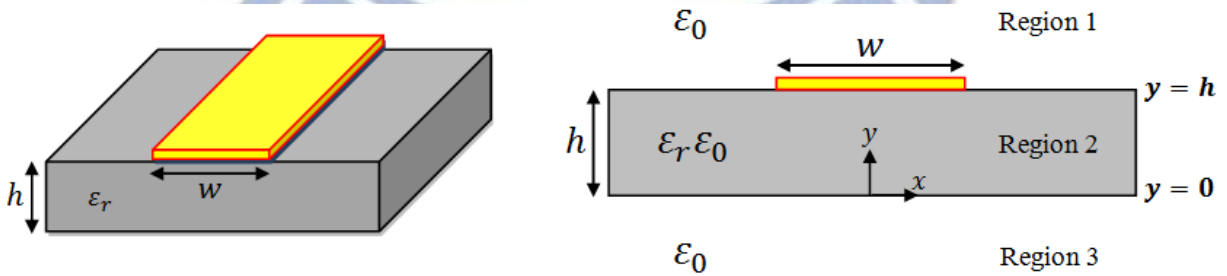


Fig. 3.2(a) Single-conductor strip structure. Fig. 3.2(b) Cross-sectional view of a single-conductor strip structure.

$$\begin{aligned}
\tilde{E}_x &= -j \frac{k_x}{\hat{y}} \frac{\partial \tilde{\psi}^e}{\partial y} - j k_z \tilde{\psi}^h & \tilde{H}_x &= j k_z \tilde{\psi}^e - j \frac{k_x}{\hat{z}} \frac{\partial \tilde{\psi}^h}{\partial y} \\
\tilde{E}_y &= \frac{1}{\hat{y}} \left( \frac{\partial^2}{\partial y^2} + k^2 \right) \tilde{\psi}^e & \tilde{H}_y &= \frac{1}{\hat{z}} \left( \frac{\partial^2}{\partial y^2} + k^2 \right) \tilde{\psi}^h \\
\tilde{E}_z &= -j \frac{k_z}{\hat{y}} \frac{\partial \tilde{\psi}^e}{\partial y} + j k_x \tilde{\psi}^h & \tilde{H}_z &= -j k_x \tilde{\psi}^e - j \frac{k_z}{\hat{z}} \frac{\partial \tilde{\psi}^h}{\partial y}
\end{aligned} \tag{3-4}$$

$$\hat{y} = j\omega\varepsilon \quad \hat{z} = j\omega\mu \quad k^2 = \omega^2\mu\varepsilon$$

Where  $\varepsilon$  is permittivity,  $\mu$  is permeability, the time convention  $e^{j\omega t}$  is implied, and the  $z$  dependence  $e^{-jk_z z}$  is assumed. Each field quantity in (3-4) is a Fourier transform of a corresponding quantity in the space domain (see Appendix A). The Fourier-transformed Helmholtz equation is expressed as (see Appendix A)

$$\left( -k_x^2 + \frac{\partial^2}{\partial y^2} - k_z^2 \right) \tilde{\psi} + k^2 \tilde{\psi} = 0 \tag{3-5}$$

The solution for this homogeneous differential equation is described in the form of

$$\tilde{\psi} = c_1 \cosh \gamma y + c_2 \sinh \gamma y, \quad \gamma^2 = k_x^2 + k_z^2 - k^2 \tag{3-6}$$

with appropriate coefficients  $c_1$  and  $c_2$ . When the boundary conditions at  $y = 0$ ,  $y = h$  and  $y \rightarrow \pm\infty$  are satisfied, the scalar potentials in each region are given as follows:

Region 1:

$$\tilde{\psi}_1^e = A^e e^{-\gamma_1(y-h)} \quad \tilde{\psi}_1^h = A^h e^{-\gamma_1(y-h)} \tag{3-7}$$

Region 2:

$$\tilde{\psi}_2^e = B^e \sin \gamma_2 y + C^e \cos \gamma_2 y \tag{3-8}$$

$$\tilde{\psi}_2^h = B^h \cos \gamma_2 y + C^h \sin \gamma_2 y$$

Region 3:

$$\tilde{\psi}_3^e = D^e e^{+\gamma_3 y} \quad \tilde{\psi}_3^h = D^h e^{+\gamma_3 y} \tag{3-9}$$

where each subscript refers to the corresponding region and  $A^e$ ,  $A^h$ , ...,  $D^h$  are unknown

coefficients.  $\gamma$  is the propagation constant in the  $y$ -direction and may be written as  $\gamma = jk_y$ .

Solution of (3-7)–(3-9) into (3-4) yields the field expressions in the three regions:

$$\begin{aligned}
\tilde{E}_{x1} &= jk_x \gamma_{y1} A^e e^{-\gamma_1(y-h)} - jk_z A^h e^{-\gamma_1(y-h)} \\
\tilde{E}_{x2} &= -jk_x \gamma_{y2} (B^e \cosh \gamma_2 y + C^e \sinh \gamma_2 y) - jk_z (B^h \cosh \gamma_2 y + C^h \sinh \gamma_2 y) \\
\tilde{E}_{x3} &= -jk_x \gamma_{y3} D^e e^{+\gamma_3 y} - jk_z D^h e^{+\gamma_3 y} \\
\tilde{E}_{y1} &= \frac{1}{\hat{y}_1} (\gamma_1^2 + k_1^2) A^e e^{-\gamma_1(y-h)} \\
\tilde{E}_{y2} &= \frac{1}{\hat{y}_2} (\gamma_2^2 + k_2^2) (B^e \sinh \gamma_2 y + C^e \cosh \gamma_2 y) \\
\tilde{E}_{y3} &= \frac{1}{\hat{y}_3} (\gamma_3^2 + k_3^2) D^e e^{+\gamma_3 y} \\
\tilde{E}_{z1} &= jk_z \gamma_{y1} A^e e^{-\gamma_1(y-h)} + jk_x A^h e^{-\gamma_1(y-h)} \\
\tilde{E}_{z2} &= -jk_z \gamma_{y2} (B^e \cosh \gamma_2 y + C^e \sinh \gamma_2 y) + jk_x (B^h \cosh \gamma_2 y + C^h \sinh \gamma_2 y) \\
\tilde{E}_{z3} &= -jk_z \gamma_{y3} D^e e^{+\gamma_3 y} + jk_x D^h e^{+\gamma_3 y} \\
\tilde{H}_{x1} &= jk_z A^e e^{-\gamma_1(y-h)} + jk_x \gamma_{z1} A^h e^{-\gamma_1(y-h)} \\
\tilde{H}_{x2} &= jk_z (B^e \sinh \gamma_2 y + C^e \cosh \gamma_2 y) - jk_x \gamma_{z2} (B^h \sinh \gamma_2 y + C^h \cosh \gamma_2 y) \\
\tilde{H}_{x3} &= jk_z D^e e^{+\gamma_3 y} - jk_x \gamma_{z3} D^h e^{+\gamma_3 y} \\
\tilde{H}_{y1} &= \frac{1}{\hat{z}_1} (\gamma_1^2 + k_1^2) A^h e^{-\gamma_1(y-h)} \\
\tilde{H}_{y2} &= \frac{1}{\hat{z}_2} (\gamma_2^2 + k_2^2) (B^h \cosh \gamma_2 y + C^h \sinh \gamma_2 y) \\
\tilde{H}_{y3} &= \frac{1}{\hat{z}_3} (\gamma_3^2 + k_3^2) D^h e^{+\gamma_3 y} \\
\tilde{H}_{z1} &= -jk_x A^e e^{-\gamma_1(y-h)} + jk_z \gamma_{z1} A^h e^{-\gamma_1(y-h)} \\
\tilde{H}_{z2} &= -jk_x (B^e \sinh \gamma_2 y + C^e \cosh \gamma_2 y) - jk_z \gamma_{z2} (B^h \sinh \gamma_2 y + C^h \cosh \gamma_2 y) \\
\tilde{H}_{z3} &= -jk_x D^e e^{+\gamma_3 y} - jk_z \gamma_{z3} D^h e^{+\gamma_3 y}
\end{aligned} \tag{3-10}$$

$$\gamma_i^2 = k_{xi}^2 + k_{zi}^2 - k_i^2 \quad \gamma_{yi} = \frac{\gamma_i}{\hat{y}_i} \quad \gamma_{zi} = \frac{\gamma_i}{\hat{z}_i} \quad i$$

where each subscript refers to the corresponding region. The unknown coefficients  $A^e$ ,  $A^h$ , ...,  $D^h$  are eliminated by imposing the boundary conditions at each interface. The boundary conditions in the spectral domain are obtained as the Fourier transforms of those in the space domain. In space domain, the boundary conditions are written as follows,

At  $y = h$ :

$$\begin{aligned}
 E_{x1} &= E_{x2} && \text{for all } x \\
 E_{z1} &= E_{z2} && \text{for all } x \\
 H_{x2} - H_{x1} &= \begin{cases} J_z(x) & |x| < w/2 \\ 0 & |x| > w/2 \end{cases} \\
 H_{z2} - H_{z1} &= \begin{cases} -J_x(x) & |x| < w/2 \\ 0 & |x| > w/2 \end{cases}
 \end{aligned}$$

At  $y = 0$ :

$$\begin{aligned}
 E_{x2} &= E_{x3} && \text{for all } x \\
 E_{z2} &= E_{z3} && \text{for all } x \\
 H_{x2} &= H_{x3} && \text{for all } x \\
 H_{z2} &= H_{z3} && \text{for all } x
 \end{aligned}$$

where  $J_x(x)$  and  $J_z(x)$  are the unknown surface current distributions on the strip at  $y = h$ . Notice these quantities need to be introduced so that the boundary conditions are specified for the entire range of  $x$ . Otherwise; it is not possible to take Fourier transforms. In the spectral domain, the boundary conditions are now given by the following equations.

At  $y = h$ :

$$\begin{aligned}
 \tilde{E}_{x1} &= \tilde{E}_{x2} \\
 \tilde{E}_{z1} &= \tilde{E}_{z2} \\
 \tilde{H}_{x2} - \tilde{H}_{x1} &= \tilde{J}_z(k_x) \\
 \tilde{H}_{z2} - \tilde{H}_{z1} &= -\tilde{J}_x(k_x)
 \end{aligned} \tag{3-11}$$

At  $y = 0$ :

$$\begin{aligned}
 \tilde{E}_{x2} &= \tilde{E}_{x3} \\
 \tilde{E}_{z2} &= \tilde{E}_{z3} \\
 \tilde{H}_{x3} - \tilde{H}_{x2} &= 0 \\
 \tilde{H}_{z3} - \tilde{H}_{z2} &= 0
 \end{aligned} \tag{3-12}$$

where  $\tilde{J}_z(k_x)$  and  $\tilde{J}_x(k_x)$  are Fourier transforms of unknown surface current components  $J_z(x)$  and  $J_x(x)$  on the strip at  $y = h$ .

Finally, the algebraic equations are derived in matrix from as follows:

$$[\tilde{E}] = [\tilde{G}_{EJ}] \cdot [\tilde{J}] \Rightarrow \begin{bmatrix} \tilde{E}_{z1} \\ \tilde{E}_{x1} \end{bmatrix} = \begin{bmatrix} \tilde{Z}_{zz} & \tilde{Z}_{zx} \\ \tilde{Z}_{xz} & \tilde{Z}_{xx} \end{bmatrix} \cdot \begin{bmatrix} \tilde{J}_z \\ \tilde{J}_x \end{bmatrix} \quad (3-13)$$

$$\tilde{Z}_{zz} = \frac{-1}{k_x^2 + k_z^2} (k_z^2 \tilde{Z}_e + k_x^2 \tilde{Z}_h) \quad (3-14)$$

$$\tilde{Z}_{zx} = \frac{-k_x k_z}{k_x^2 + k_z^2} (\tilde{Z}_e - \tilde{Z}_h) \quad (3-15)$$

$$\tilde{Z}_{xz} = \tilde{Z}_{zx} \quad (3-16)$$

$$\tilde{Z}_{xx} = \frac{-1}{k_x^2 + k_z^2} (k_x^2 \tilde{Z}_e + k_z^2 \tilde{Z}_h) \quad (3-17)$$

$$\tilde{Z}_e = \frac{\gamma_{y0} \coth \gamma h + \gamma_y}{2 \coth \gamma h + \gamma_{y0}/\gamma_y + \gamma_y/\gamma_{y0}} \quad (3-18)$$

$$\tilde{Z}_h = \frac{\frac{1}{\gamma_{z0}} \coth \gamma h + \frac{1}{\gamma_z}}{2 \coth \gamma h + \gamma_{z0}/\gamma_z + \gamma_z/\gamma_{z0}} \quad (3-19)$$

$$\gamma_0^2 = k_x^2 + k_z^2 - k^2, \quad k_0^2 = \omega^2 \mu_0 \epsilon_0$$

$$\gamma^2 = k_x^2 + k_z^2 - k^2, \quad k^2 = \omega^2 \mu_0 \epsilon_0 \epsilon_r$$

$$\gamma_{y0} = \frac{\gamma_0}{j\omega \epsilon_0}, \quad \gamma_y = \frac{\gamma}{j\omega \epsilon_0 \epsilon_r}, \quad \gamma_{z0} = \frac{\gamma_0}{j\omega \mu_0}, \quad \gamma_z = \frac{\gamma}{j\omega \mu_0}$$

The derivation of these formulations is detailed in [Appendix B](#). It should be noted that there is one more set of boundary conditions not used up to this stage. In the space domain, it is

$$E_z = E_x = 0 \quad \text{for } |x| < w/2 \text{ at } y = h \quad (3-20)$$

This set of conditions is incorporated in the solution process as we will see below.

### 3.2.2 Choice of Basis Functions

In order to solve (3-13), the unknown  $\tilde{J}_z$  and  $\tilde{J}_x$  should be expanded by known basis functions  $\tilde{J}_{zm}$  and  $\tilde{J}_{xm}$

$$\begin{aligned}\tilde{J}_z &= \sum_{m=1}^N c_m \tilde{J}_{zm}(k_x) \\ \tilde{J}_x &= \sum_{m=1}^M d_m \tilde{J}_{xm}(k_x)\end{aligned}\quad (3-21)$$

Where  $c_m$  and  $d_m$  are unknown coefficients. These approximations are assumed that  $\tilde{J}_z$  and  $\tilde{J}_x$  have known forms, and the only unknowns in their representation are the amplitude coefficients  $c_m$  and  $d_m$ . The basis functions must be chosen to correspond to the odd or even symmetry of the currents for the mode of interest. The current is nonzero only on the strip. Therefore, the basis functions  $\tilde{J}_{zm}(k_x)$  and  $\tilde{J}_{xm}(k_x)$  must also be chosen such that their inverse Fourier transforms are nonzero only on the strip  $|x| < w/2$ . The accuracy of the numerical results can be increased by selecting higher values of  $M$  and  $N$ , but it is relatively low efficiency because of taking more time during numerical computation. It means that the accuracy and efficiency depend on the numbers of basis functions. As shown in Fig. 3.3, due to the structural symmetry, a virtual perfect electric wall is placed at the center of the single

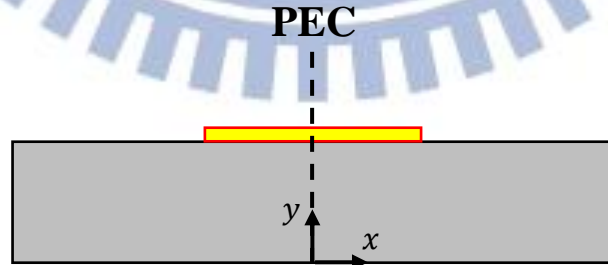


Fig. 3.3 Cross-sectional view of a single-conductor strip structure. A virtual perfect electric wall is placed at the center of this structure for the first higher-order mode.



conductor strip structure for the first higher-order mode, so odd basis functions for  $J_z$  and even basis functions for  $J_x$  are chosen [6]. Here, the following set of basis functions is employed [13]:

$$J_{zm}(x) = \frac{\sin[(2m-1)\pi x/w]}{\sqrt{1-(2x/w)^2}}, \quad m = 1, 2, \dots, N \quad (3-22)$$

$$J_{xm}(x) = \frac{\cos[(2m-1)\pi x/w]}{\sqrt{1-(2x/w)^2}}, \quad m = 1, 2, \dots, M \quad (3-23)$$

Note that the definitions given above are only over the strip  $|x| < w/2$  and the functions are zero elsewhere. The functions in (3-22) incorporate the correct edge singularity. The shapes of the first three functions are shown in Fig. 3.4. The Fourier transforms of (3-22) and (3-23) are (see Appendix C for derivations)

$$\tilde{J}_{zm}(k_x) = \frac{\pi w}{4j} \left[ J_0 \left( \left| \frac{wk_x + (2m-1)\pi}{2} \right| \right) - J_0 \left( \left| \frac{wk_x - (2m-1)\pi}{2} \right| \right) \right] \quad (3-24)$$

$$\tilde{J}_{xm}(k_x) = \frac{\pi w}{4} \left[ J_0 \left( \left| \frac{wk_x + (2m-1)\pi}{2} \right| \right) + J_0 \left( \left| \frac{wk_x - (2m-1)\pi}{2} \right| \right) \right] \quad (3-25)$$

where  $J_0$  denotes the zero-order Bessel function of the first kind.

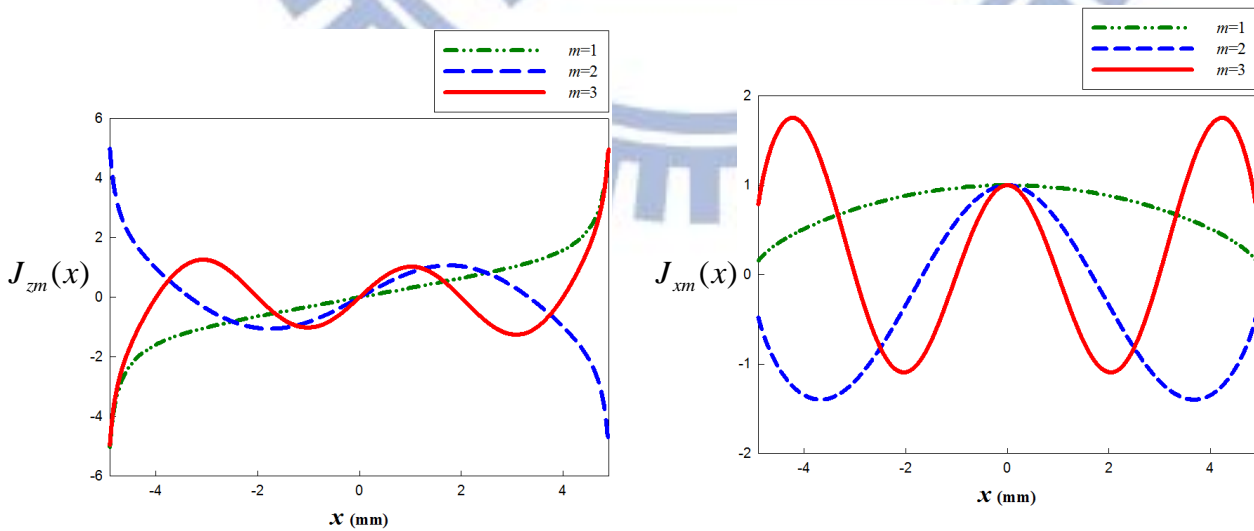


Fig. 3.4 Shapes of basis functions

### 3.2.3 Method of Solution

In this section, an efficient method for solving (3-13) is presented. It is noted that the two equations in (3-13) contain four unknowns  $\tilde{J}_z$ ,  $\tilde{J}_x$ ,  $\tilde{E}_z$  and  $\tilde{E}_x$ . The latter two unknowns  $\tilde{E}_z$  and  $\tilde{E}_x$ , however, can be eliminated by applying Galerkin's method in the spectral domain [12], [13]. The first step is to expand the unknown  $\tilde{J}_z$  and  $\tilde{J}_x$  in terms of known basis functions  $\tilde{J}_{zm}$  and  $\tilde{J}_{xm}$  as shown in (3-21). After substituting (3-21) into (3-13), one takes the inner products of the resultant equations with the known basis functions  $\tilde{J}_{zk}(k_x)$ ,  $\tilde{J}_{xl}(k_x)$ , respectively, for different values of  $k$  and  $l$ . This process yields the matrix equation

$$\int_{k_x} \left[ \tilde{J}_{zk} \tilde{Z}_{zz} \sum_{m=1}^N c_m \tilde{J}_{zm} + \tilde{J}_{zk} \tilde{Z}_{zx} \sum_{m=1}^M d_m \tilde{J}_{xm} \right] dk_x = 0, \quad k = 1, 2, 3 \dots N \quad (3-26a)$$

$$\int_{k_x} \left[ \tilde{J}_{xl} \tilde{Z}_{xz} \sum_{m=1}^N c_m \tilde{J}_{zm} + \tilde{J}_{xl} \tilde{Z}_{xx} \sum_{m=1}^M d_m \tilde{J}_{xm} \right] dk_x = 0, \quad l = 1, 2, 3 \dots M \quad (3-26b)$$

The right hand sides of (3-26) are zero by virtue of Parseval's theorem, because the currents  $J_{zk}(x)$ ,  $J_{xl}(x)$  and the field components  $E_z(x, h)$ ,  $E_x(x, h)$  are nonzero in the complementary regions of  $x$ . For instance, if the inner product of  $\tilde{E}_z$  on the left-hand side of (3-13) and  $\tilde{J}_{zk}(k_x)$  is taken, one obtains

$$\int_{-\infty}^{\infty} \tilde{J}_{zk}(k_x) \tilde{E}_{z1}(k_x) dk_x = 2\pi \int_{-\infty}^{\infty} J_{zk}(x) E_{z1}(-x) dx = 0$$

In the above,  $J_{zk}(x)$  is zero outside the strip and  $E_{z1}(x)$  is zero on the strip, thereby the integrand  $J_{zk}(x) E_{z1}(-x)$  vanishes for any value of  $x$ . Therefore, the final boundary condition (3-20) is now used.

Equations (3-26) will be expressed in matrix form as follows

$$\sum_{m=1}^N K_{km}^{(1,1)} c_m + \sum_{m=1}^M K_{km}^{(1,2)} d_m = 0, \quad k = 1, 2, \dots, N \quad (3-27a)$$

$$\sum_{m=1}^N K_{lm}^{(2,1)} c_m + \sum_{m=1}^M K_{lm}^{(2,2)} d_m = 0, \quad l = 1, 2, \dots, M \quad (3-27b)$$

where

$$K_{km}^{(1,1)} = \int_{-\infty}^{\infty} \tilde{J}_{zk}(k_x) \tilde{Z}_{zz}(k_x, k_z) \tilde{J}_{zm}(k_x) dk_x \quad (3-28)$$

$$K_{km}^{(1,2)} = \int_{-\infty}^{\infty} \tilde{J}_{zk}(k_x) \tilde{Z}_{zx}(k_x, k_z) \tilde{J}_{xm}(k_x) dk_x \quad (3-29)$$

$$K_{lm}^{(2,1)} = \int_{-\infty}^{\infty} \tilde{J}_{xl}(k_x) \tilde{Z}_{xz}(k_x, k_z) \tilde{J}_{zm}(k_x) dk_x \quad (3-30)$$

$$K_{lm}^{(2,2)} = \int_{-\infty}^{\infty} \tilde{J}_{xl}(k_x) \tilde{Z}_{xx}(k_x, k_z) \tilde{J}_{xm}(k_x) dk_x \quad (3-31)$$

For example, if one basis function for  $\tilde{J}_z$  and two basis functions for  $\tilde{J}_x$  are assumed, the matrix form of (3-27) with  $N=1$  and  $M=2$  becomes

$$\begin{bmatrix} \int_{k_x} \tilde{J}_{z1} \tilde{Z}_{zz} \tilde{J}_{z1} & \int_{k_x} \tilde{J}_{z1} \tilde{Z}_{zx} \tilde{J}_{x1} & \int_{k_x} \tilde{J}_{z1} \tilde{Z}_{zx} \tilde{J}_{x2} \\ \int_{k_x} \tilde{J}_{x1} \tilde{Z}_{xz} \tilde{J}_{z1} & \int_{k_x} \tilde{J}_{x1} \tilde{Z}_{xx} \tilde{J}_{x1} & \int_{k_x} \tilde{J}_{x1} \tilde{Z}_{xx} \tilde{J}_{x2} \\ \int_{k_x} \tilde{J}_{x2} \tilde{Z}_{xz} \tilde{J}_{z1} & \int_{k_x} \tilde{J}_{x2} \tilde{Z}_{xx} \tilde{J}_{x1} & \int_{k_x} \tilde{J}_{x2} \tilde{Z}_{xx} \tilde{J}_{x2} \end{bmatrix} \cdot \begin{bmatrix} c_1 \\ d_1 \\ d_2 \end{bmatrix} = 0 \quad (3-32)$$

In order that  $c_m$  and  $d_m$  have nontrivial solutions, the determinant of the matrix must be zero, and it is calculated with an assumed value of  $k_z$ . Then, by applying a root-seeking process, the true value of  $k_z$  is obtained at each frequency.

### 3.2.4 Discussion of Integration Contours

The main feature of interest in the spectral-domain analysis is the appropriate path of integration used to compute the matrix elements listed in (3-28)-(3-31) from which the propagation constant  $k_z$  of a specific wave mode is to be found. Since the path is an open contour in the  $k_x$  plane, from  $-\infty$  to  $+\infty$ , different solutions for  $k_z$  are possible depending upon the choice of the integration contour. The conventional path, which lies along the real axis in the complex  $k_x$ -plane (contour  $C_0$  of Fig. 3.5), yields the solution for the proper (bound) mode. The other two paths  $C_1$  and  $C_2$  in Fig. 3.5 are used to obtain leaky-mode solutions [15]. The absence of a ground plane allows the  $TM_0$  and the  $TE_0$  surface-wave modes to exist in the single-conductor strip structure [6]. Because both of the  $TM_0$  and the  $TE_0$  surface-wave modes exist for a dielectric slab structure (see Appendix D), so two proper surface-wave poles of  $k_{xp, TM_0}$  and  $k_{xp, TE_0}$  are present in the  $k_x$  plane. As seen in Fig. 3.5, the path  $C_1$  detours around the poles of the integrand in the  $k_x$  plane that correspond to the  $TM_0$  and the  $TE_0$  surface-wave modes of the dielectric slab structure, and lies entirely on the top Riemann sheet of the  $k_x$  plane, which is the proper sheet for the vertical wavenumber  $k_y$  [16]. This path is used to obtain the solution for a leaky mode that has leakage into only the  $TM_0$  and the  $TE_0$  surface waves [8]. In order to yield the solution for a leaky mode that energy leaks into both the space wave and the surface wave, the path  $C_2$  is utilized. This path lies partly on the improper sheet of the  $k_x$  plane in the region between the branch cuts and includes both proper surface-wave poles for the  $TM_0$  and the  $TE_0$  modes [6].

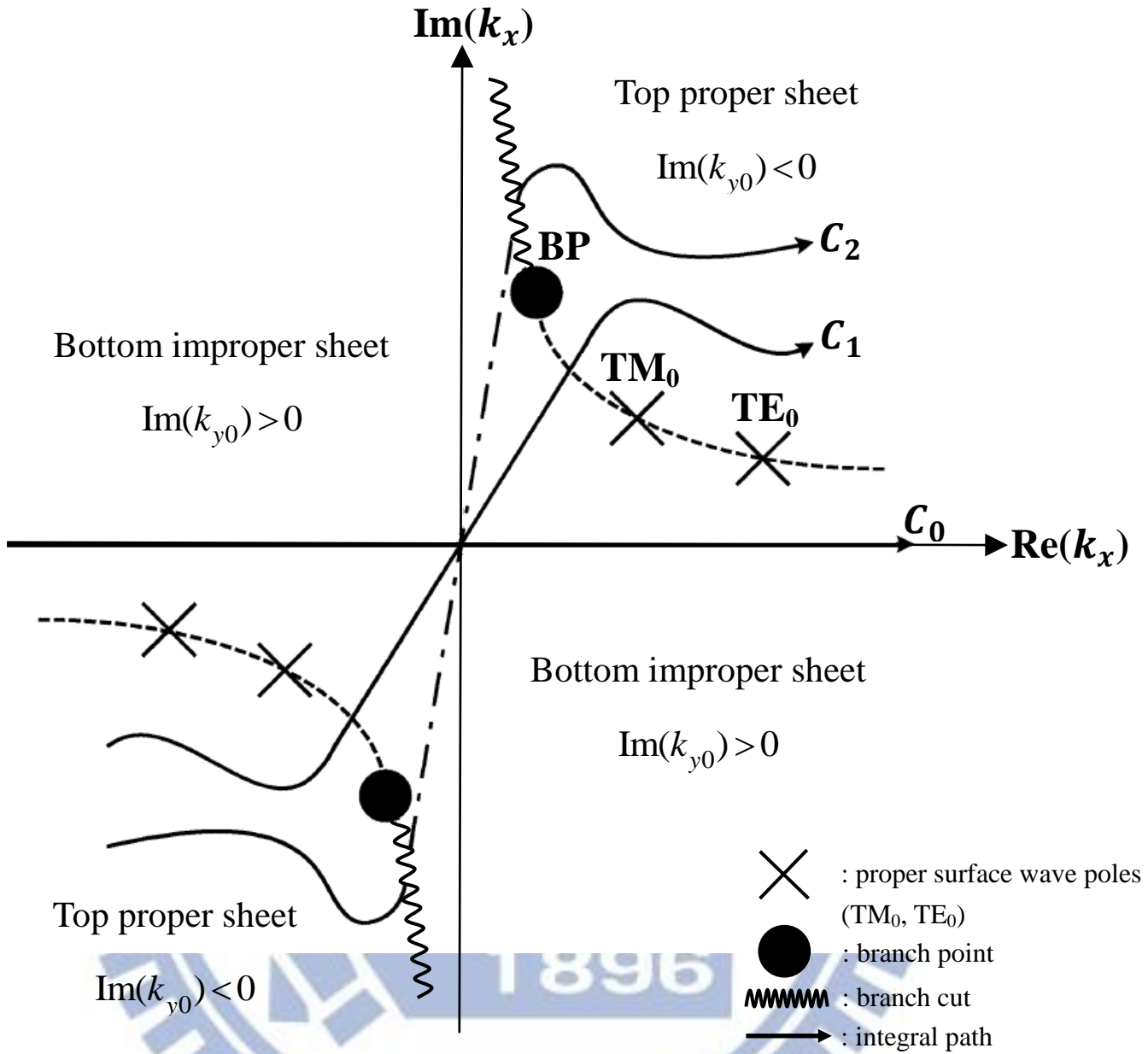


Fig. 3.5 Integral paths of the inverse Fourier transform on the  $k_x$  plane.

For the first higher-order leaky mode of a single conductor strip structure:

$$1) \text{ propagation constant } k_z = \beta - j\alpha \quad (3-33)$$

$$2) k_{y0} = \pm \sqrt{k_0^2 - k_x^2 - k_z^2}, \text{ (proper sheet "-", improper sheet "+")} \quad (3-34)$$

$$3) \text{ branch points } (k_{y0} = 0): k_{xb} = \pm \sqrt{k_0^2 - k_z^2} \quad (3-35)$$

These branch points define a two-sheeted Riemann surface in the  $k_x$  plane. Using the Sommerfeld choice for defining the corresponding branch cuts,

$\text{Im}(k_{y0}) = \text{Im}\sqrt{k_0^2 - k_x^2 - k_z^2} = 0$ , the two sheets correspond to the vertical wavenumber  $k_{y0}$  being proper (imaginary part negative) and improper (imaginary part positive). The derivation is detailed in [Appendix E](#).

$$4) \text{ TM}_0 \text{ poles: } k_{xp, \text{TM}_0} = \pm\sqrt{k_{s, \text{TM}_0}^2 - k_z^2} \quad (3-36)$$

where  $k_{s, \text{TM}_0}$  is the wavenumber associated with the  $\text{TM}_0$  surface wave mode of the dielectric slab structure.

$$5) \text{ TE}_0 \text{ poles: } k_{xp, \text{TE}_0} = \pm\sqrt{k_{s, \text{TE}_0}^2 - k_z^2} \quad (3-37)$$

where  $k_{s, \text{TE}_0}$  is the wavenumber associated with the  $\text{TE}_0$  surface wave mode of the dielectric slab structure.

For the integration of the products in Eqs. (3-28)-(3-31), the Green's functions meet poles along the  $k_x$  integral path. These poles are encountered when the denominator of  $\tilde{Z}_e$  or  $\tilde{Z}_h$  is equal to zero. The zeros of the denominators of  $\tilde{Z}_e$  and  $\tilde{Z}_h$  correspond to the odd TM and odd TE surface wave modes in the dielectric slab waveguide, respectively. That is, the zeros of the denominators of  $\tilde{Z}_e$  and  $\tilde{Z}_h$  give the phase constant of the surface waves ( $k_{s, \text{TM}_0}$  and  $k_{s, \text{TE}_0}$ ) existing in the dielectric slab waveguide. Substituting  $k_{s, \text{TM}_0}$  into Eq. (3-36) and  $k_{s, \text{TE}_0}$  into Eq. (3-37), we obtain the locations of the  $\text{TM}_0$  and  $\text{TE}_0$  surface wave poles ( $k_{xp, \text{TM}_0}$  and  $k_{xp, \text{TE}_0}$ ) in the complex  $k_x$  plane. By further deforming the path  $C_2$  in Fig. 3.6, we obtain a simple contour  $C'_2$  that encloses  $\pm k_{xp, \text{TM}_0}$  and  $\pm k_{xp, \text{TE}_0}$  in the residue sense. This means that the integrands of Eqs. (3-28)-(3-31) involve four residual contributions which correspond physically to excitation of the  $\text{TM}_0$  and  $\text{TE}_0$  surface waves; therefore we

can rearrange each of them as the quotient form as follows:

$$\tilde{J}(k_x)\tilde{Z}(k_x)\tilde{J}(k_x) = \frac{p(k_x)}{q(k_x)} \quad (3-38)$$

where  $p$  and  $q$  are both analytic at surface wave poles  $k_{xp}$ , and  $p(k_{xp}) \neq 0$ ,  $q(k_{xp}) = 0$ ,  $q'(k_{xp}) \neq 0$ . It can be shown that the residue is

$$\text{Res}_{k_x=k_{xp}} \frac{p(k_x)}{q(k_x)} = \frac{p(k_{xp})}{q'(k_{xp})} \quad (3-39)$$

Thus, the spectral integrals need to be evaluated along  $C'_2$  and can be simplified to

$$\begin{aligned} & \int_{-\infty}^{\text{Re}(-k_{xb})} (\bullet) dk_x + \int_{\text{Re}(-k_{xb})}^{-k_{xb}} (\bullet) dk_x + \underbrace{\int_{-k_{xb}}^{\text{Re}(-k_{xb})} (\bullet) dk_x + \int_{\text{Re}(-k_{xb})}^{\text{Re}(k_{xb})} (\bullet) dk_x + \int_{\text{Re}(k_{xb})}^{k_{xb}} (\bullet) dk_x}_{\text{improper sheet}} \\ & + \int_{k_{xb}}^{\text{Re}(k_{xb})} (\bullet) dk_x + \int_{\text{Re}(k_{xb})}^{\infty} (\bullet) dk_x + j2\pi \left[ \text{Res}(\bullet)_{-k_{xp, \text{TM}_0}} - \text{Res}(\bullet)_{k_{xp, \text{TM}_0}} + \text{Res}(\bullet)_{-k_{xp, \text{TE}_0}} - \text{Res}(\bullet)_{k_{xp, \text{TE}_0}} \right] \end{aligned} \quad (3-40)$$

where  $(\bullet)$  is the integrand of Eqs. (3-28)-(3-31).

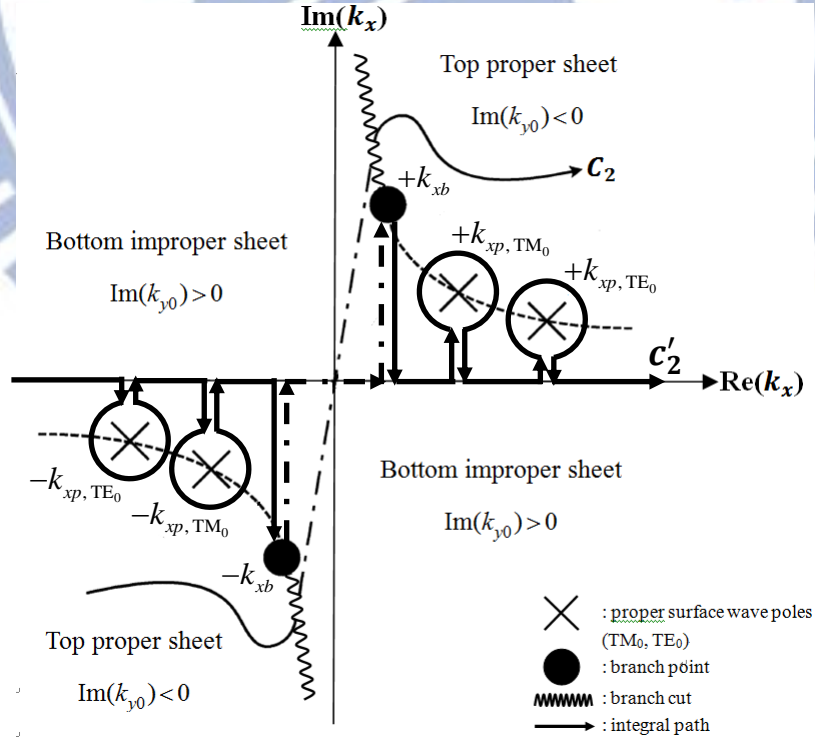


Fig. 3.6 Integral paths of the inverse Fourier transform on the  $k_x$  plane.

### 3.2.5 Numerical Results

Fig. 3.7 plots the normalized phase constant  $\beta/k_0$  and the normalized attenuation constant  $\alpha/k_0$  against the frequency of the first higher order mode of the single conductor strip structure with  $\epsilon_r = 3.55$  and  $h = 0.508$  mm for different strip widths. Because of the resonance of the transverse currents, the leaky region obviously shifts to a higher frequency for a narrow strip. Also, a narrow strip increases the attention constant.

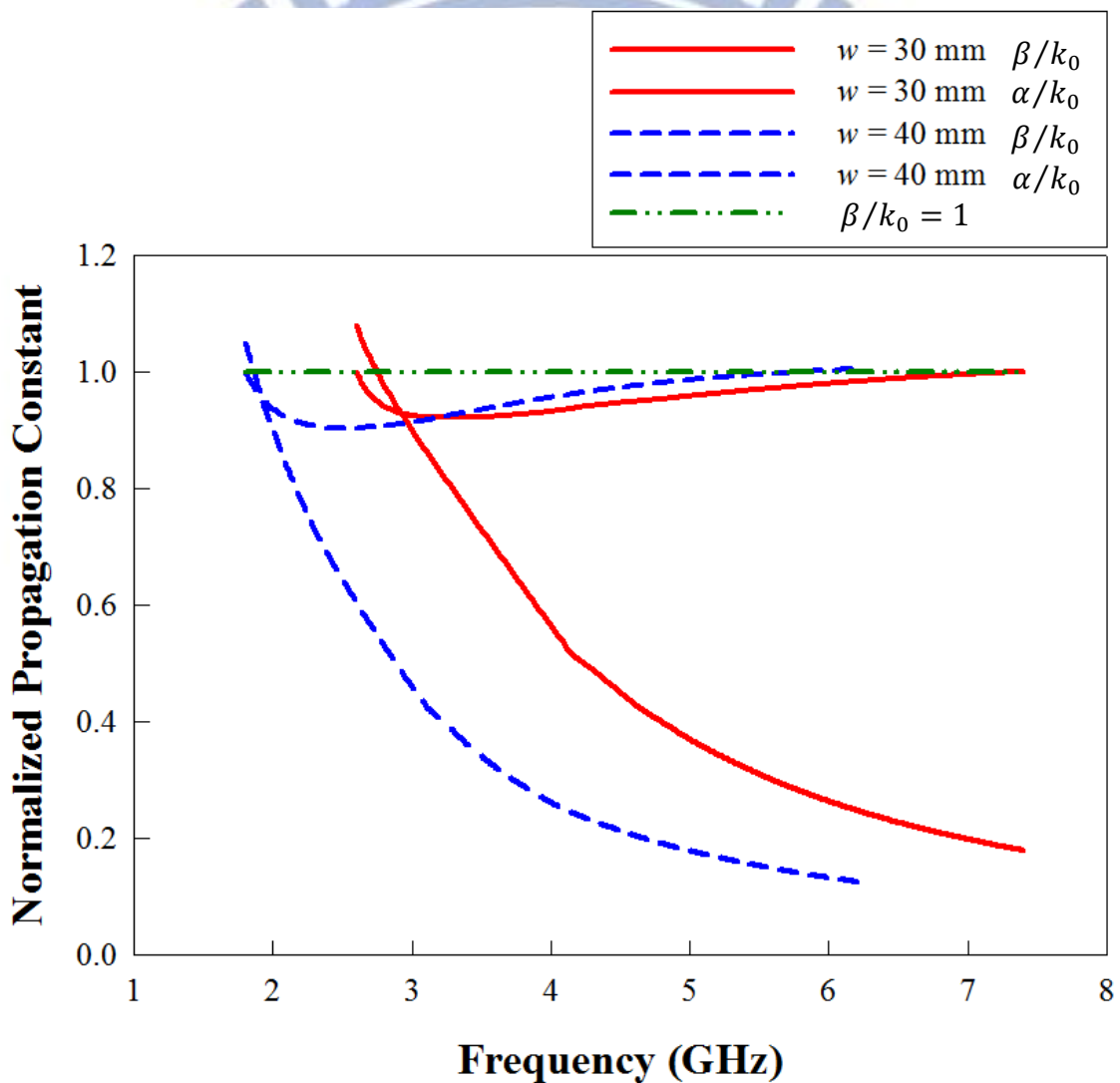


Fig. 3.7 Behavior of the normalized phase constants and the normalized attenuation constants as a function of frequencies for the first higher order mode of the single conductor strip structure with  $\epsilon_r = 3.55$  and  $h = 0.508$  mm for different strip widths.



Fig. 3.8 plots the normalized phase constant  $\beta/k_0$  and the normalized attenuation constant  $\alpha/k_0$  against the frequency of the first higher order mode of the single conductor strip structure with  $w = 40$  mm and  $h = 0.508$  mm for different dielectric constants. A substrate with a high dielectric constant will rapidly increase the normalized phase constant. Increasing the dielectric constant of the substrate also increase the attenuation constant.

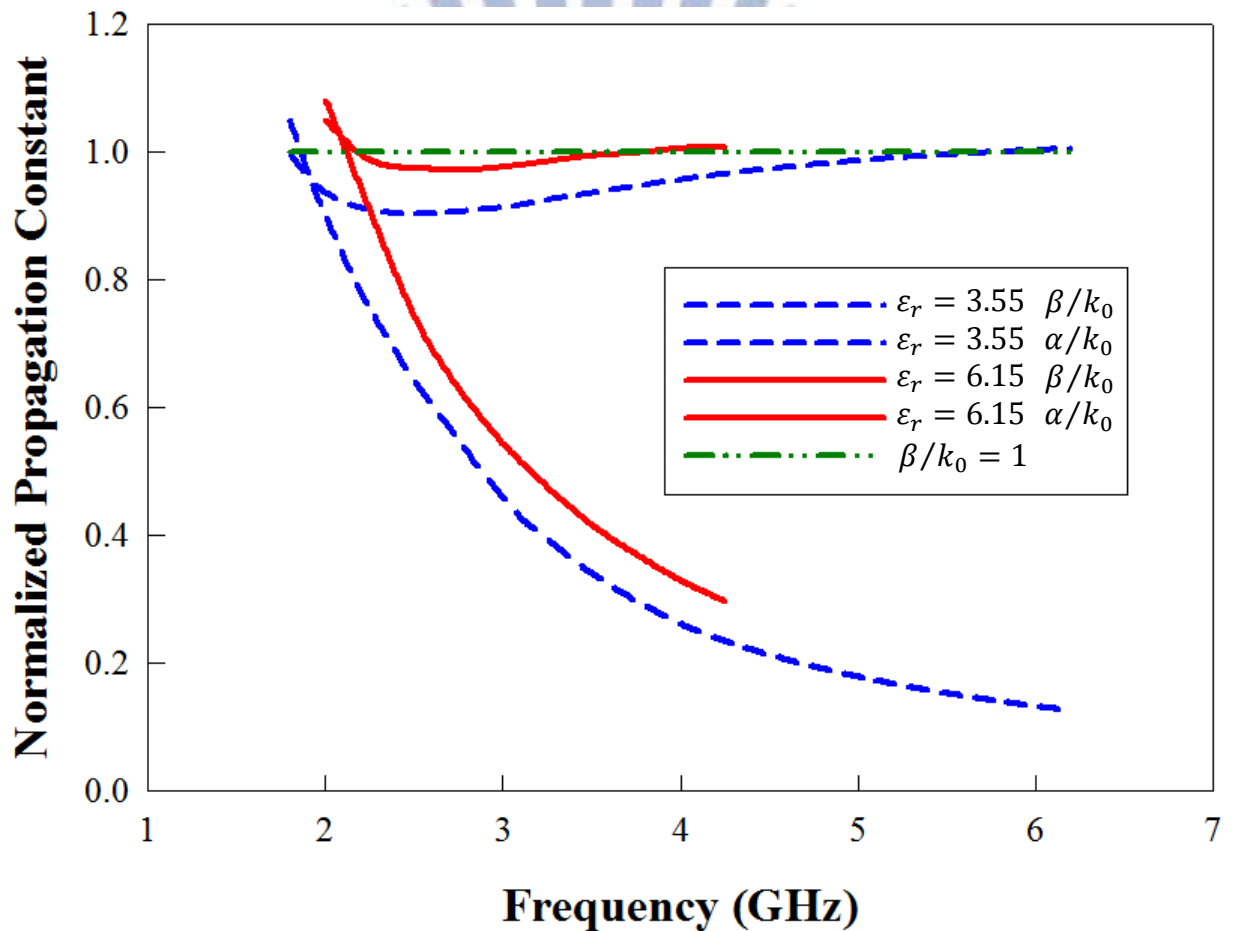


Fig. 3.8 Behavior of the normalized phase constants and the normalized attenuation constants as a function of frequencies for the first higher order mode of the single conductor strip structure with  $w = 40$  mm and  $h = 0.508$  mm for different dielectric constants.

Fig. 3.9 plots the normalized phase constant  $\beta/k_0$  and the normalized attenuation constant  $\alpha/k_0$  against the frequency of the first higher order mode of the single conductor strip structure with  $w = 40$  mm and  $\epsilon_r = 3.55$  for different substrate thicknesses. When the thickness of the substrate increases, the normalized phase constant increases, since the effective strip width is reduced by the fringing effect. The attenuation constant of a thin substrate is less than that of a thick substrate. Most of the energy is focused under the strip when the dielectric constant is high or the substrate is thick. The energy leaks out to the air more easily if the thickness or the dielectric constant of the substrate is lower or smaller.

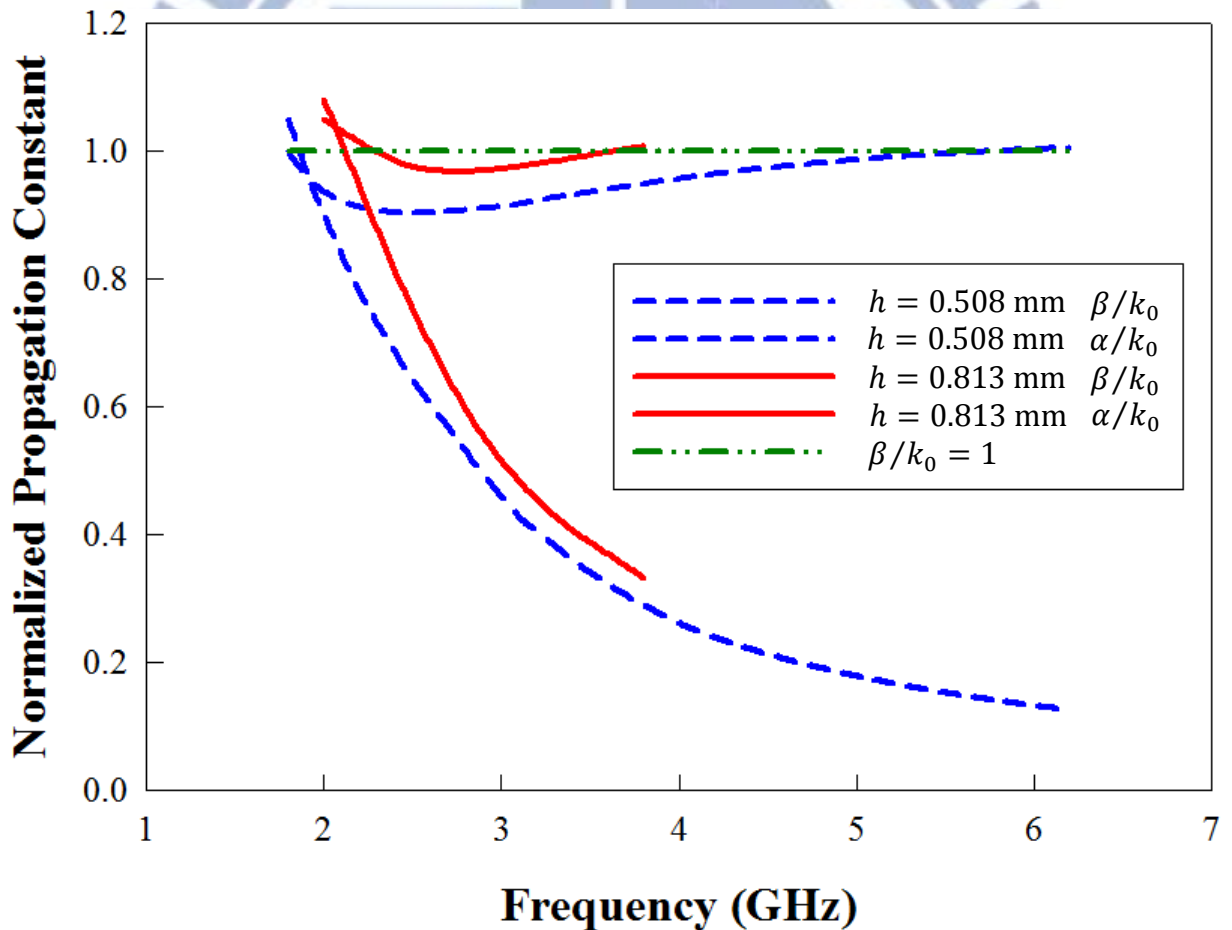


Fig. 3.9 Behavior of the normalized phase constants and the normalized attenuation constants as a function of frequencies for the first higher order mode of the single conductor strip structure with  $w = 40$  mm and  $\epsilon_r = 3.55$  for different substrate thicknesses.

# Chapter 4

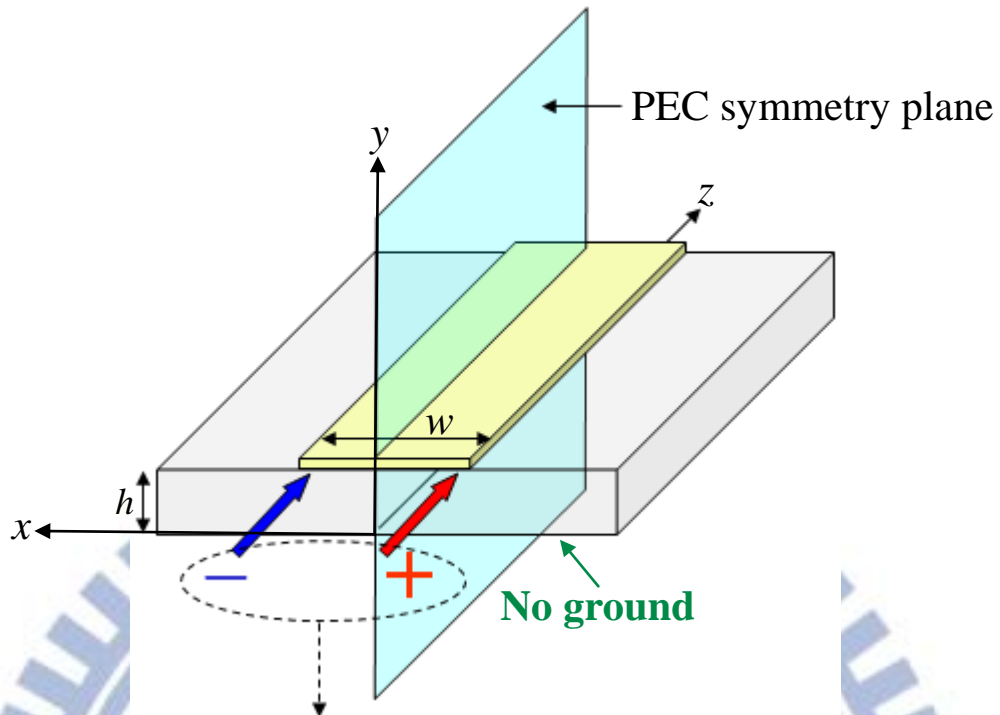
## Antenna Design, Simulation and Measurement

Broadband, high gain, and frequency-scanning are the main features of leaky wave antennas [9]. In some applications, such as point-to-point communication, the frequency-scanning characteristic is undesired. In this chapter, we use a single-conductor strip leaky wave antenna, which is proposed in [6]. Unlike other leaky-wave antennas, whose main beam changes according to frequency, the single-conductor strip leaky-wave antenna has a fixed main beam in the end-fire direction over a broadband region. Compared to the resonant antennas such as microstrip patch antenna and dipole antenna, whose radiation patterns are in the broadside direction, the pattern feature of single-conductor strip leaky-wave antenna is useful in some applications that require a main beam in the end-fire direction. Finally, to alleviate the problem of a large back lobe [17], the feeding structure of the single-conductor strip leaky-wave antenna is modified with two broadband planar baluns [18]. The simulated and measured results are also presented in this chapter.

### 4.1 DESIGN OF SINGLE-CONDUCTOR STRIP LEAKY-WAVE ANTENNA

#### 4.1.1 Broadband Planar Feeding Structure

As described above, the single-conductor strip structure has only a single-conductor strip on a substrate without a practical ground plane. For the first higher-order leaky mode in this structure, an infinite virtual PEC boundary is assumed at the center of the strip, in which the longitudinal currents are odd-symmetric and the transverse currents are even-symmetric with respect to the center [6]. As shown in Fig. 4.1, these current distributions help us design an appropriate feeding structure which generates two out-of-phase currents to feed this



To excite the first higher-order leaky mode

Fig. 4.1 An appropriate feeding structure which generates two out-of-phase currents is used to feed the single-conductor strip structure and thus excites the first higher order leaky mode.

single-conductor strip structure and thus excites the first higher order leaky mode. As shown in Fig. 4.2, a broadband planar feeding structure which consists of a conventional microstrip line · a microstrip-to-balanced-microstrip-line transition · a balanced-microstrip-line T-junction power divider and one set of the balanced microstrip lines is changed to form the inverted balanced microstrip lines is developed for the first higher-order leaky mode of the single-conductor strip line [6]. As shown in Fig. 4.3, gradually tapering the ground plane to a width equal to the strip width  $w$  makes conventional microstrip line a balanced microstrip line, with a strip of positive voltage on the upper side of the substrate and a strip of negative voltage on the lower side of the substrate.

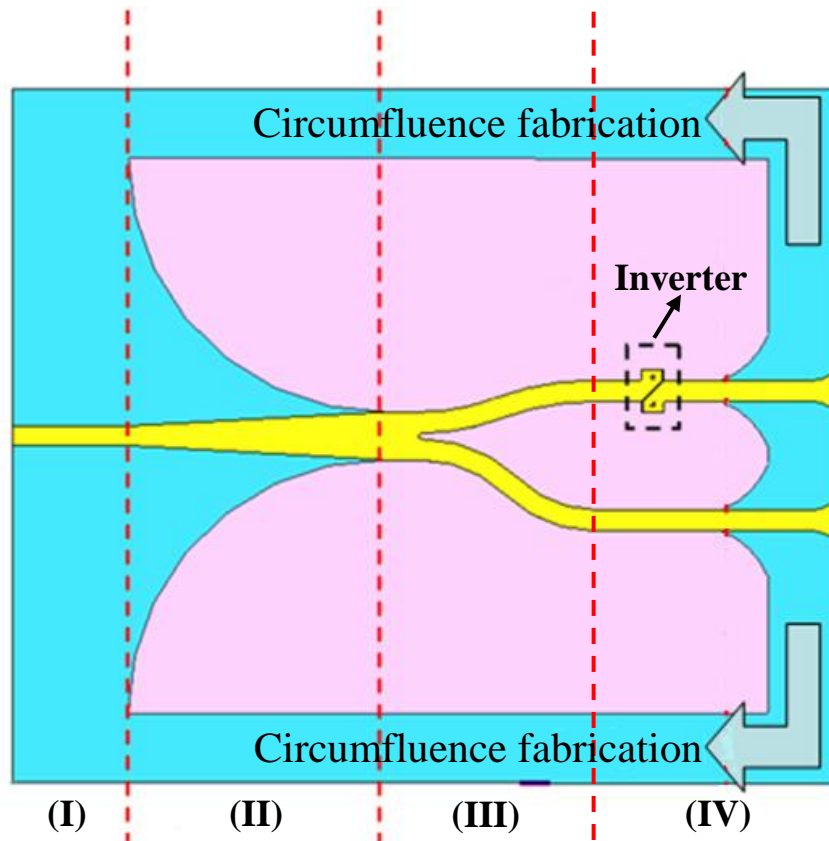


Fig. 4.2(a) Diagram of the broadband balun structure used to excite the first higher order leaky mode of the single-conductor strip line. The strips of the balun on the lower side of the substrate are connected to each other and returned back to the original ground plane of the microstrip line. This feeding structure consists of (I) a conventional microstrip line; (II) a microstrip-to-balanced-microstrip-line transition; (III) a balanced-microstrip-line T-junction power divider and (IV) one set of the balanced microstrip lines is changed to form the inverted balanced microstrip lines.

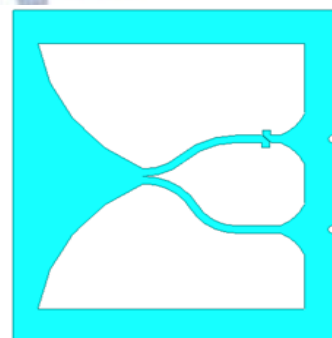
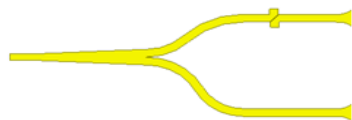


Fig. 4.2(b) The strip of the balun on the upper side of the substrate. Fig. 4.2(c) The strip of the balun on the lower side of the substrate.

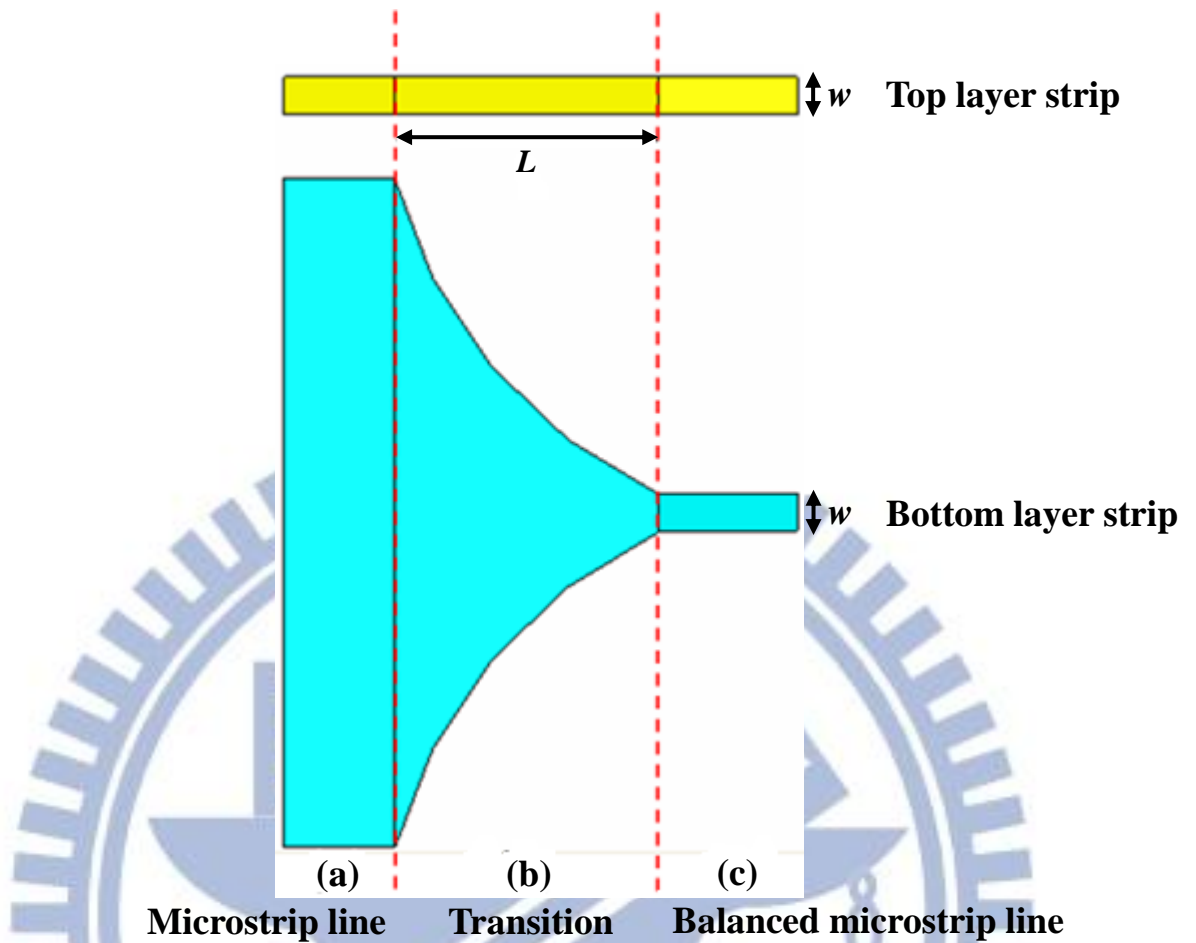


Fig. 4.3(a) Gradually tapering the ground plane to a width equal to the strip width  $w$  makes conventional microstrip line a balanced microstrip line.

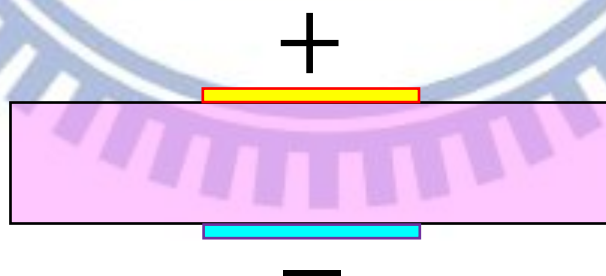


Fig. 4.3(b) Cross-sectional view of a balanced microstrip line, with a strip of positive voltage on the upper side of the substrate and a strip of negative voltage on the lower side of the substrate.

The position of the positive strip on the upper side of the substrate of the inverted balanced microstrip line structure is exchanged with that of the negative strip on the lower side of the substrate after a microstrip phase inverter illustrated in Fig. 4.4(a). As shown in Fig. 4.4(b), each of these positive and negative strips (strip1 and strip2) is terminated with a chamfered right-angled bend in an opposite direction, and each of the subsequent strips (strip3 and strip4) is also headed with a chamfered right-angle bend but in the other direction. A slanted gap separates two strips on the same side of the substrate. The bent stubs  $l_{up}$ , and  $l_{dn}$  on the upper and lower sides of the substrate, respectively, can be used to compensate for the reactance induced by the via holes and the slanted gaps, and may have different lengths. The positive strip on the upper substrate is connected vertically through a cylindrical via to the subsequent strip on the lower side of the substrate. The negative strip on the lower side is similarly connected to the subsequent strip on the upper side. Hence, the positions of the positive and negative strips alternate as shown in Fig. 4.4(c). The details of the design method for such a microstrip phase inverter structure are presented in [19].

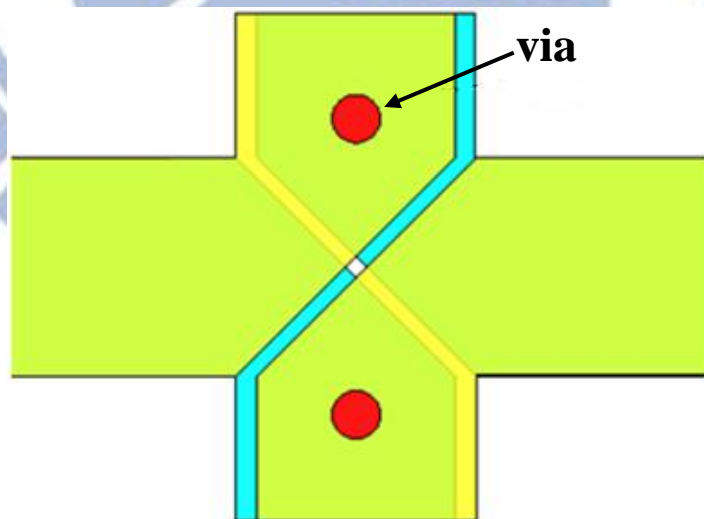


Fig. 4.4(a) Top view of the inverted balanced microstrip line.

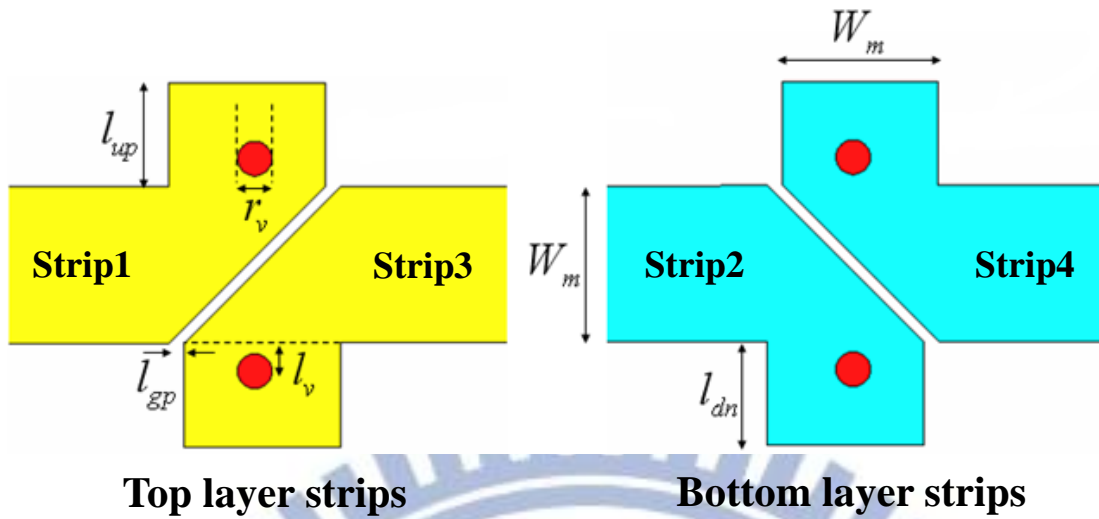


Fig. 4.4(b) The width of the bent stubs:  $W_m = 1.35$  mm; the length of the bent stubs:  $l_{up} = 0.9$  mm and  $l_{dn} = 0.9$  mm; the gap width:  $l_{gp} = 0.13$  mm; the diameter of vias:  $r_v = 0.3$  mm; the slanted angle is 45 degrees.

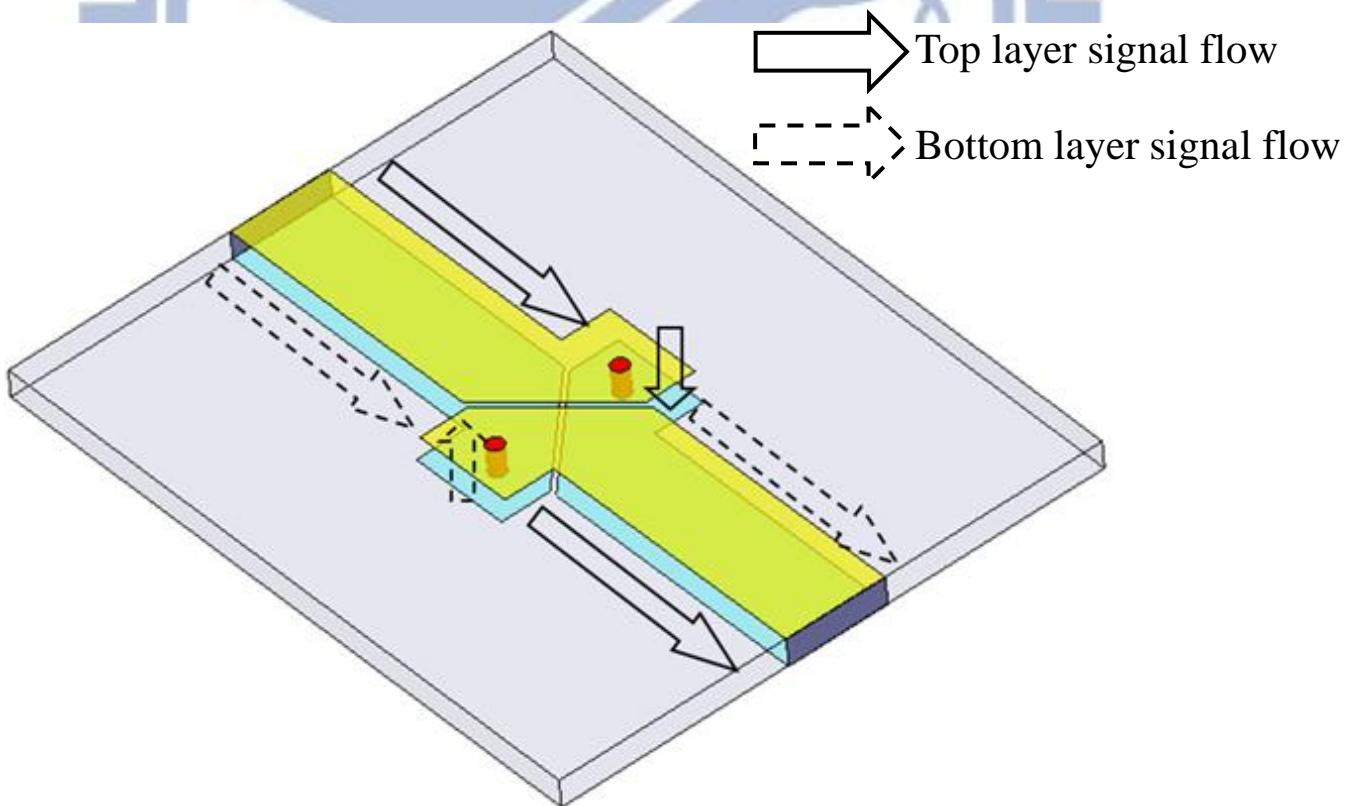


Fig. 4.4(c) Signal flow graph of the inverted balanced microstrip line.



Using a balanced-microstrip-line T-junction power divider with inverted balanced microstrip lines substituted for balanced microstrip lines in one of the two output ports, two pairs of broadband planar baluns can be formed as shown in Fig 4.5.

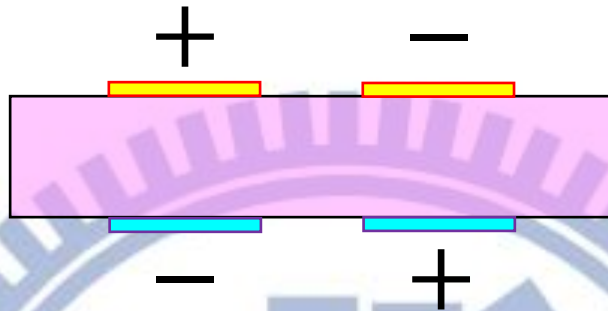


Fig. 4.5 Two pairs of the broadband planar baluns on the upper and lower substrate sides, respectively.

The balun on the lower side of the substrate produces a disturbed radiation because no background metal plane is located beneath the single-conductor strip structure. Fig. 4.2(a) depicts a method for preventing such disturbed radiation pattern. The strips of the balun on the lower side of the substrate are connected to each other and returned back to the original ground plane of the microstrip line. Hence, only the balun on the upper side of the substrate feeds the single-conductor strip and a closed metal loop is formed on the lower side of the substrate. As shown in Fig. 4.2(c), on this closed metal loop, two semicircles beneath the two feeding strips are etched out with diameters equal to the widths of the feeding strips, respectively, to enhance the electrical field transition from feeding points to the single-conductor strip.

### 4.1.2 Performance of Single-Conductor Strip Leaky-Wave Antenna

Fig. 4.6 shows the geometry of the single-conductor strip leaky-wave antenna with a strip width of  $w=32.5\text{mm}$  and a strip length of  $L=100\text{mm}$ , on a substrate with a dielectric constant of  $\epsilon_r=3.55$  and a thickness of  $h=0.508\text{mm}$ . The substrate used to design this antenna is Rogers 4003. The geometry of the broadband feeding structure of this antenna is shown in Fig. 4.7, and the S parameter magnitudes and phase difference of this broadband feeding structure are plotted in Fig. 4.8(a) and Fig. 4.8(b), respectively. The return loss is always below  $-10\text{ dB}$  from  $3\text{ GHz}$  to  $8\text{ GHz}$  and insertion losses are between  $-3.4\text{ dB}$  and  $-3.8\text{ dB}$  over the frequency range of  $5\text{ GHz}$  to  $6\text{ GHz}$ . The phase imbalance is calculated as  $180^\circ - |\angle(S_{21}) - \angle(S_{31})|$ , and is shown to be less than  $10^\circ$  from  $3\text{ GHz}$  to  $8\text{ GHz}$ . Within the frequency from  $5\text{ GHz}$  to  $6\text{ GHz}$ , the phase imbalance is less than  $2^\circ$ . Careful attention is paid to the feeding points in the edge of strip to exploit the leaky-wave bandwidth as much as possible. As shown in Fig. 4.6, the feeding points are offset from the edges by  $8.075\text{ mm}$ . The length of leaky-wave antenna is related to the attenuation constant  $\alpha$  and can be determined by  $e^{-2\alpha L} < 0.01$  (the inequality ignores dissipative losses in the structure). This design is call for a 99% radiation efficiency [9].

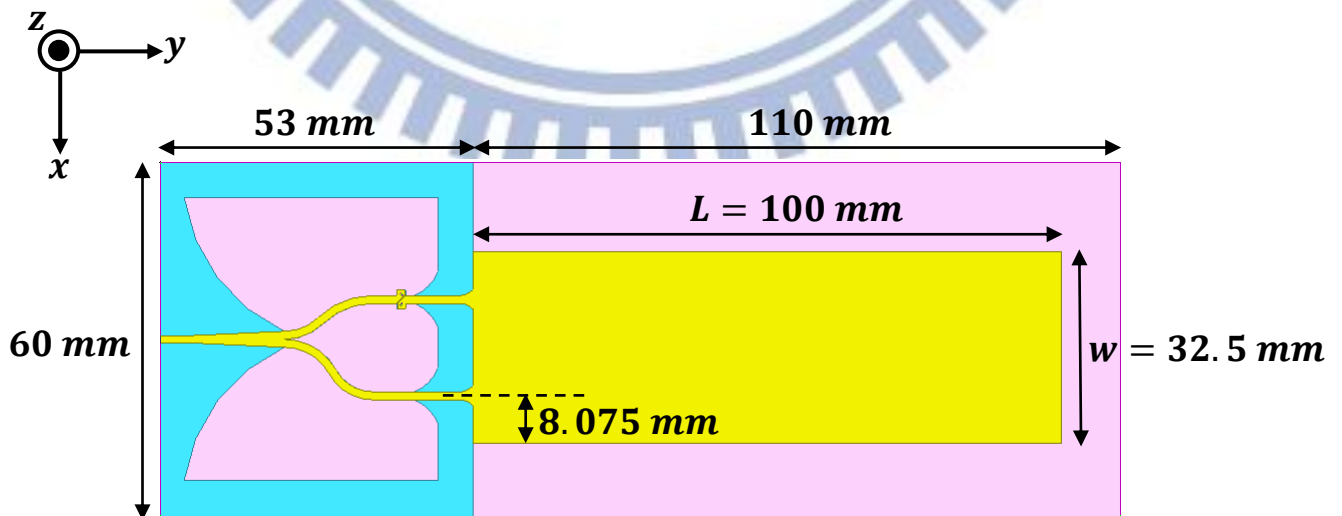


Fig. 4.6 Geometry of the single-conductor strip leaky-wave antenna.

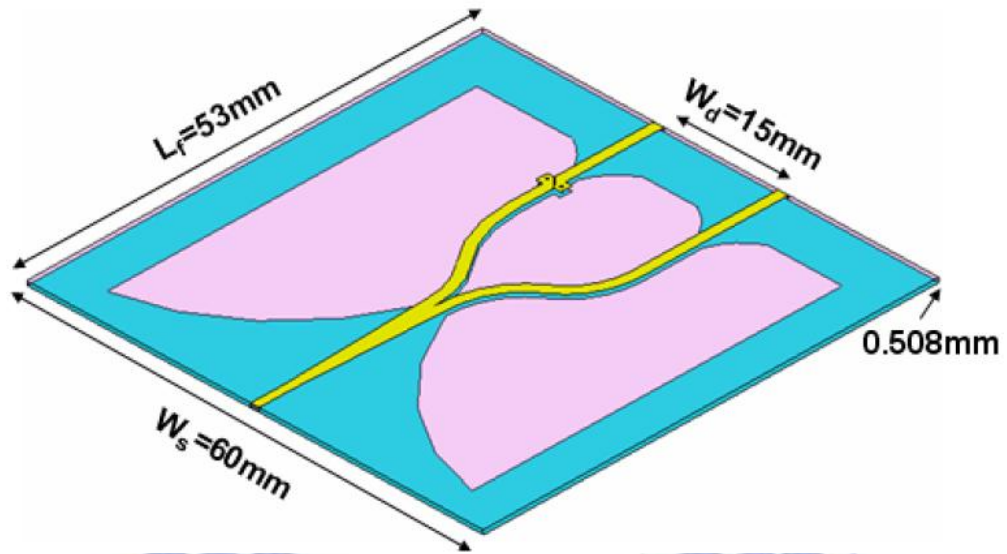


Fig. 4.7(a) Side view of the broadband planar feeding structure.

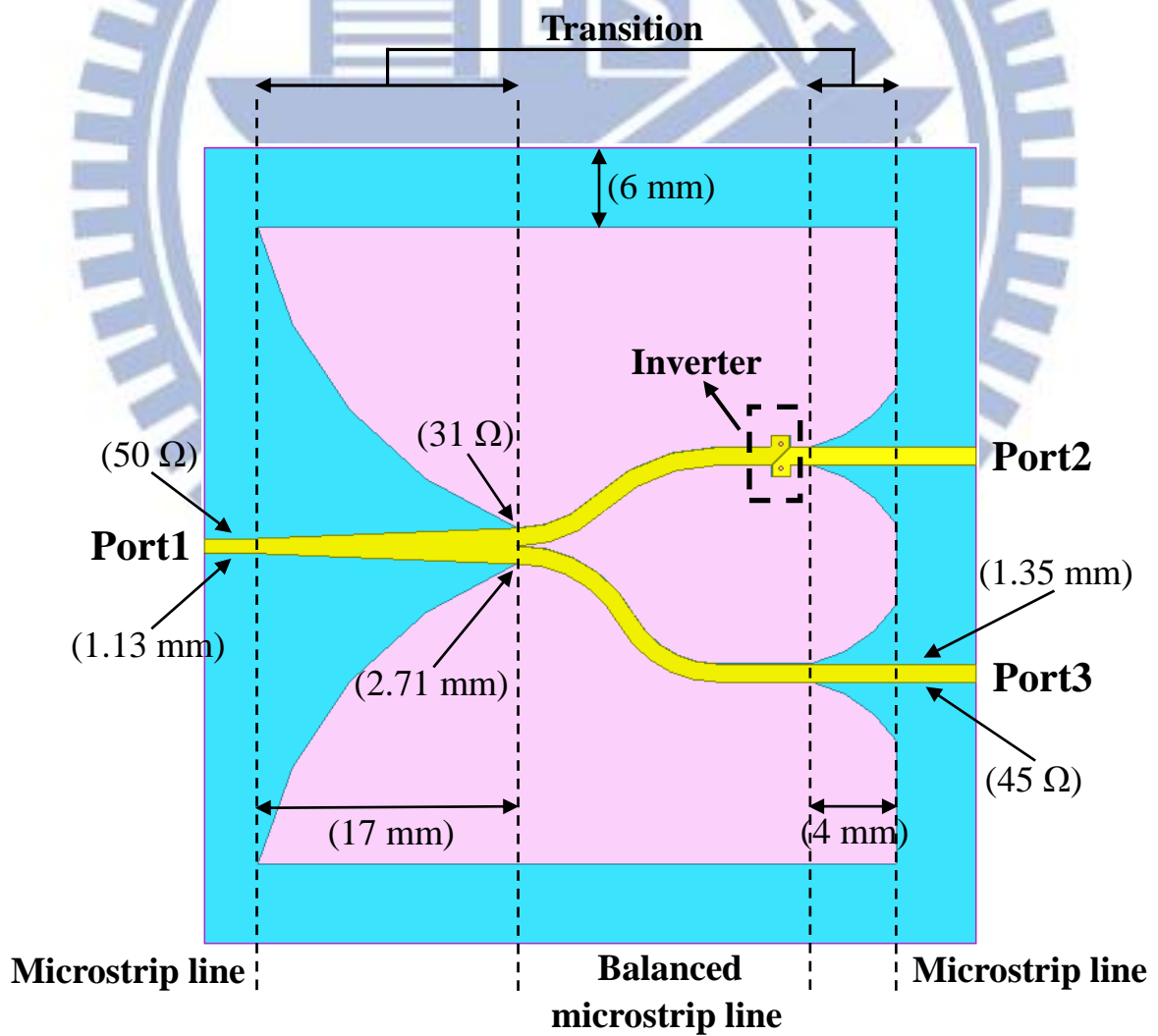


Fig. 4.7(b) Top view of the broadband planar feeding structure.

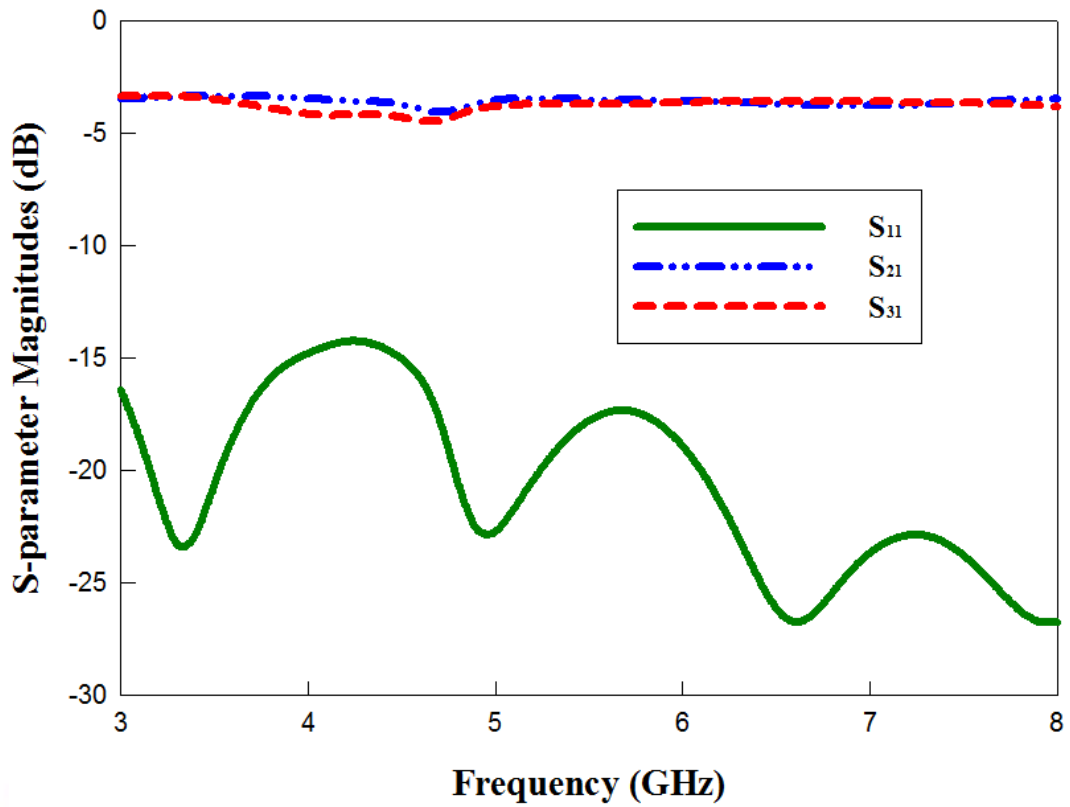


Fig. 4.8(a) Simulated S-parameter magnitudes of the broadband planar feeding structure.

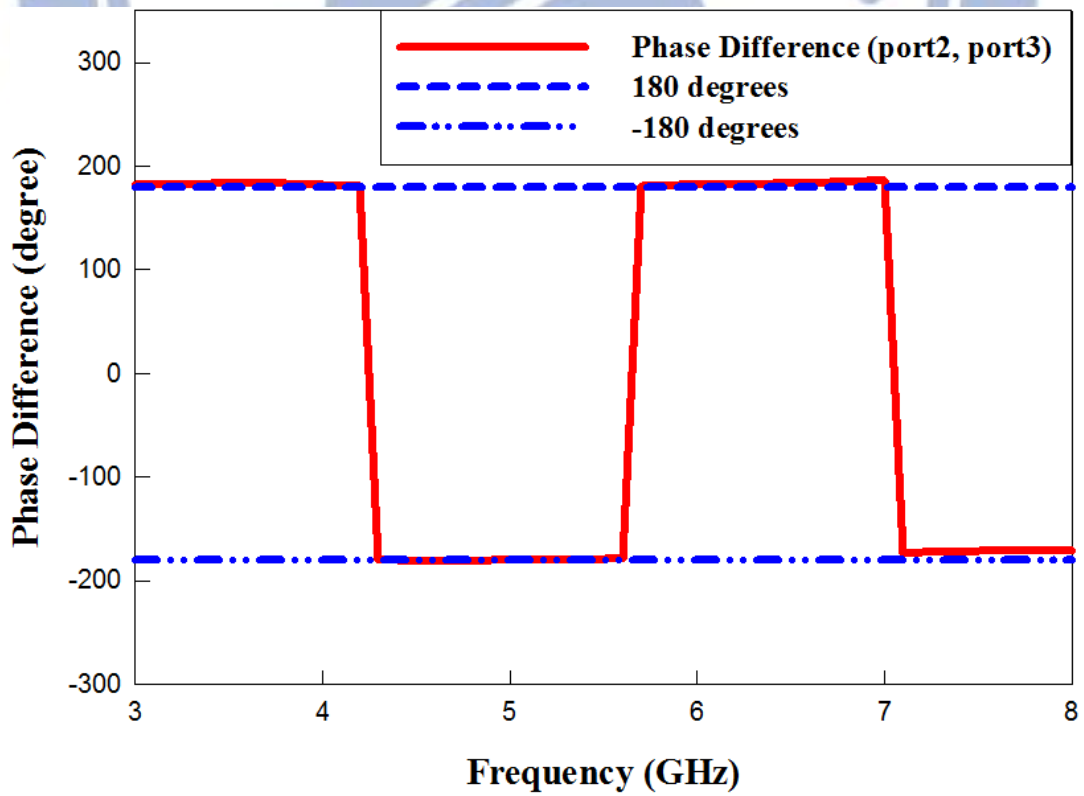


Fig. 4.8(b) Simulated phase difference of the broadband planar feeding structure.

The propagation constant of the single-conductor strip leaky-wave antenna is decided by the strip width  $w$ , the thickness  $h$  of the substrate, and the dielectric constant  $\epsilon_r$ . Using the SDA discussed previously, we obtain the normalized phase constant  $\beta$  and the normalized attenuation constant  $\alpha$  of the first higher-order leaky mode of the single-conductor strip leaky-wave antenna, as shown in Fig. 4.9. For the leaky-wave antenna structure, the space-wave radiation roughly starts at a frequency that the real power propagating starts to exceed the imaginary power, and ends when  $\beta/k_0 > 1$  [11]. Therefore, the radiation region of this first higher-order leaky mode is from 2.8 GHz to 7 GHz. According to Fig. 4.9, the value of the normalized phase constant ranges from 0.91 to 1 in the space-wave leaky region; this means that the main beam of this antenna is fixed in the end-fire direction over a broadband region.

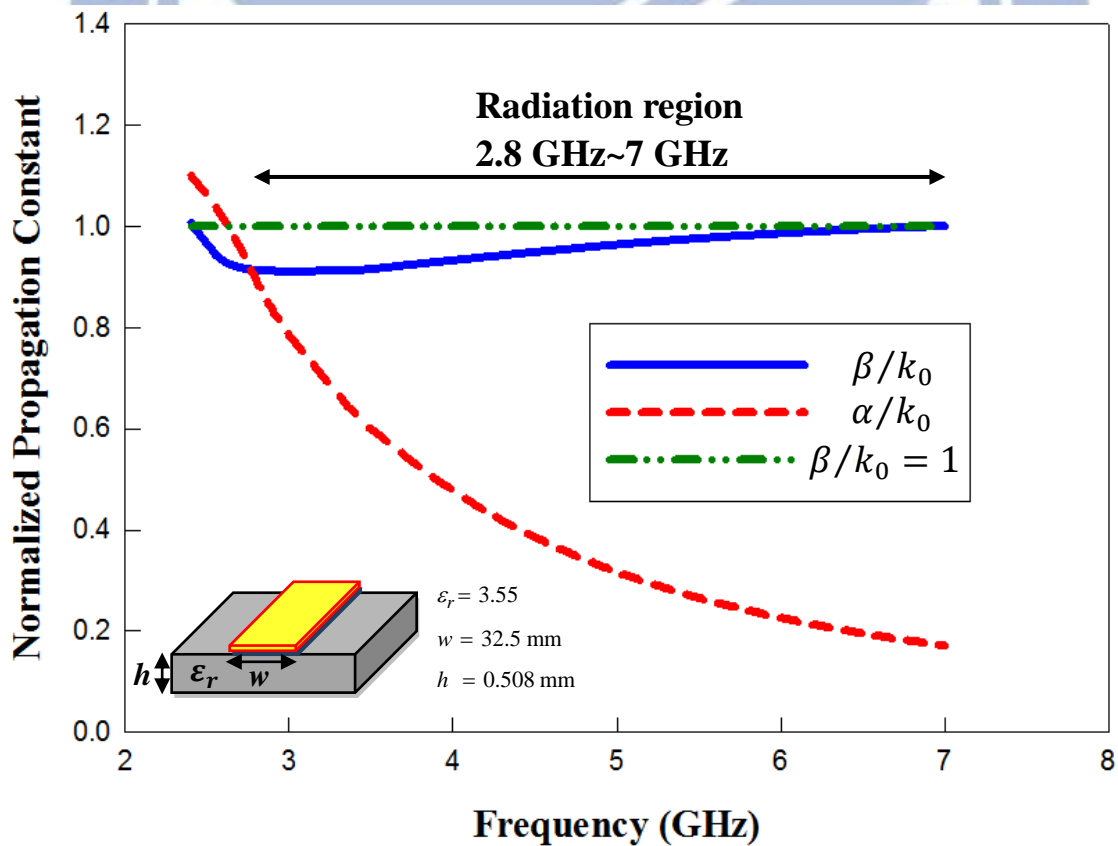


Fig. 4.9 Normalized propagation constant of the single-conductor strip structure with a strip width of  $w = 32.5\text{mm}$ , a dielectric constant of  $\epsilon_r = 3.55$ , and a thickness of  $h = 0.508\text{mm}$ .

As shown in Fig. 4.10, the simulated return loss of this single-conductor strip leaky-wave antenna is below -10 dB from 4.35 GHz to 6.85 GHz.

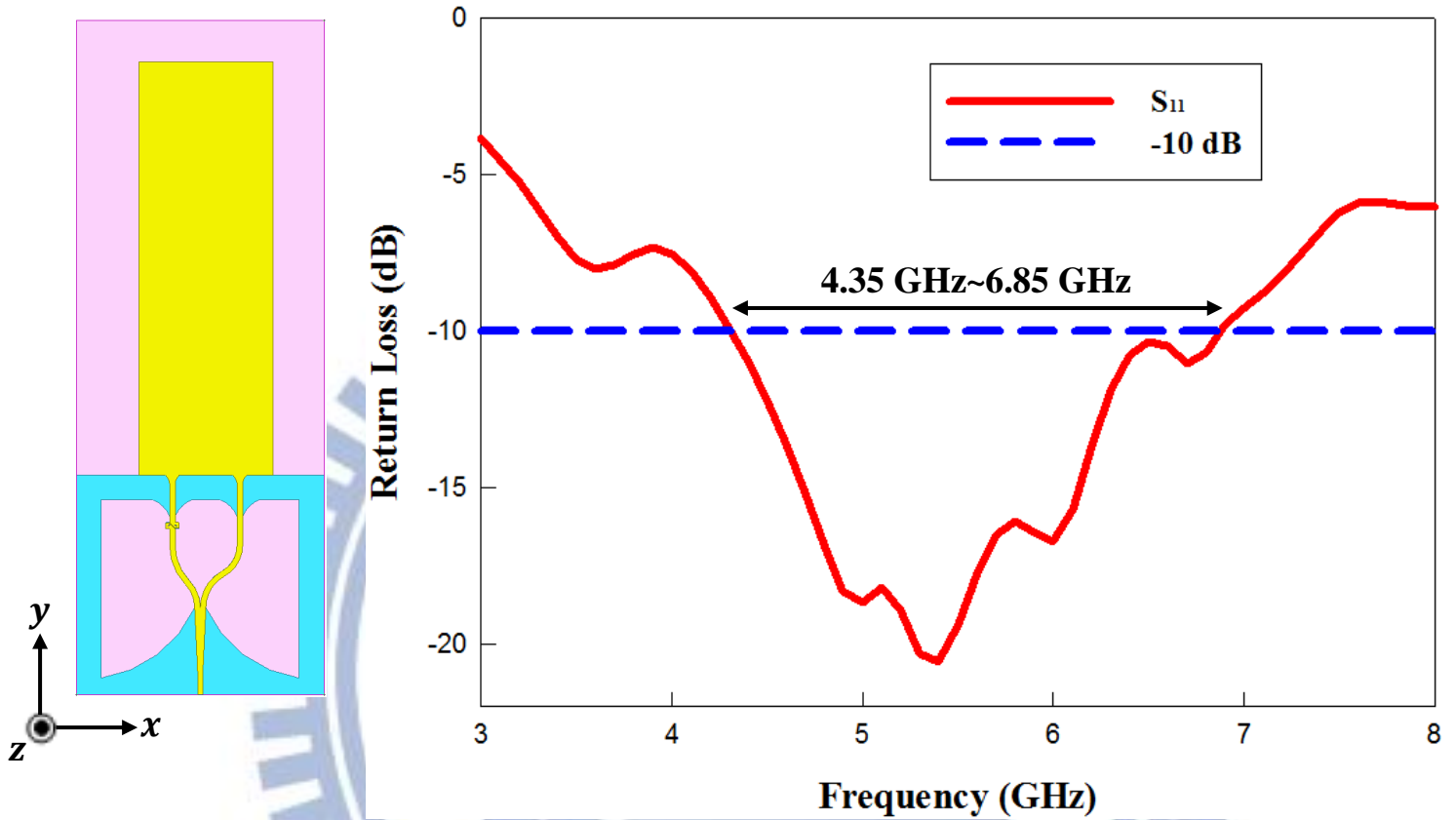


Fig. 4.10 Simulated return loss of the single-conductor strip leaky-wave antenna.

Fig. 4.11(a)-(h) present the simulated E-plane ( $x$ - $y$  plane) and H-plane ( $y$ - $z$  plane) radiation patterns of this single-conductor strip leaky-wave antenna at 5.2 GHz, 5.4 GHz, 5.6 GHz, and 5.8 GHz, respectively. According to the simulated H-plane ( $y$ - $z$  plane) radiation patterns, we can see that the main beam of this antenna is always fixed in the end-fire direction as expected.

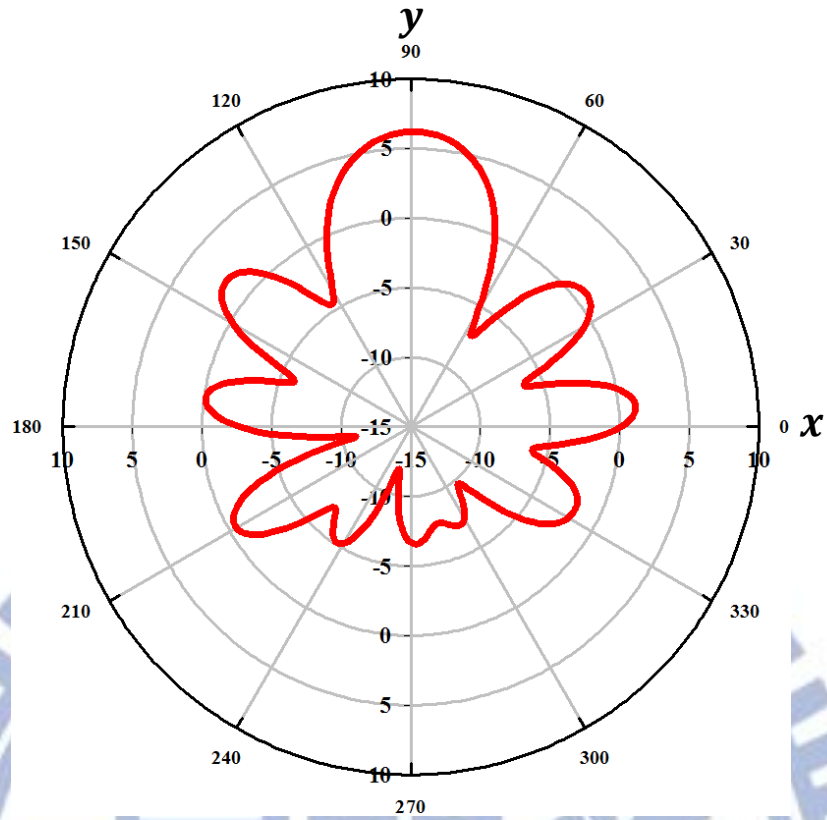


Fig. 4.11(a) Simulated E-plane ( $x$ - $y$  plane) radiation pattern of the single-conductor strip leaky-wave antenna with a gain of 6.24 dBi at 5.2 GHz.

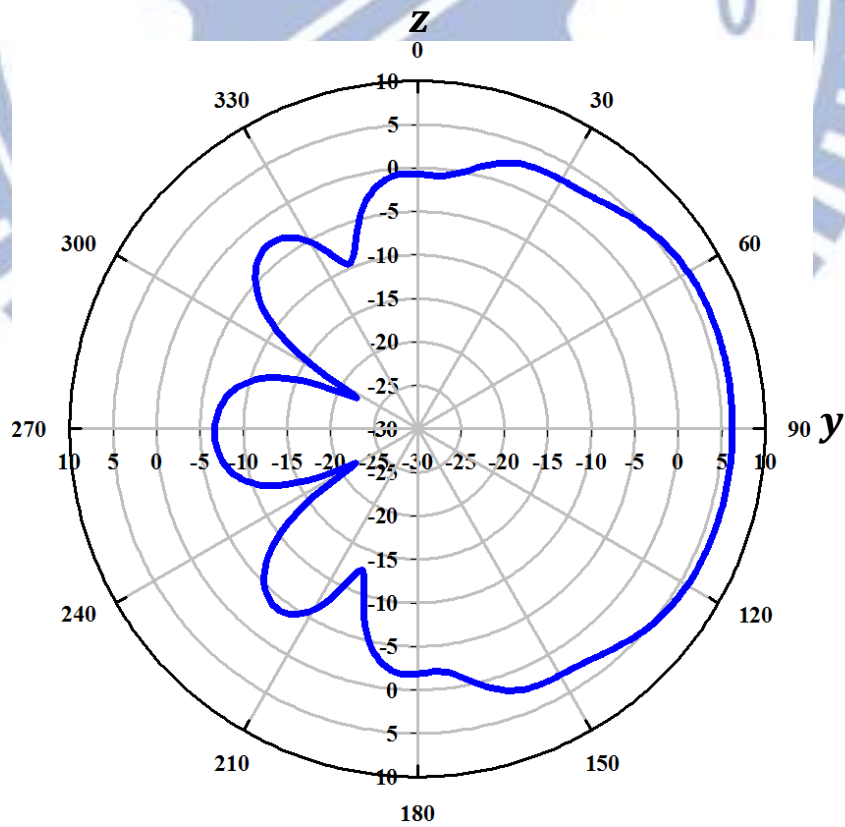


Fig. 4.11(b) Simulated H-plane ( $y$ - $z$  plane) radiation pattern of the single-conductor strip leaky-wave antenna at 5.2 GHz.

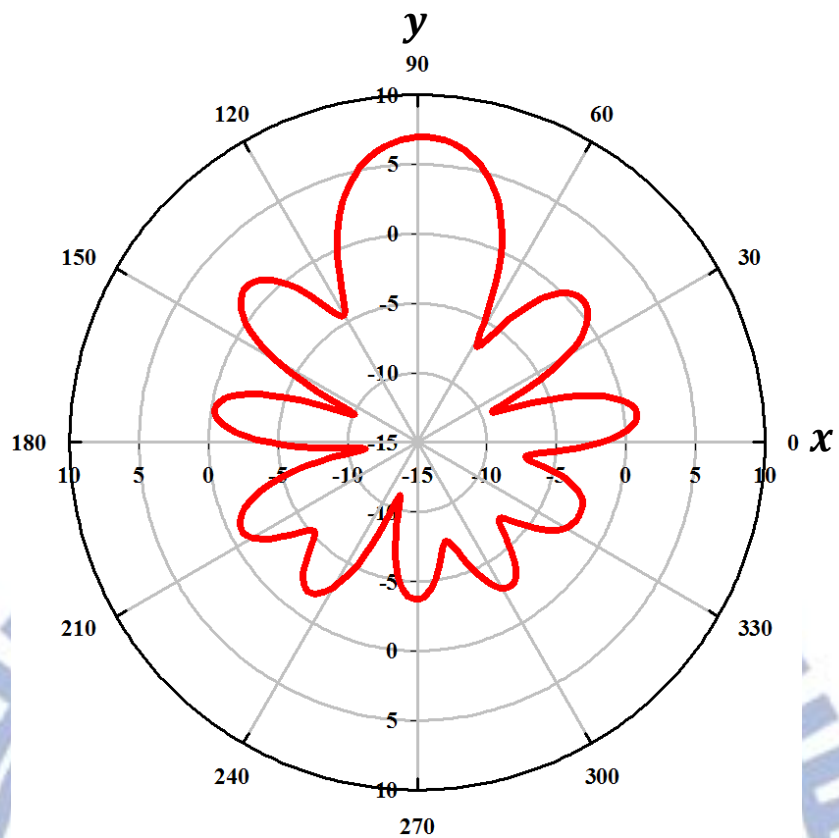


Fig. 4.11(c) Simulated E-plane ( $x$ - $y$  plane) radiation pattern of the single-conductor strip leaky-wave antenna with a gain of 6.96 dBi at 5.4 GHz.

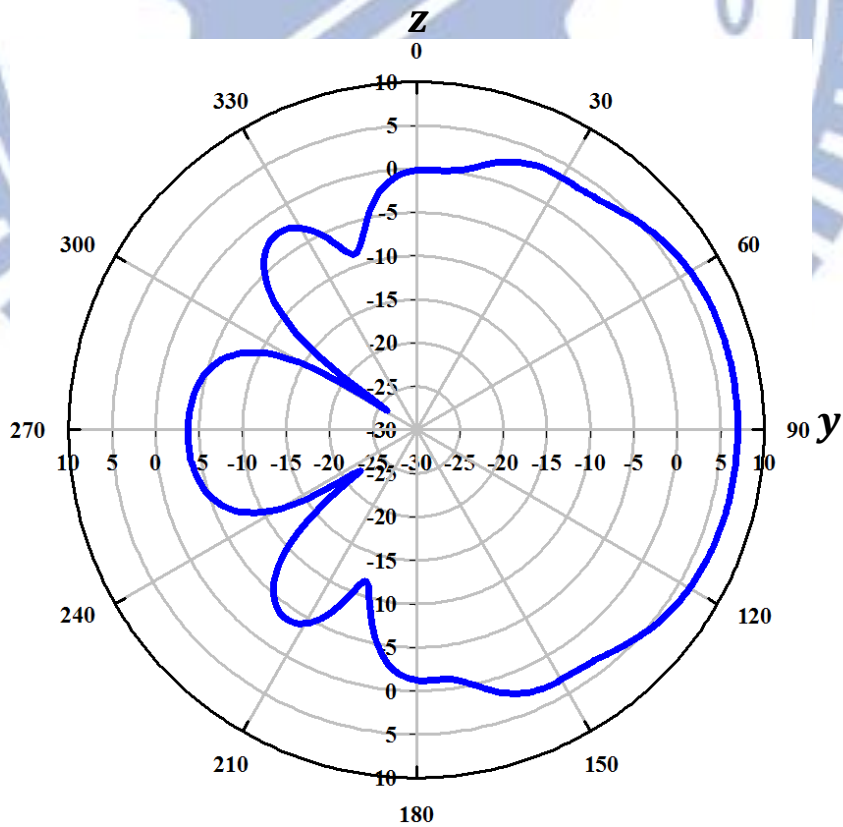


Fig. 4.11(d) Simulated H-plane ( $y$ - $z$  plane) radiation pattern of the single-conductor strip leaky-wave antenna at 5.4 GHz.



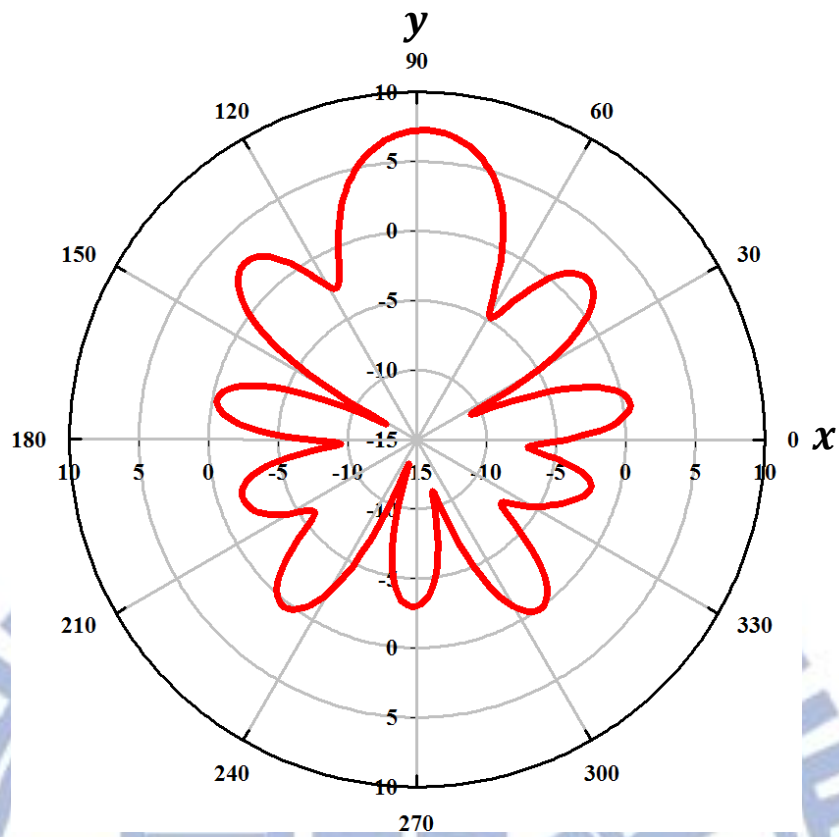


Fig. 4.11(e) Simulated E-plane ( $x$ - $y$  plane) radiation pattern of the single-conductor strip leaky-wave antenna with a gain of 7.23 dBi at 5.6 GHz.

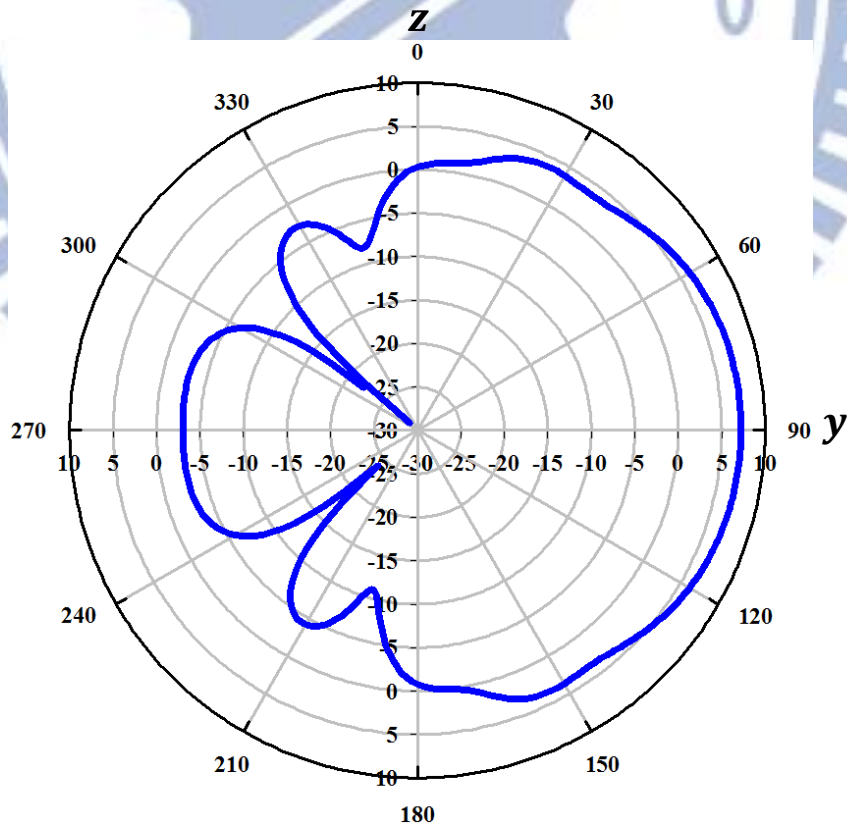


Fig. 4.11(f) Simulated H-plane ( $y$ - $z$  plane) radiation pattern of the single-conductor strip leaky-wave antenna at 5.6 GHz.

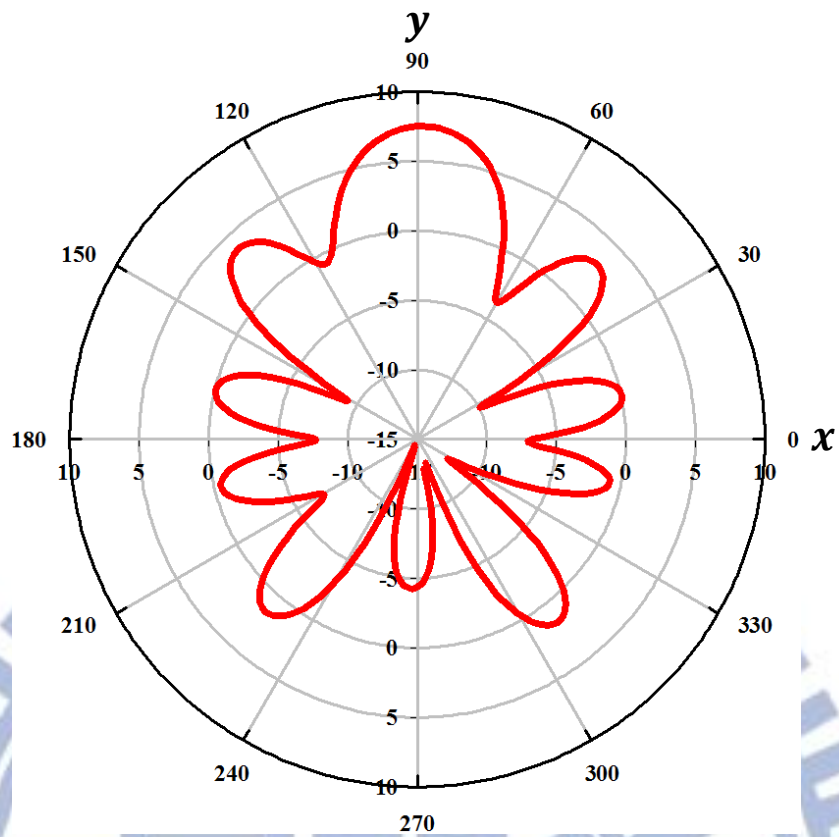


Fig. 4.11(g) Simulated E-plane ( $x$ - $y$  plane) radiation pattern of the single-conductor strip leaky-wave antenna with a gain of 7.51 dBi at 5.8 GHz.

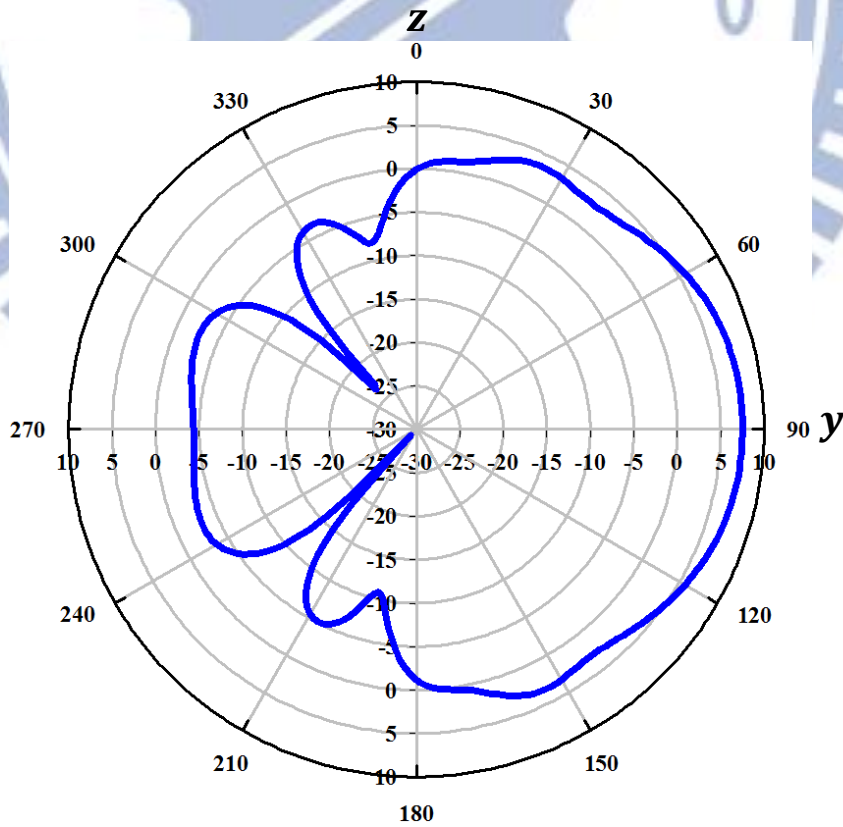


Fig. 4.11(h) Simulated H-plane ( $y$ - $z$  plane) radiation pattern of the single-conductor strip leaky-wave antenna at 5.8 GHz.

## 4.2 REDUCTION OF THE BACK LOBE

### 4.2.1 Consideration during Design Procedure

From the radiation patterns of our single-conductor strip leaky-wave antenna, we observe that the back lobe is quite large. After analyzing the single-conductor strip leaky-wave antenna, we conclude that the feeding structure of this antenna causes this undesired effect. As shown in Fig. 4.12, one of the reasons why the feeding structure produces this undesired radiation is the circumfluence fabrication of the feeding structure [17]. In order to alleviate this undesired radiation from the feeding structure, we turn two broadband planar baluns upside down and attach themselves to the left and right sides of the feeding structure, respectively. Fig. 4.13 shows the geometry of this modified single-conductor strip leaky-wave antenna.

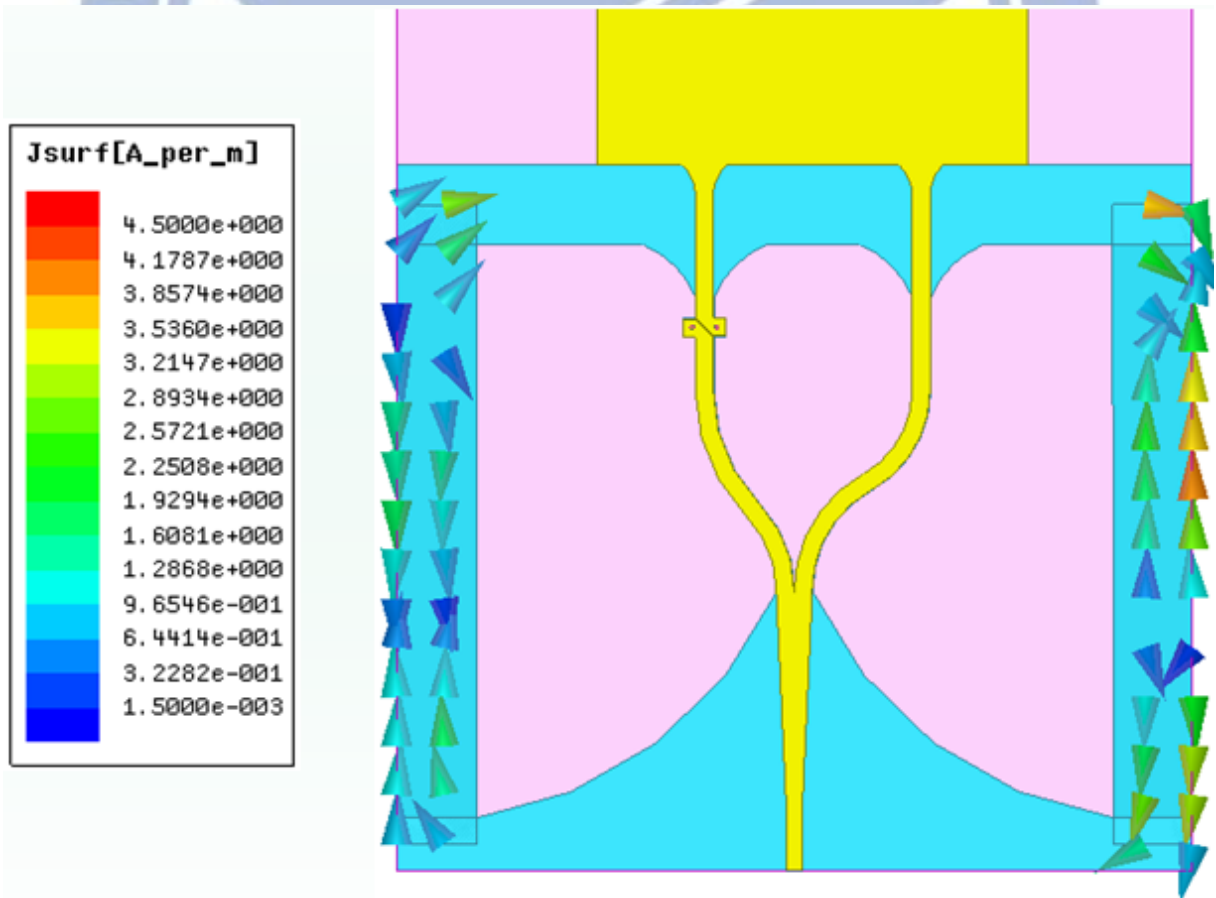


Fig. 4.12 Surface current in the current returning paths in the ground plane.

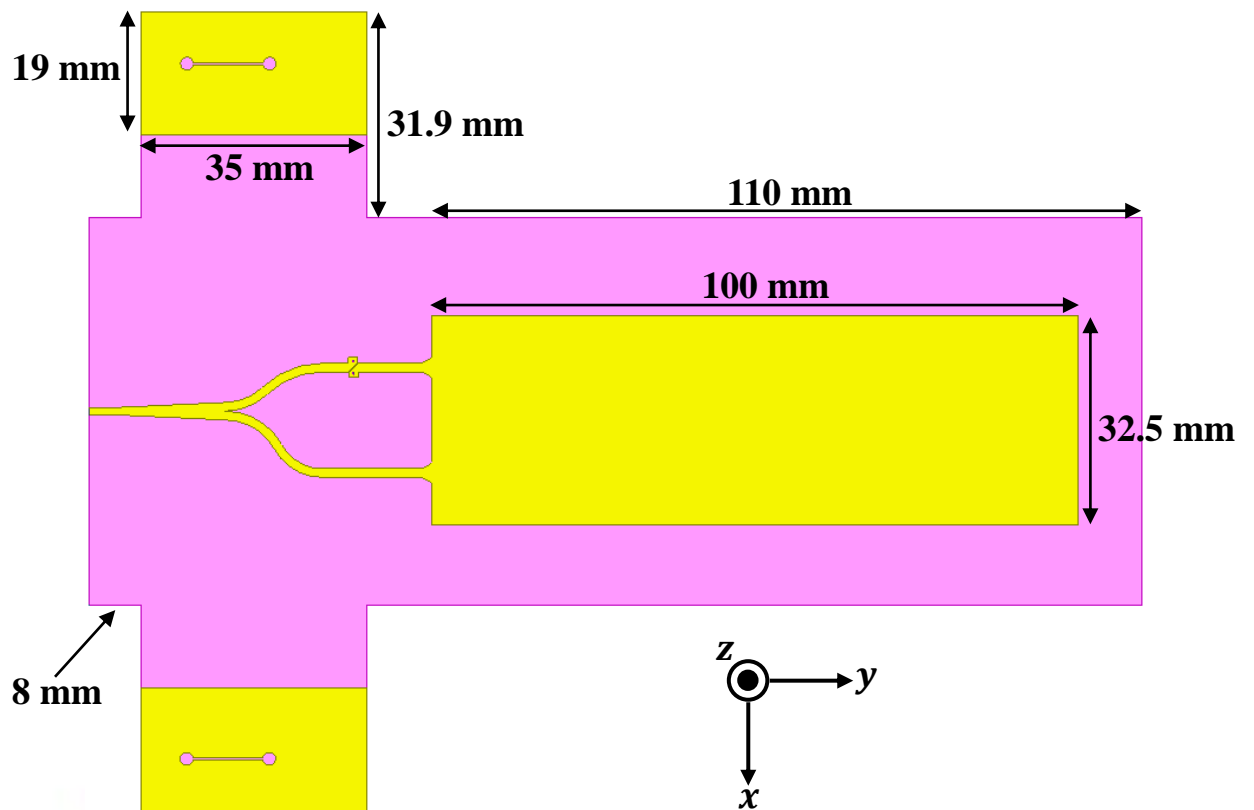


Fig. 4.13(a) Top view of the modified single-conductor strip leaky-wave antenna.

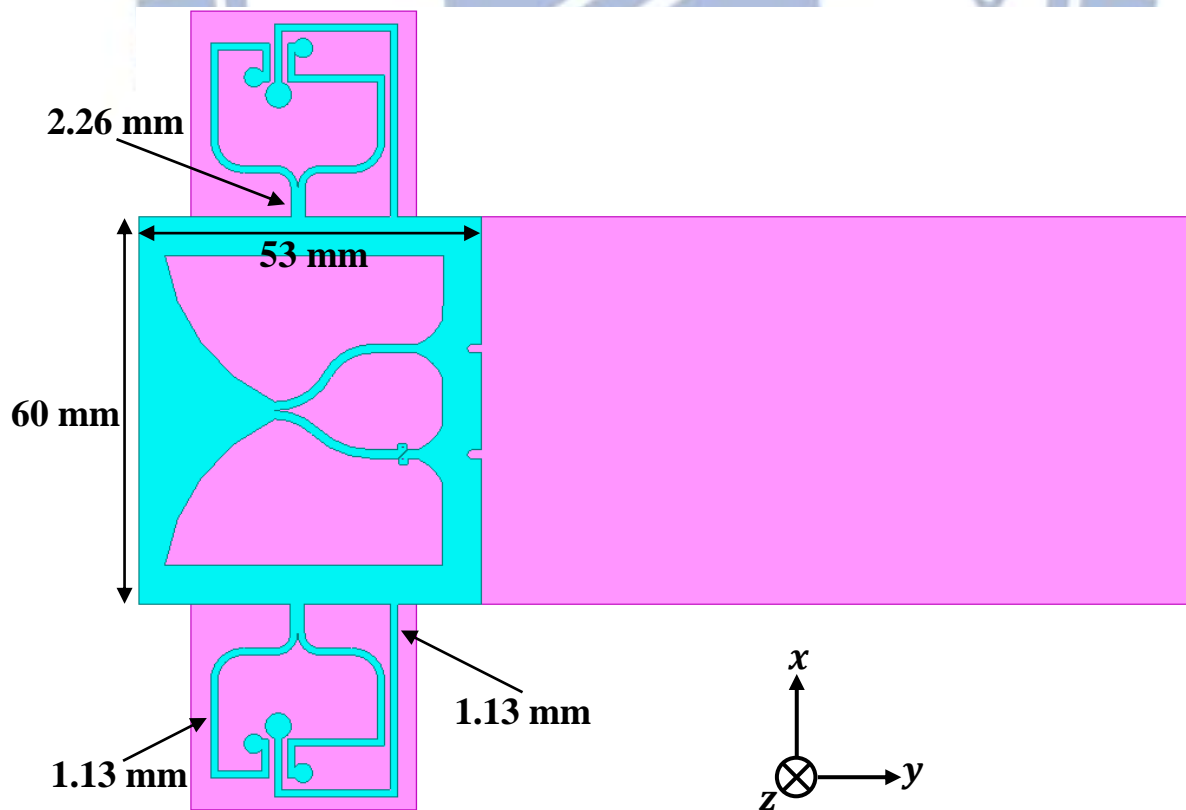


Fig. 4.13(b) Back view of the modified single-conductor strip leaky-wave antenna.

#### 4.2.2 Broadband Planar Balun

When two microstrip-to-slotline transitions are connected back-to-back as shown in Fig. 4.14(a), an additional  $180^\circ$  phase shift is introduced in the signal path [20]. This can be explained qualitatively by considering the  $\mathbf{E}$ -field distribution associated with the microstrip-to-slotline transition. Referring to Fig. 4.14(b), we note that the electric field in the input microstrip line (near the transition) is in the  $-y$ -direction. This produces a slotline wave with the  $\mathbf{E}$ -field in the  $x$ -direction. At the second transition an  $x$ -directed component of  $\mathbf{E}$  will cause the  $\mathbf{E}$ -field in the output microstrip to lie in the  $y$ -direction. Thus, in addition to the phase change introduced by the line length, the  $\mathbf{E}$ -field direction changes from  $-y$  to  $y$ , which amounts to an equivalent  $180^\circ$  phase change. This phase change is independent of frequency (at least in a first-order analysis) and can thus be used in wide-band circuits.

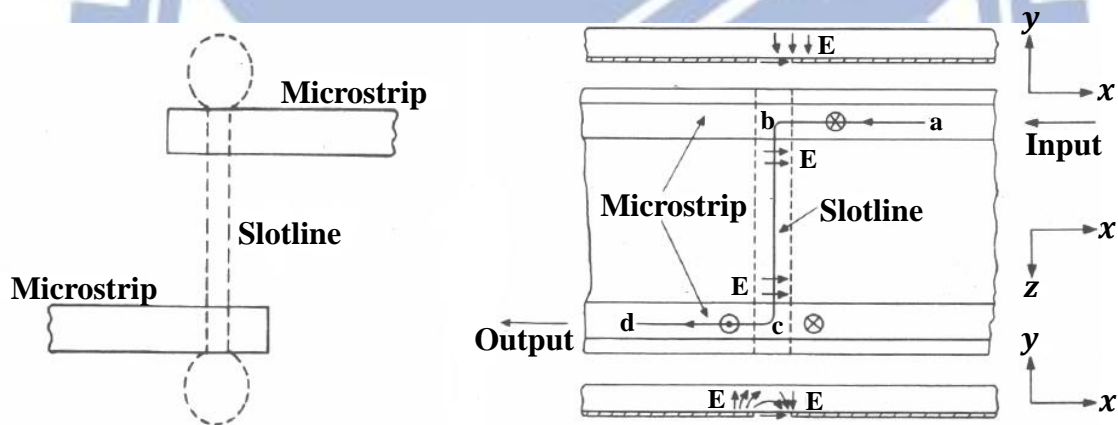


Fig. 4.14(a) Two microstrip-to-slotline transitions connected back-to-back for  $180^\circ$  phase change and (b) mechanism for  $180^\circ$  phase change.

Fig. 4.15 shows the geometry of the broadband planar balun [18]. The return loss is always below  $-10$  dB from 2.45 GHz to 5.85 GHz. The magnitude difference has a maximum 0.55 dB of separation over the frequency range of 3 GHz to 6 GHz. The phase imbalance is calculated as  $180^\circ - |\angle(S_{21}) - \angle(S_{31})|$ , and is shown to be less than  $10^\circ$  from 4.2 GHz to 6 GHz.

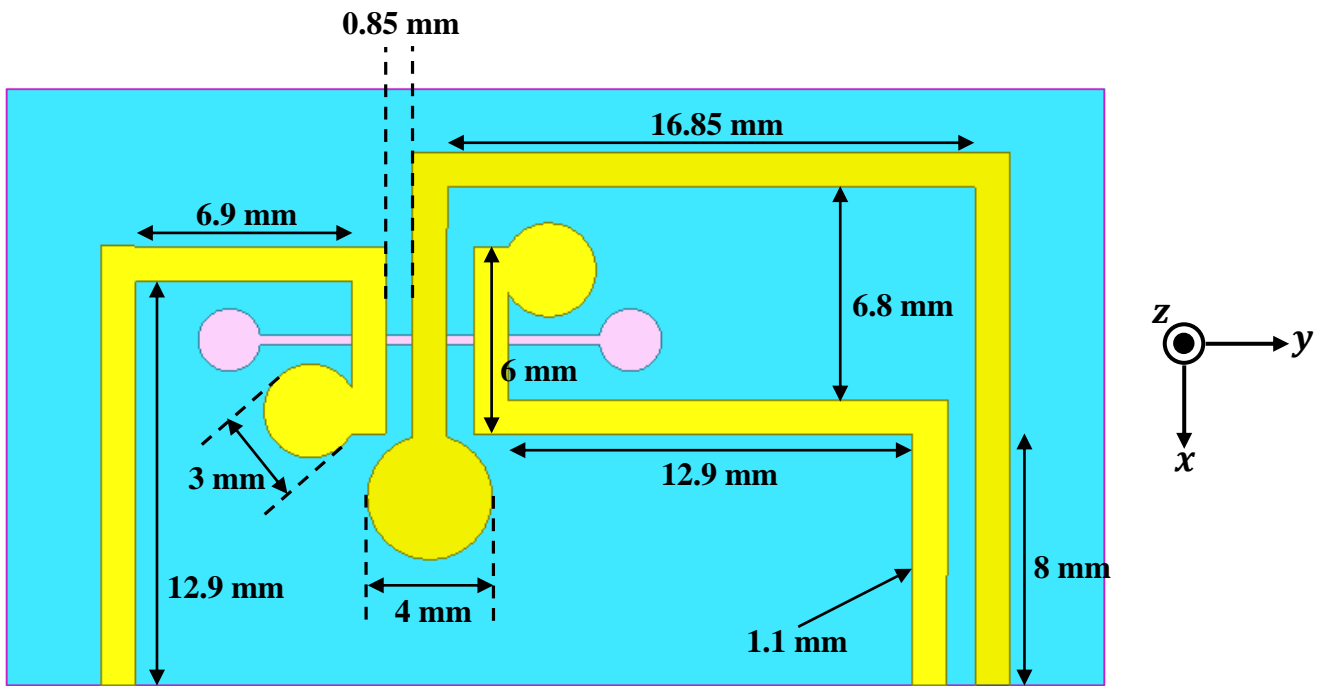


Fig. 4.15(a) Top view of the broadband planar balun.

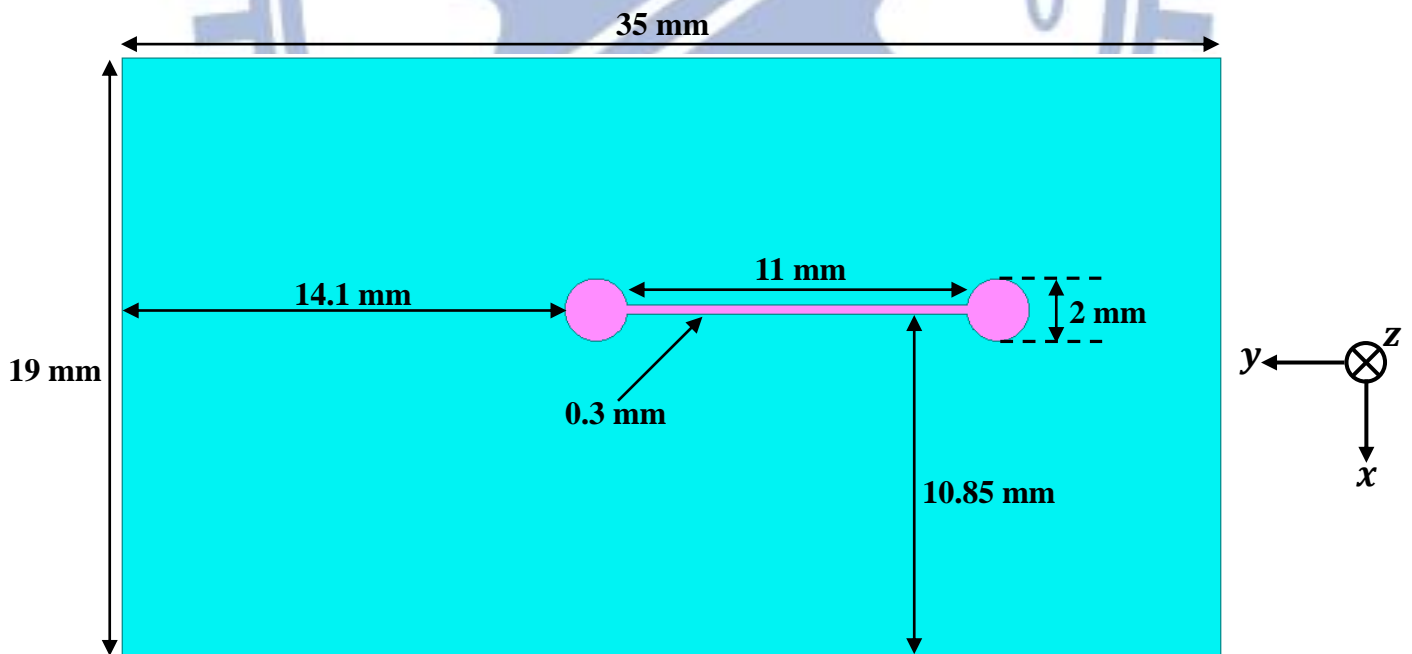


Fig. 4.15(b) Back view of the broadband planar balun.

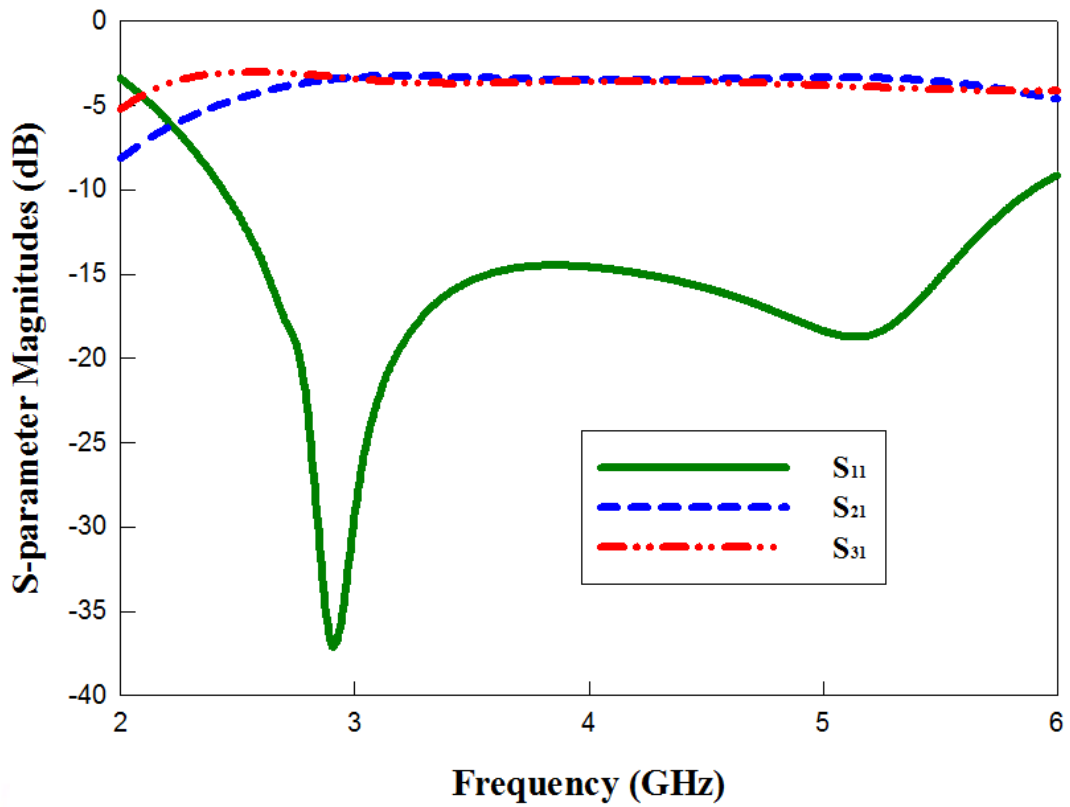


Fig. 4.16(a) Simulated S-parameter magnitudes of the broadband planar balun.

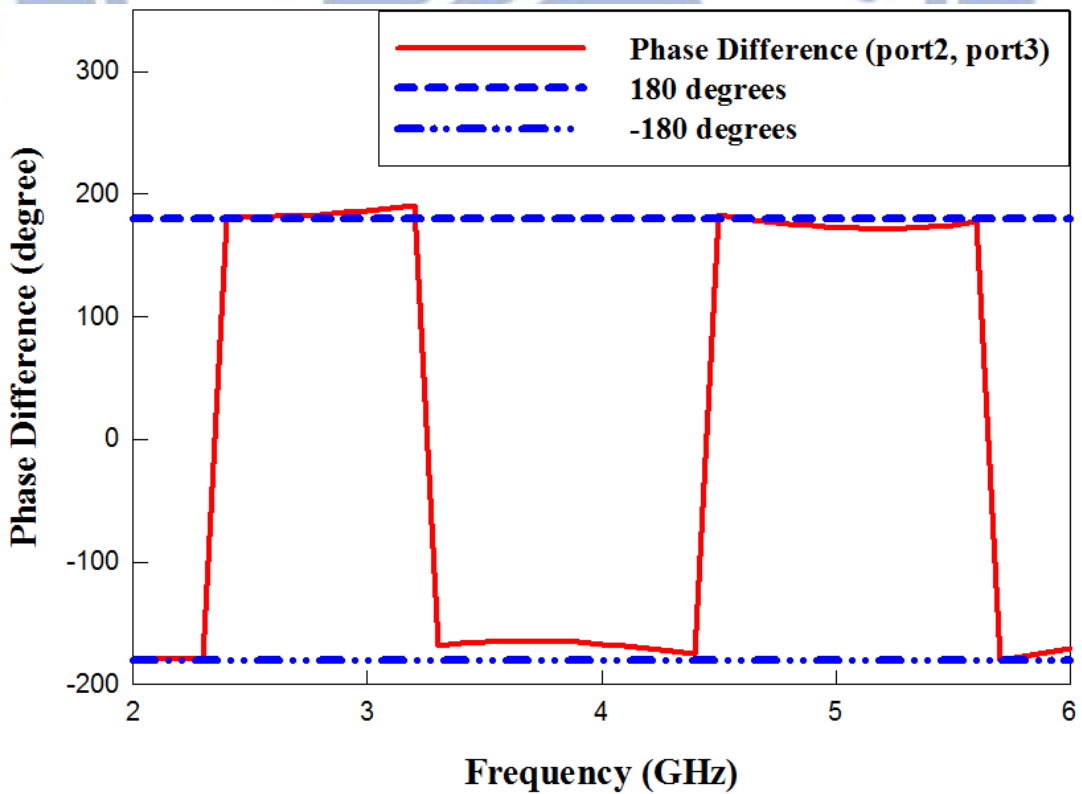


Fig. 4.16(b) Simulated phase difference of the broadband planar balun.

### 4.2.3 Comparison of Simulated Results Between Original and Modified Single-Conductor Strip Leaky-Wave Antenna

Fig. 4.17 shows the comparison of the surface currents in the current returning paths in the ground plane between the original and the modified single-conductor strip leaky-wave antenna, a significant decrease of the surface current is observed. The comparison of the simulated E-plane ( $x$ - $y$  plane) radiation patterns between the original antenna and the modified antenna from 5.2 GHz to 5.8 GHz is shown in Fig. 4.18(a)-(g). Table 4.1 shows the simulated results of the gain and the back lobe values. Table 4.2 shows the simulated results of the front-to-back ratio values, and the comparison between them are plotted in Fig. 4.19. Simulated results show significant improvement of the front-to-back ratio of this antenna.

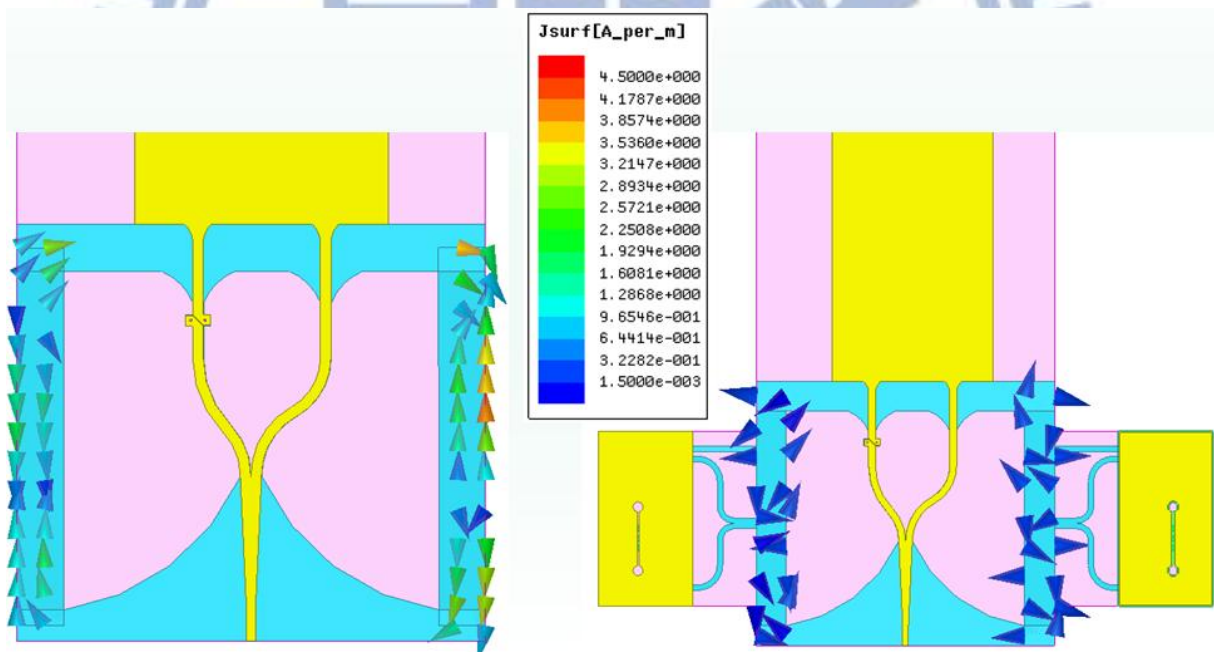


Fig. 4.17 Comparison of the simulated surface currents in the current returning paths in the ground plane between the original and the modified single-conductor strip leaky-wave



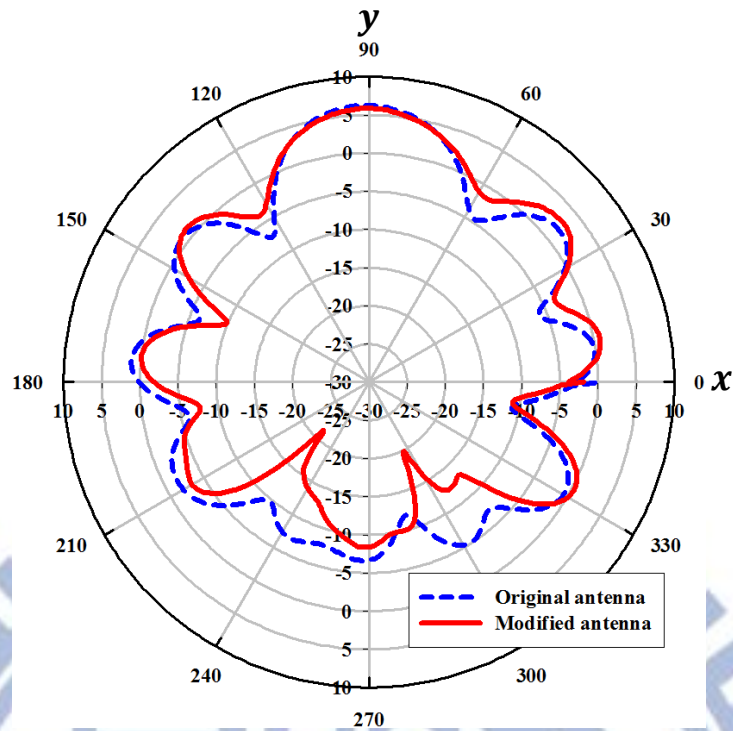


Fig. 4.18(a) Comparison of the simulated E-plane ( $x$ - $y$  plane) radiation patterns between the original and the modified single-conductor strip leaky-wave antenna at 5.2 GHz.

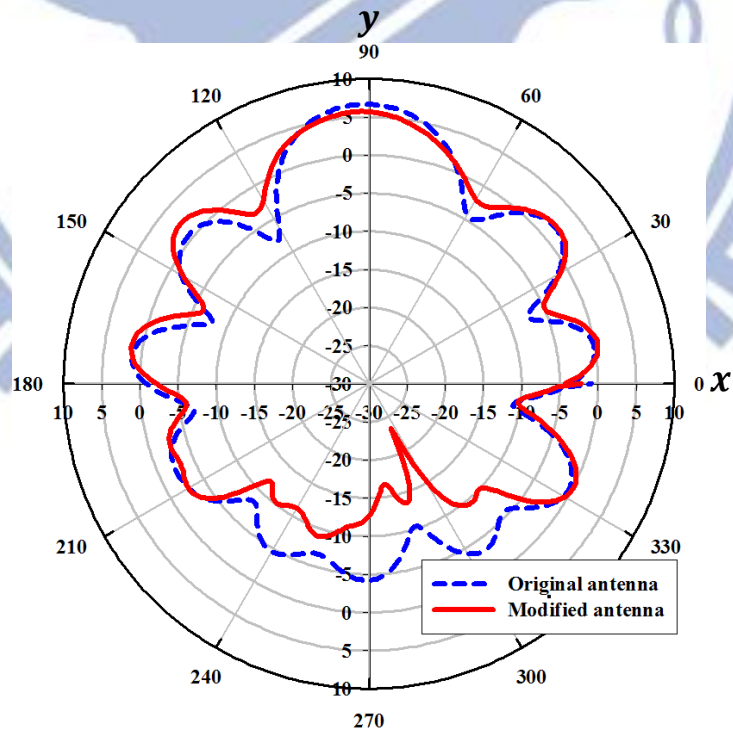


Fig. 4.18(b) Comparison of the simulated E-plane ( $x$ - $y$  plane) radiation patterns between the original and the modified single-conductor strip leaky-wave antenna at 5.3 GHz.

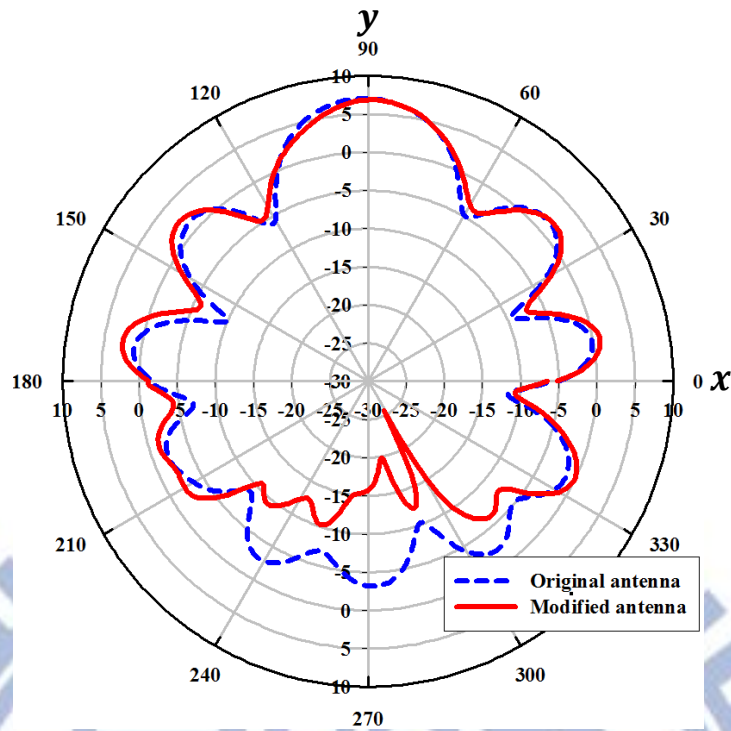


Fig. 4.18(c) Comparison of the simulated E-plane ( $x$ - $y$  plane) radiation patterns between the original and the modified single-conductor strip leaky-wave antenna at 5.4 GHz.

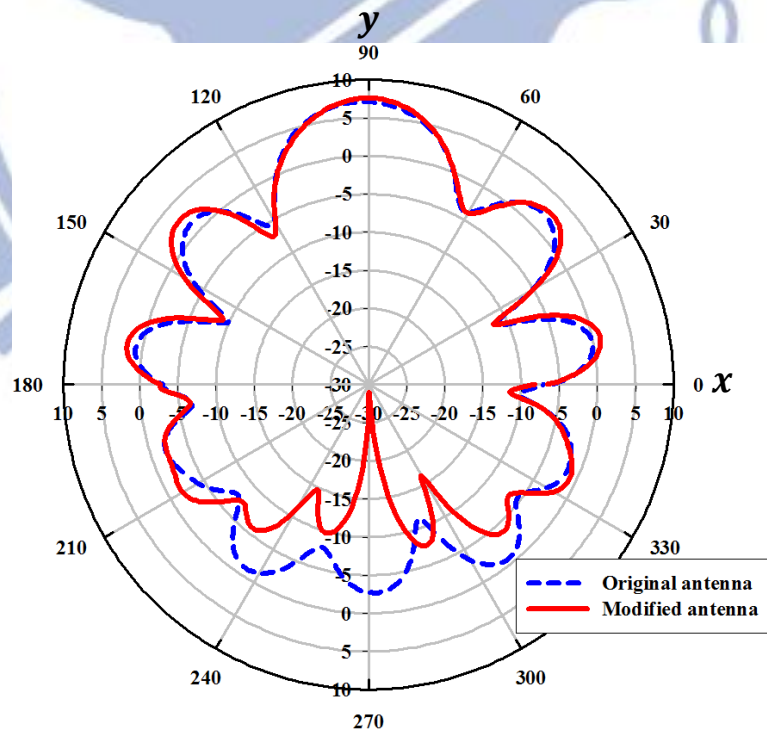


Fig. 4.18(d) Comparison of the simulated E-plane ( $x$ - $y$  plane) radiation patterns between the original and the modified single-conductor strip leaky-wave antenna at 5.5 GHz.

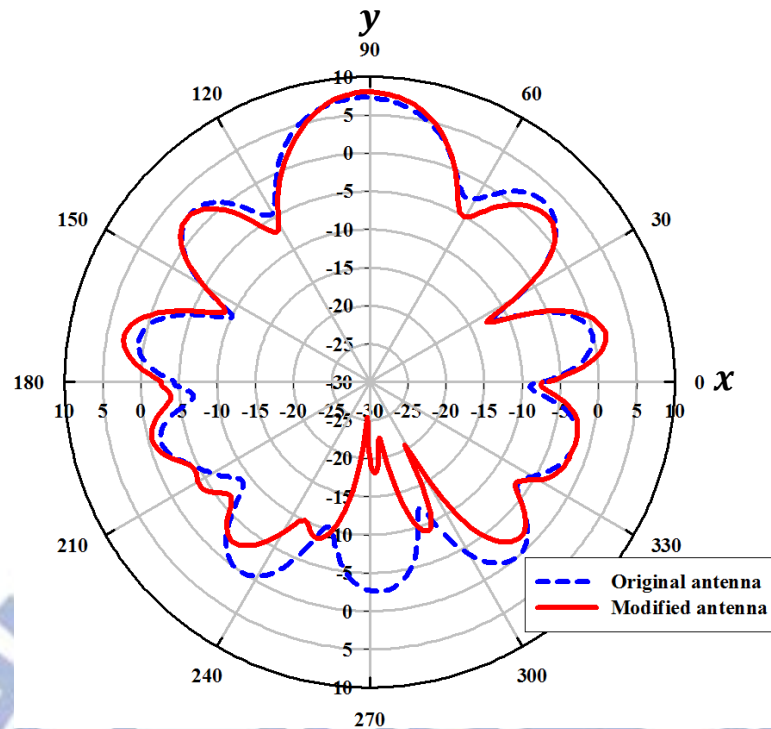


Fig. 4.18(e) Comparison of the simulated E-plane ( $x$ - $y$  plane) radiation patterns between the original and the modified single-conductor strip leaky-wave antenna at 5.6 GHz.

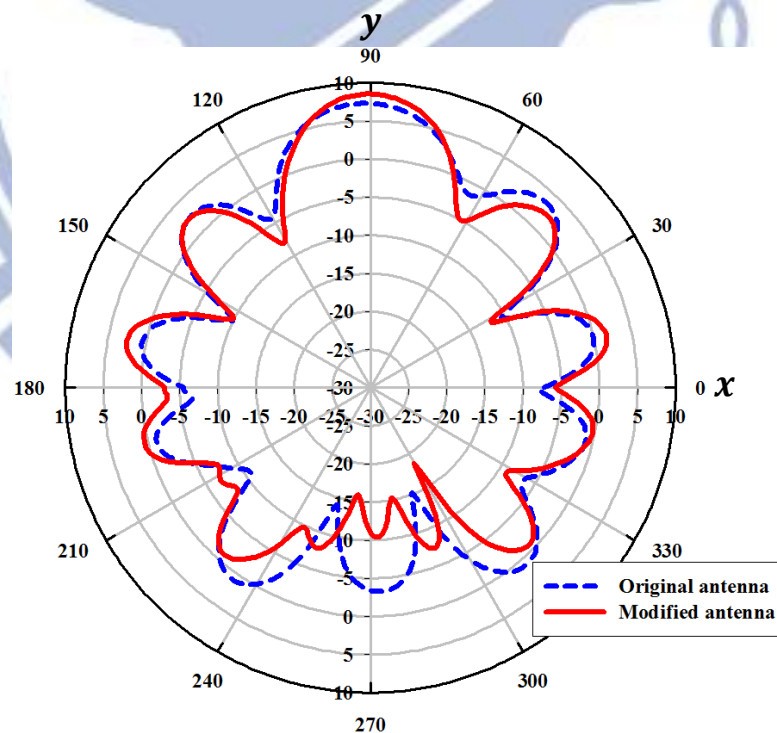


Fig. 4.18(f) Comparison of the simulated E-plane ( $x$ - $y$  plane) radiation patterns between the original and the modified single-conductor strip leaky-wave antenna at 5.7 GHz.

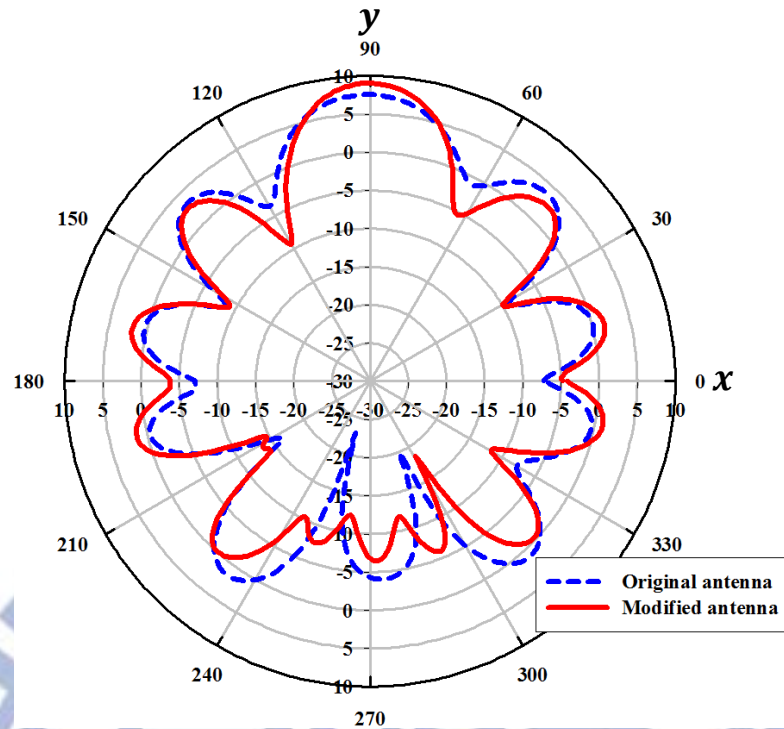


Fig. 4.18(g) Comparison of the simulated E-plane ( $x$ - $y$  plane) radiation patterns between the original and the modified single-conductor strip leaky-wave antenna at 5.8 GHz.

Table 4.1 Simulated gain and the back lobe of the original and the modified single-conductor strip leaky-wave antenna

Frequency (GHz)	5.2	5.3	5.4	5.5	5.6	5.7	5.8
Original antenna gain (dBi)	6.24	6.67	6.89	7.1	7.28	7.31	7.58
Modified antenna gain (dBi)	5.86	5.67	6.85	7.6	8	8.53	9.03
Original antenna back lobe (dBi)	-6.67	-4.2	-3.12	-2.66	-2.6	-3.29	-4.16
Modified antenna back lobe (dBi)	-8.38	-12.63	-15.93	-27.94	-19	-10.6	-6.54

Table 4.2 Simulated front-to-back ratio of the original and the modified single-conductor strip leaky-wave antenna

Frequency (GHz)	5.2	5.3	5.4	5.5	5.6	5.7	5.8
Original antenna front-to-back ratio (dB)	12.91	10.87	10.01	9.76	9.88	10.6	11.74
Modified antenna front-to-back ratio (dB)	14.24	18.3	22.78	35.54	27	19.13	15.57

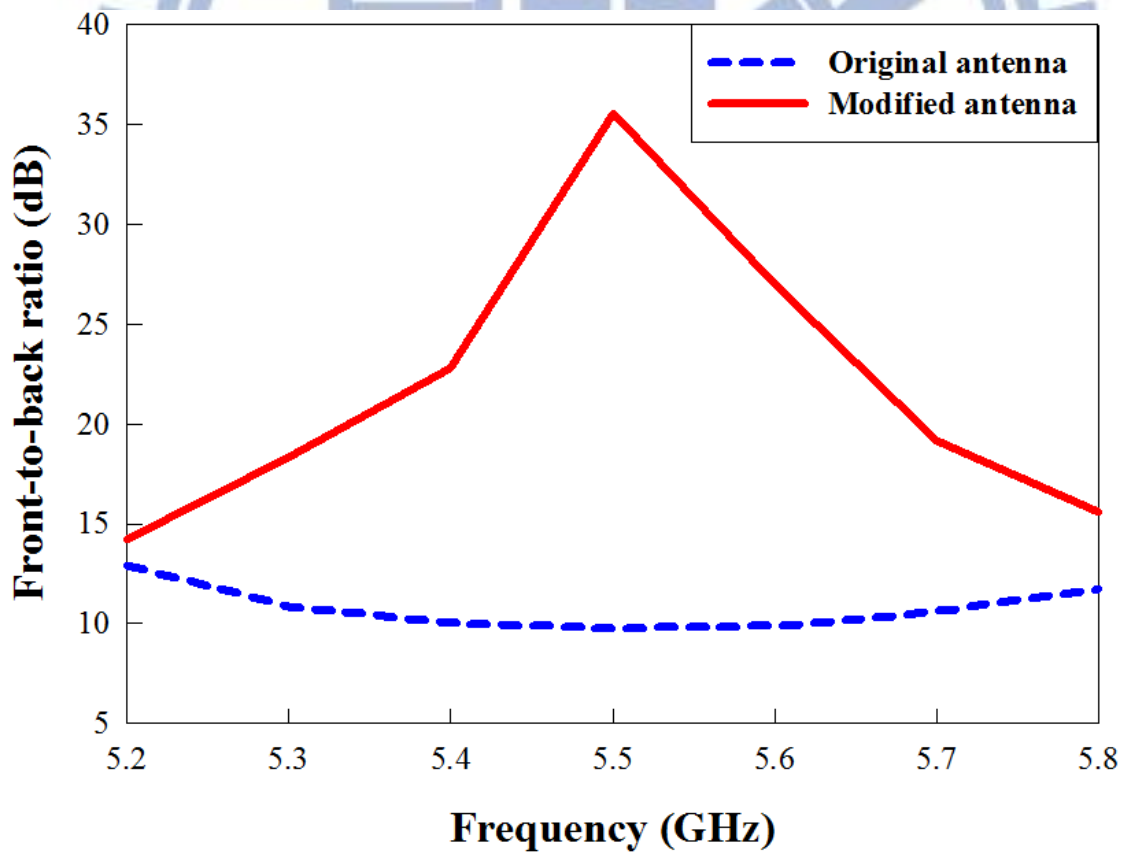


Fig. 4.19 Comparison of the simulated front-to-back ratio between the original and the modified single-conductor strip leaky-wave antenna.

#### 4.2.4 Fabrication and Measurement of Modified Single-Conductor Strip Leaky-Wave Antenna

Based on the design procedures in Sec. 4.1, 4.2.1, and 4.2.2, a modified single-conductor strip leaky-wave antenna is designed and fabricated as shown in Fig. 4.20.

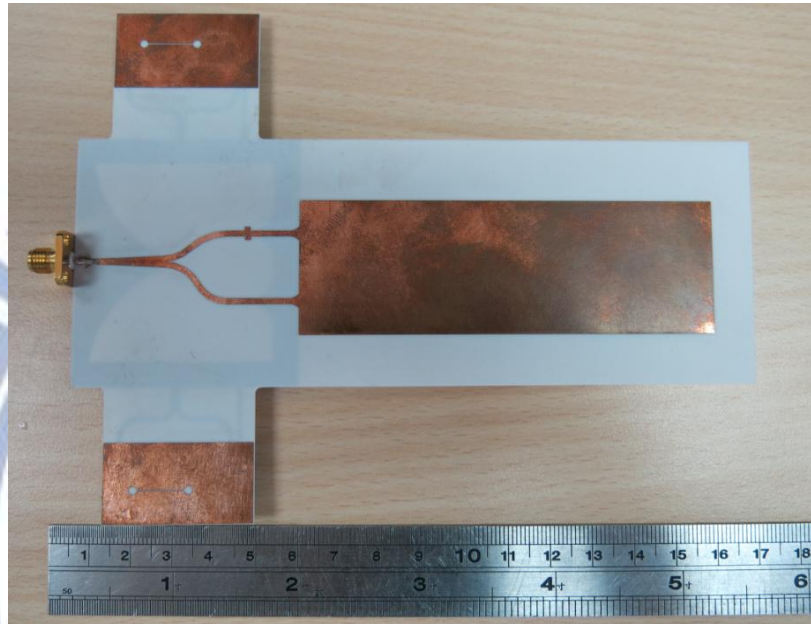


Fig. 4.20(a) Top view of the fabricated modified single-conductor strip leaky-wave antenna.

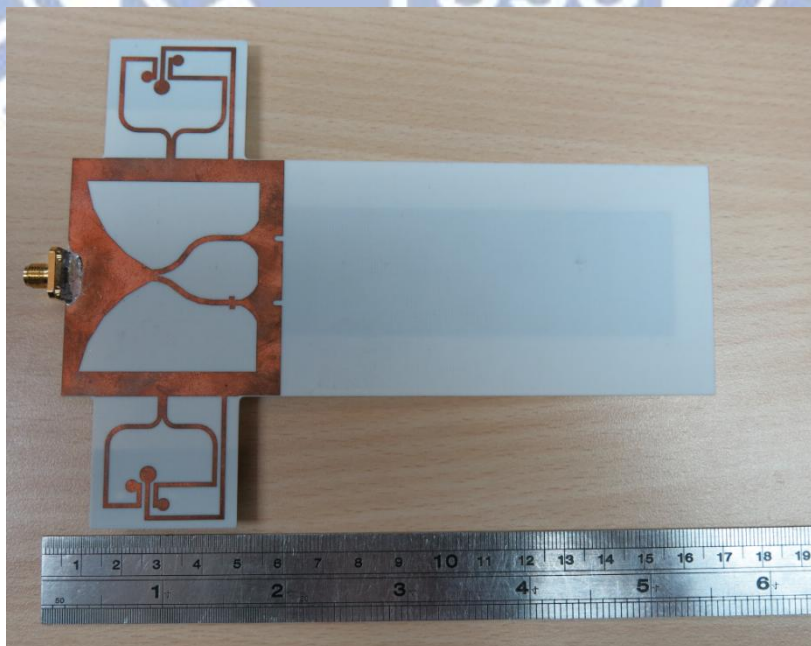


Fig. 4.20(b) Back view of the fabricated modified single-conductor strip leaky-wave antenna.

Fig. 4.21 presents the measured and simulated return loss; the measured return loss of this modified antenna is below -10 dB from 4.31 GHz to 6.85 GHz.

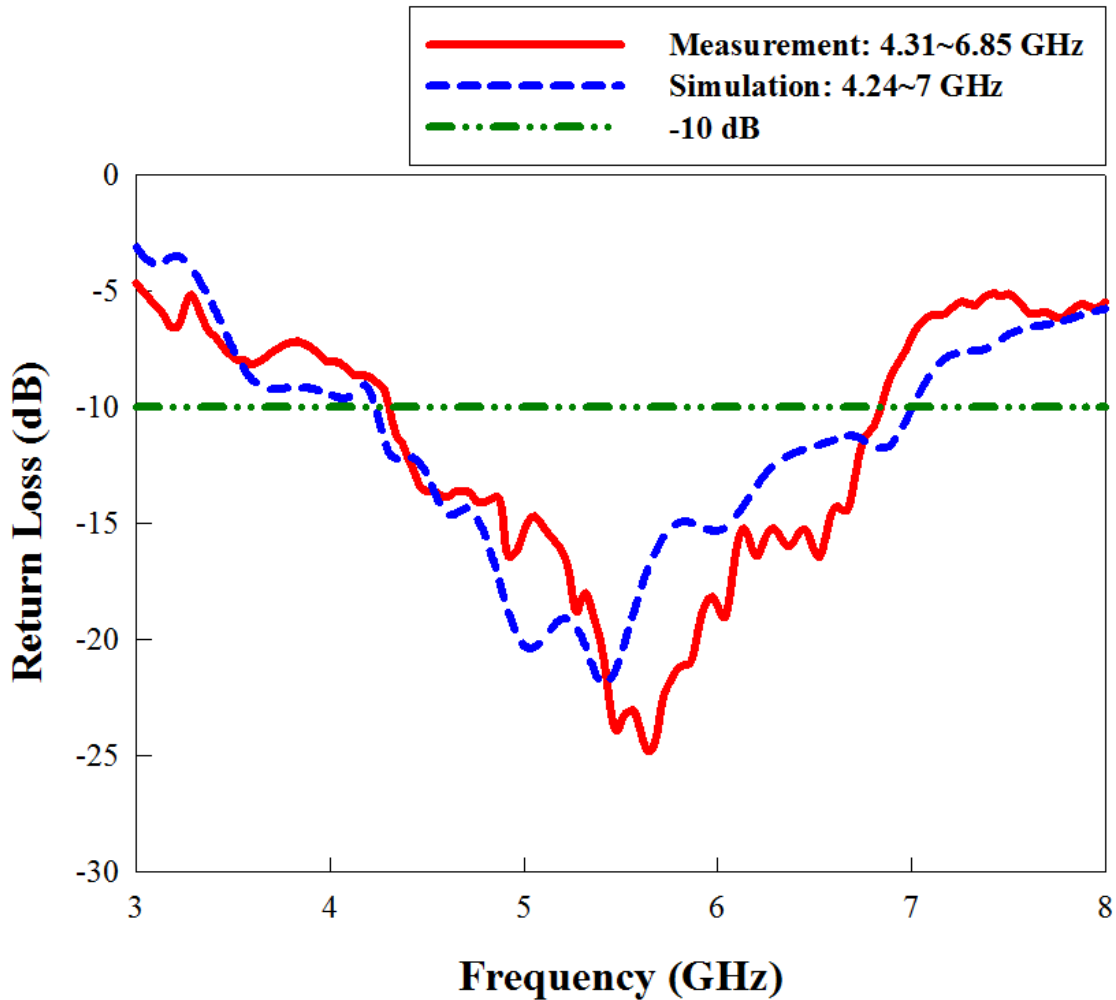


Fig. 4.21 Measured and simulated return loss of the modified single-conductor strip leaky-wave antenna.

The comparison of the measured and simulated E-plane ( $x$ - $y$  plane) radiation patterns from 5.2 GHz to 5.8 GHz is shown in Fig. 4.22(a)-(g). Table 4.3 shows the measured and simulated results, including the antenna gain and the back lobe values. Table 4.4 shows the measured and simulated results of the front-to-back ratio values, and the comparison between them are plotted in Fig. 4.23. The measured results of this modified antenna are in good agreement with the simulated results.

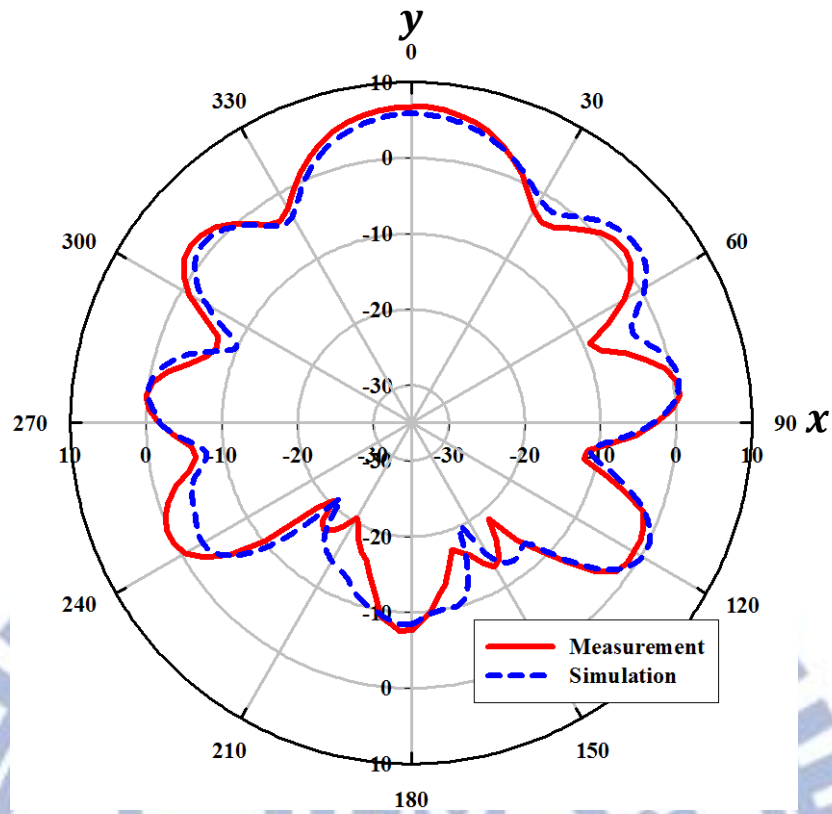


Fig. 4.22(a) Measured and simulated E-plane ( $x$ - $y$  plane) radiation patterns of the modified single-conductor strip leaky-wave antenna at 5.2 GHz.

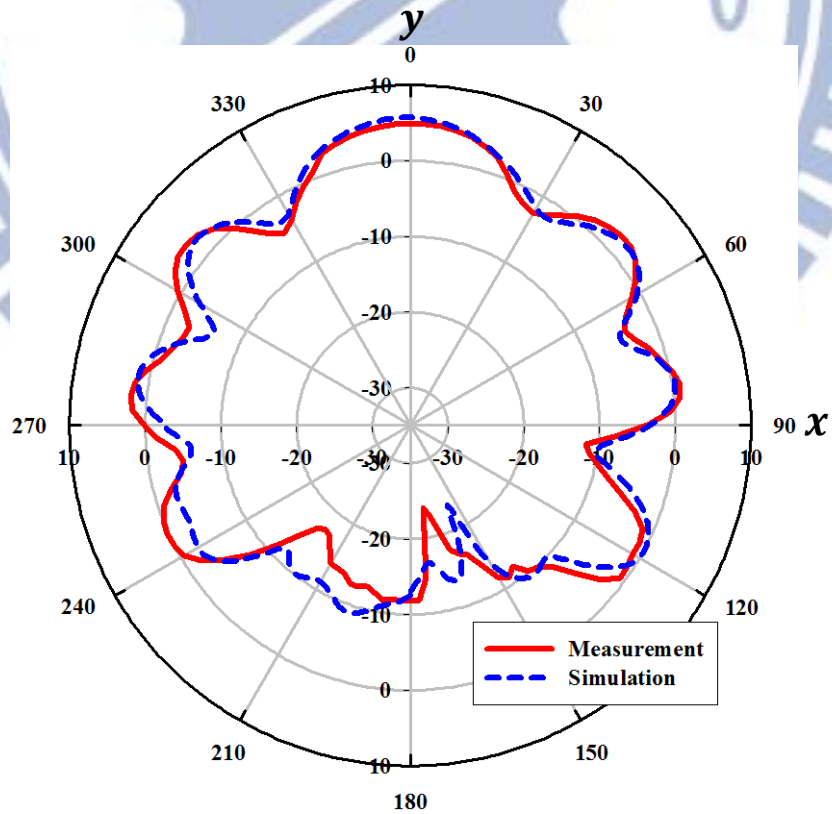


Fig. 4.22(b) Measured and simulated E-plane ( $x$ - $y$  plane) radiation patterns of the modified single-conductor strip leaky-wave antenna at 5.3 GHz.



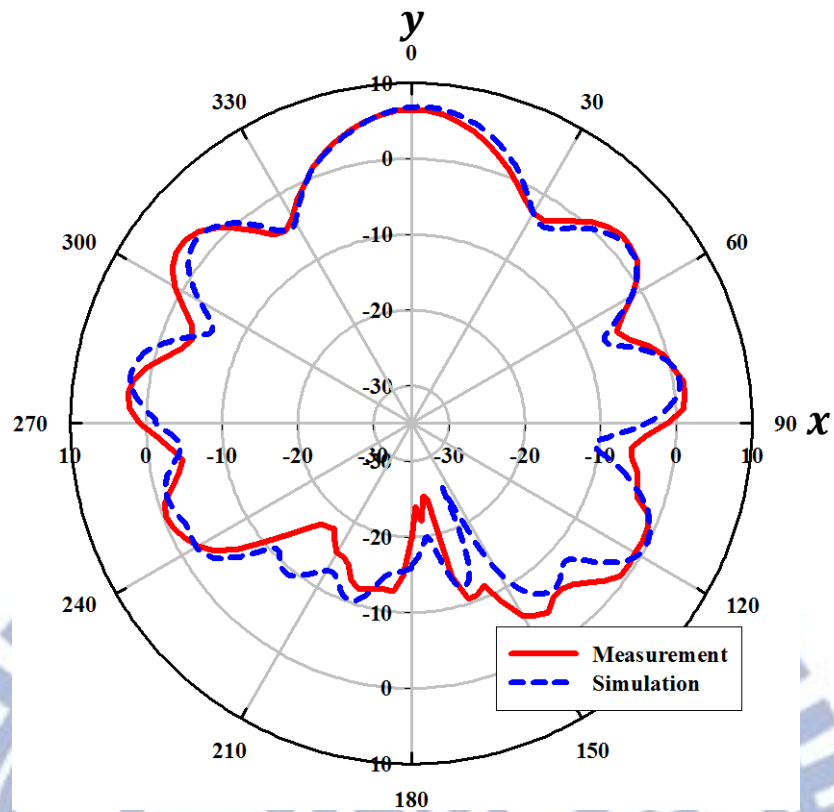


Fig. 4.22(c) Measured and simulated E-plane ( $x$ - $y$  plane) radiation patterns of the modified single-conductor strip leaky-wave antenna at 5.4 GHz.

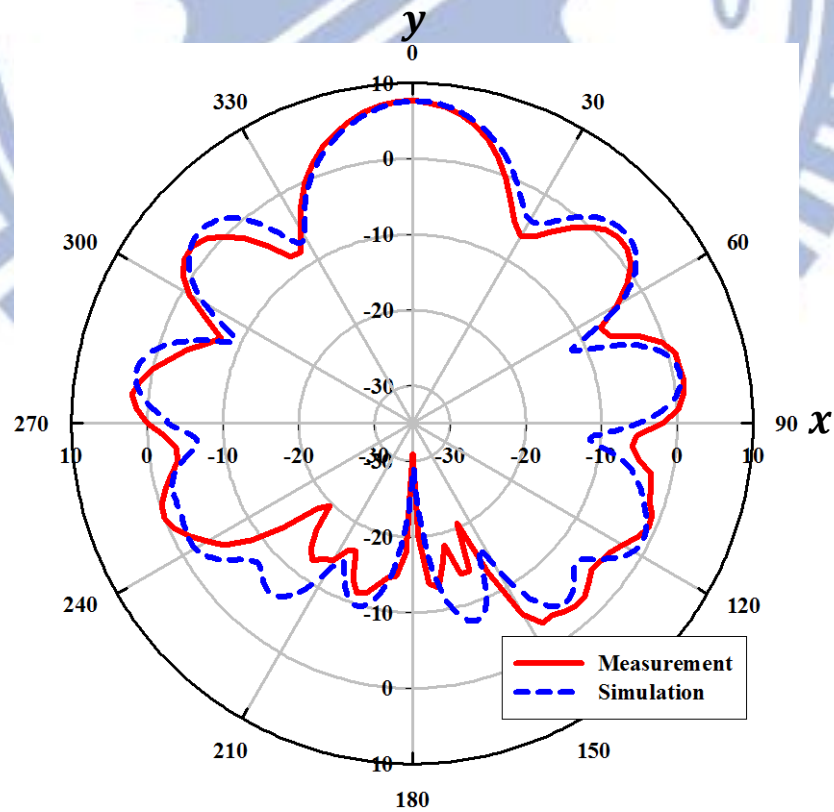


Fig. 4.22(d) Measured and simulated E-plane ( $x$ - $y$  plane) radiation patterns of the modified single-conductor strip leaky-wave antenna at 5.5 GHz.

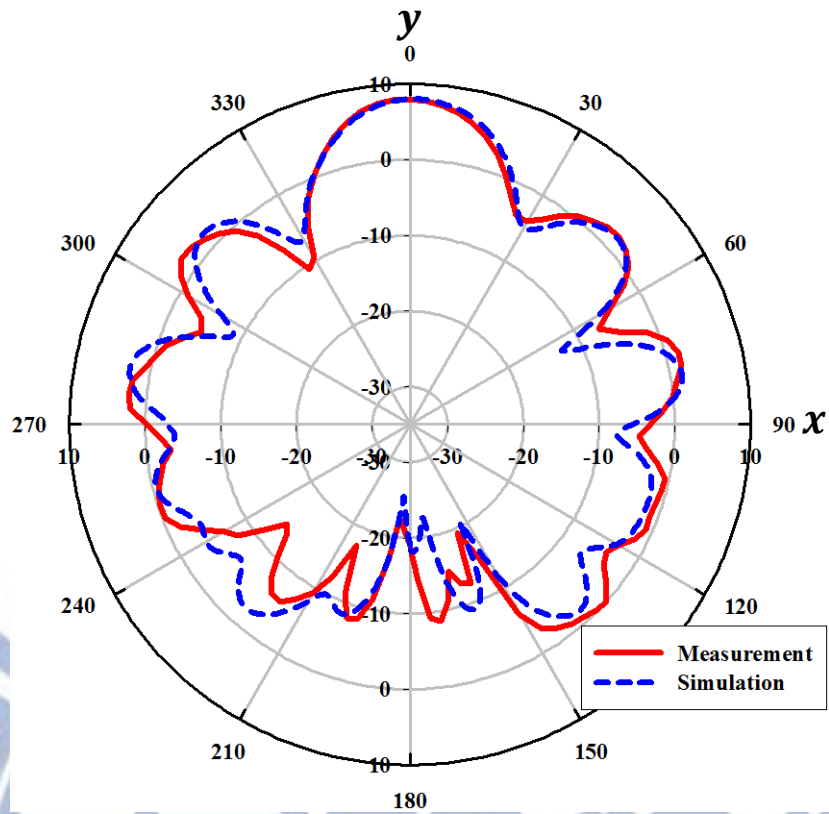


Fig. 4.22(e) Measured and simulated E-plane ( $x$ - $y$  plane) radiation patterns of the modified single-conductor strip leaky-wave antenna at 5.6 GHz.

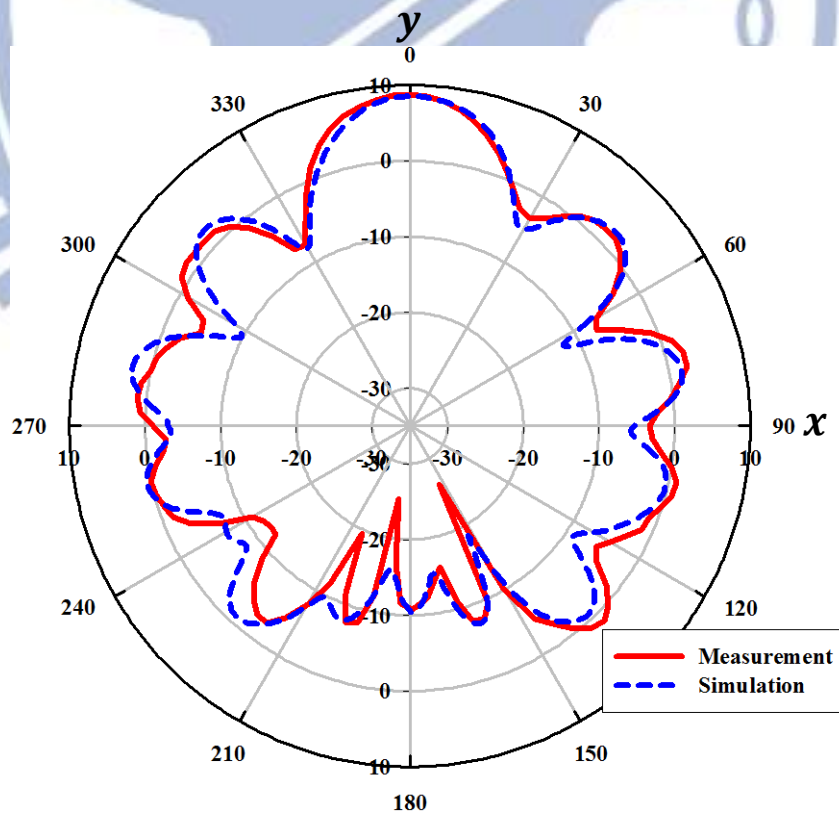


Fig. 4.22(f) Measured and simulated E-plane ( $x$ - $y$  plane) radiation patterns of the modified single-conductor strip leaky-wave antenna at 5.7 GHz.

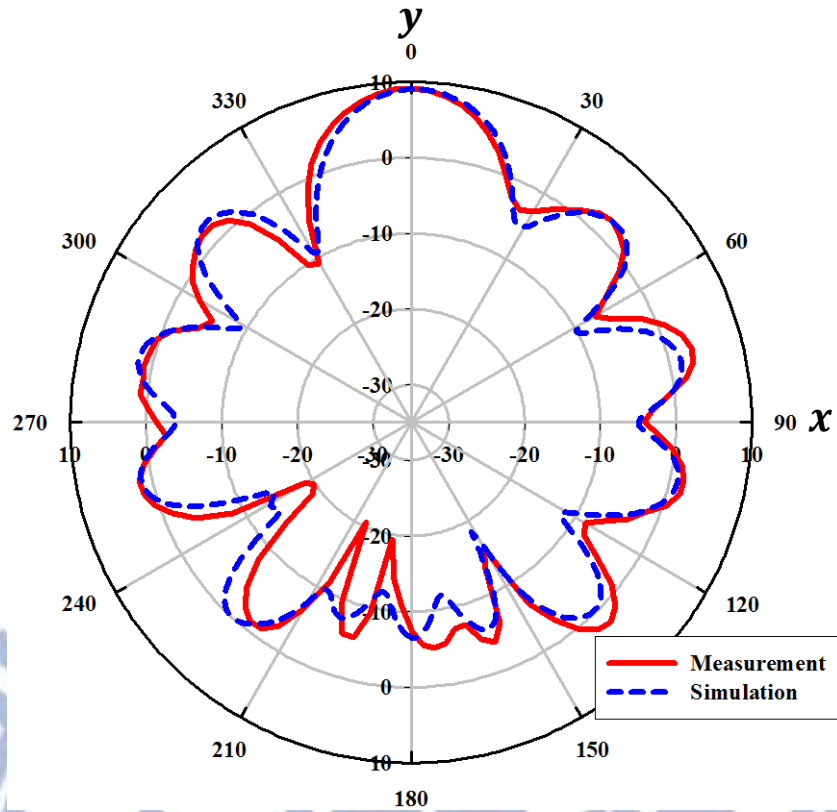


Fig. 4.22(g) Measured and simulated E-plane ( $x$ - $y$  plane) radiation patterns of the modified single-conductor strip leaky-wave antenna at 5.8 GHz.

Table 4.3 Measured and simulated results of the gain and the back lobe of the modified single-conductor strip leaky-wave antenna

Frequency (GHz)	5.2	5.3	5.4	5.5	5.6	5.7	5.8
Simulated gain (dBi)	5.86	5.67	6.85	7.6	8	8.53	9.03
Measured gain (dBi)	6.77	4.95	6.48	7.68	7.94	8.57	9.13
Simulated back lobe (dBi)	-8.38	-12.63	-15.93	-27.94	-19	-10.6	-6.54
Measured back lobe (dBi)	-7.7	-11	-19.97	-31.03	-18.86	-10.98	-7.65

Table 4.4 Measured and simulated front-to-back ratio of the modified single-conductor strip leaky-wave antenna

Frequency (GHz)	5.2	5.3	5.4	5.5	5.6	5.7	5.8
Simulated front-to-back ratio (dB)	14.24	18.3	22.78	35.54	27	19.13	15.57
Measured front-to-back ratio (dB)	14.47	15.95	26.45	38.71	26.8	19.55	16.78

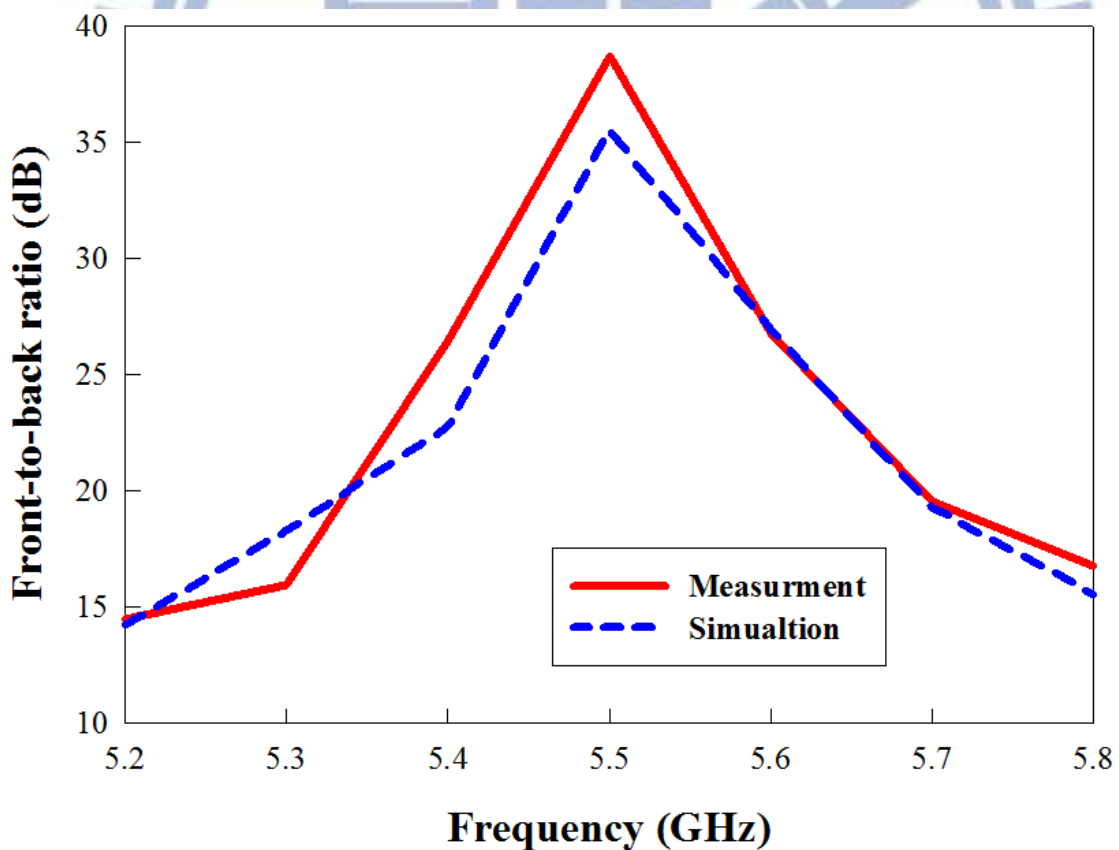


Fig. 4.23 Comparison of the measured and simulated front-to-back ratio of the modified single-conductor strip leaky-wave antenna.

# Chapter 5

## Conclusion and Future Work

### 5.1 CONCLUSION

This thesis describes the propagation characteristics of the first higher-order leaky mode of the single-conductor strip structure. Both surface wave modes  $TE_0$  and  $TM_0$  exist in the single-conductor strip structure, so the behavior of the space-wave and surface-wave modes differs from that of open transmission lines covered with ground planes, and so needs further investigation. To alleviate the large back lobe of the single-conductor strip leaky-wave antenna, the feeding structure of this antenna is modified with two broadband planar baluns. The measured results of radiation patterns reveal significant improvement of the front-to-back ratio of this antenna.

### 5.2 FUTURE WORK

In future work, there are still some topics that we can research. For the modified feeding structure of the single-conductor strip leaky-wave antenna, one challenge is how to design a wideband balun which has a smaller size. Another challenge is how to increase the bandwidth of this modified leaky-wave antenna which has the front-to-back ratio more than 20 dB.

## REFERENCES

- [1] W. Menzel, "A new traveling-wave antenna in microstrip," *Arch. Electron. Ubertrag. Tech.*, vol. 33, pp. 137–140, 1979.
- [2] A. A. Oliner and K. S. Lee, "The nature of the leakage from higher-order modes on microstrip line," in *Proc. 1986 IEEE MTT-S Int. Microwave Symp. Dig.*, Baltimore, MD, pp. 57–60, 1986.
- [3] A. A. Oliner, "Leakage from higher modes on microstrip line with application to antenna," *Radio Sci.*, vol. 22, no. 6, pp. 907–912, Nov. 1987.
- [4] J. S. Bagby, C. H. Lee, D. P. Nyquist, and Y. Yuan, "Identification of propagation regimes on integrated microstrip transmission lines," *IEEE Trans. Microwave Theory Tech.*, vol. 41, pp. 1887–1894, Nov. 1993.
- [5] J. M. Grimm and D. P. Nyquist, "Spectral analysis considerations relevant to radiation and leaky modes of open-boundary microstrip transmission line," *IEEE Trans. Microwave Theory Tech.*, vol. 41, pp. 150–153, Jan. 1993.
- [6] W. Hong and Y. D. Lin, "Single-conductor strip leaky-wave antenna," *IEEE Trans. Antennas Propag.*, vol. 52, pp. 1783–1789, July 2004.
- [7] A. A. Oliner, "Leaky waves: basic properties and applications," *Proc. Asia-Pacific Microwave Conf.*, vol. 1, pp. 397–400, 1997.
- [8] N. K. Das and D. M. Pozar, "Full-wave spectral-domain computation of material, radiation, and guided wave losses in infinite multilayered printed transmission lines," *IEEE Trans. Microwave Theory Tech.*, vol. 39, pp. 54–63, Jan. 1991.
- [9] D. R. Jackson and A. A. Oliner, *Modern Antenna Handbook*, C. A. Balanis, ed., Hoboken, NJ: John Wiley & Sons, 2008.
- [10] Y. D. Lin, J. W. Sheen, and C. K. C. Tzuang, "Analysis and design of feeding structures for microstrip leaky wave antenna," in *IEEE MTT-S Int. Microwave Symp. Dig.*,

Orlando, FL, May 1995, pp. 149–152.

- [11] Y. D. Lin and J. W. Sheen, “Mode distinction and radiation-efficiency analysis of planar leaky-wave line source,” *IEEE Trans. Microwave Theory Tech.*, vol. 45, pp. 1672–1680, Oct. 1997.
- [12] T. Itoh and R. Mittra, “Spectral-domain approach for calculating the dispersion characteristics of microstrip lines,” *IEEE Trans. Microwave theory Tech.*, vol. MTT-21, pp. 496–499, July 1973.
- [13] T. Itoh, ed., *Numerical Techniques for Microwave and Millimeter-Wave Passive Structure*. New York: Wiley, 1989, ch. 5.
- [14] R. F. Harrington, *Time-Harmonic Electromagnetic Fields*. New York: McGraw-Hill, 1961.
- [15] D. Nghiem, J. T. Williams, D. R. Jackson, and A. A. Oliner, “Existence of a leaky dominant mode on microstrip line with an isotropic substrate: theory and measurements,” *IEEE Trans. Microwave Theory Tech.*, vol. 44, pp. 1710–1715, Oct. 1996.
- [16] R. Marqués and F. Mesa, “Spectral domain analysis of higher order leaky modes in microstrip lines: A new spectral-gap effect,” *Journal of Electromagnetic Waves and Applications*, Vol. 11, No. 10, 1367–1384, 1997.
- [17] C. C. Wu, H. C. Lin, Y. D. Lin, and Toshihide Kitazawa, “Composite sector-beam single-conductor leaky-wave antenna for base-station applications,” *2012 Asia-Pacific Microwave Conference (APMC 2012)*, pp. 803–805, Kaohsiung, Taiwan, Dec. 2012.
- [18] W. H. Lian, “Printed multi-band antennas with balanced feeds and the effects of nearby conductors,” National Chiao Tung University, Hsinchu, Taiwan, 2004.
- [19] W. Hong, J. W. Sheen, T. L. Chen, Y. D. Lin, and C. Y. Chang, “Broad-band tapered microstrip leaky-wave antenna,” *IEEE Trans. Antennas Propag.*, vol. 51, pp. 1922–1928, Aug. 2003.
- [20] K. C. Gupta, R. Garg and I. J. Bahl, *Microstrip Lines and Slotlines*. Artech House, 1979.

# APPENDIX A

## Part 1:

Maxwell' equations:

$$\nabla \times \vec{E} = -j\omega\vec{B} - \vec{M}$$

$$\nabla \times \vec{H} = j\omega\vec{D} + \vec{J}$$

$$\nabla \cdot \vec{D} = \rho$$

$$\nabla \cdot \vec{B} = 0$$

$$\nabla \cdot \vec{J} = -j\omega\rho$$

$$\nabla \cdot \vec{M} = 0$$

Lorentz condition (or gauge):

$$\nabla \cdot \vec{A} = -j\omega\mu\varepsilon\phi \Rightarrow \phi = -\frac{1}{j\omega\mu\varepsilon} \nabla \cdot \vec{A}$$

$\vec{A}$ : magnetic vector potential

$\phi$ : electric scalar potential

Duality principles:

Electric sources ( $\vec{J} \neq 0, \vec{M} = 0$ )

Magnetic sources ( $\vec{J} = 0, \vec{M} \neq 0$ )

$$\vec{E}_A$$

$$\vec{H}_A$$

$$\vec{J}$$

$$\vec{A}$$

$$\varepsilon$$

$$\mu$$

$$\eta$$

$$1/\eta$$

$$\vec{H}_F$$

$$-\vec{E}_F$$

$$\vec{M}$$

$$\vec{F}$$

$$\mu$$

$$\varepsilon$$

$$1/\eta$$

$$\eta$$

1) If only  $\vec{J}$  exists

$$\vec{B} = \mu\vec{H}_A = \nabla \times \vec{A} \Rightarrow \boxed{\vec{H}_A = \frac{1}{\mu} \nabla \times \vec{A}} \quad (\because \nabla \cdot \vec{B} = 0 \equiv \nabla \cdot (\nabla \times \vec{A}))$$

$$\nabla \times \vec{E}_A = -j\omega\vec{B} = -j\omega(\nabla \times \vec{A}) \Rightarrow \nabla \times (\vec{E}_A + j\omega\vec{A}) = 0 \equiv \nabla \times (-\nabla\phi)$$

$$\Rightarrow \vec{E}_A = -\nabla\phi - j\omega\vec{A} \Rightarrow \boxed{\vec{E}_A = -\nabla\phi - j\omega\vec{A} - j\frac{1}{\omega\mu\varepsilon} \nabla(\nabla \cdot \vec{A})}$$



2) If only  $\vec{M}$  exists

$$\boxed{\vec{E}_F = -\frac{1}{\epsilon} \nabla \times \vec{F}} \quad \boxed{\vec{H}_F = -j\omega \vec{F} - j\frac{1}{\omega\mu\epsilon} (\nabla \cdot \vec{\nabla}) \vec{F}}$$

3) If  $\vec{J}$  and  $\vec{M}$  both exist

$$\boxed{\vec{E} = \vec{E}_A + \vec{E}_F = -j\omega\vec{A} - j\frac{1}{\omega\mu\epsilon} \nabla(\nabla \cdot \vec{A}) - \frac{1}{\epsilon} \nabla \times \vec{F}}$$

$$\boxed{\vec{H} = \vec{H}_A + \vec{H}_F = \frac{1}{\mu} \nabla \times \vec{A} - j\omega\vec{F} - j\frac{1}{\omega\mu\epsilon} \nabla(\nabla \cdot \vec{F})}$$

It is possible to combine the scalar and vector potentials and the Lorentz condition and form a single vector called the Hertz vector, from which all the field components can be derived. Let us define the electric Hertz vector  $\vec{\psi}$  such that

$$\boxed{\vec{A} = \mu\vec{\Psi}_e} \Rightarrow \nabla \cdot \vec{A} = \mu(\nabla \cdot \vec{\psi}_e) = -j\omega\mu\epsilon\phi \Rightarrow \boxed{\phi = -\frac{1}{j\omega\epsilon} \nabla \cdot \vec{\Psi}_e}$$

**TM<sub>y</sub> :**

$$\boxed{\vec{A} = A_y(x, y, z)\hat{a}_y = \mu\Psi_e(x, y, z)\hat{a}_y}$$

$$\boxed{\vec{F} = 0}$$

Let  $\hat{y} = j\omega\epsilon$  ,  $\hat{z} = j\omega\mu$  ,  $k^2 = \omega^2\mu\epsilon$

$$\vec{E}_A = -j\omega\vec{A} - j\frac{1}{\omega\mu\epsilon} \nabla(\nabla \cdot \vec{A}) \quad \text{and} \quad \vec{H}_A = \frac{1}{\mu} \nabla \times \vec{A}$$

$E_x = -j\frac{1}{\omega\mu\epsilon} \frac{\partial^2 A_y}{\partial x \partial y} = \frac{1}{\hat{y}} \frac{\partial^2 \Psi_e}{\partial x \partial y}$	$H_x = -\frac{1}{\mu} \frac{\partial A_y}{\partial z} = -\frac{\partial \Psi_e}{\partial z}$
$E_y = -j\frac{1}{\omega\mu\epsilon} \left( \frac{\partial^2}{\partial y^2} + k^2 \right) A_y = \frac{1}{\hat{y}} \left( \frac{\partial^2}{\partial y^2} + k^2 \right) \Psi_e$	$H_y = 0$
$E_z = -j\frac{1}{\omega\mu\epsilon} \frac{\partial^2 A_y}{\partial y \partial z} = \frac{1}{\hat{y}} \frac{\partial^2 \Psi_e}{\partial y \partial z}$	$H_z = \frac{1}{\mu} \frac{\partial A_y}{\partial x} = \frac{\partial \Psi_e}{\partial x}$

**TE<sub>y</sub> :**

$$\begin{aligned} \vec{F} &= F_y(x, y, z)\hat{a}_y = \epsilon\Psi_h(x, y, z)\hat{a}_y \\ \vec{A} &= 0 \end{aligned}$$

Let  $\hat{y} = j\omega\epsilon$  ,  $\hat{z} = j\omega\mu$  ,  $k^2 = \omega^2\mu\epsilon$

$$\vec{E}_F = -\frac{1}{\epsilon}\nabla \times \vec{F} \quad \text{and} \quad \vec{H}_F = -j\omega\vec{F} - j\frac{1}{\omega\mu\epsilon}\nabla(\nabla \cdot \vec{F})$$

$$\begin{aligned} E_x &= \frac{1}{\epsilon} \frac{\partial F_y}{\partial z} = \frac{\partial \Psi_h}{\partial z} & H_x &= -j \frac{1}{\omega\mu\epsilon} \frac{\partial^2 F_y}{\partial x \partial y} = \frac{1}{\hat{z}} \frac{\partial^2 \Psi_h}{\partial x \partial y} \\ E_y &= 0 & H_y &= -j \frac{1}{\omega\mu\epsilon} \left( \frac{\partial^2}{\partial y^2} + k^2 \right) F_y = \frac{1}{\hat{z}} \left( \frac{\partial^2}{\partial y^2} + k^2 \right) \Psi_h \\ E_z &= -\frac{1}{\epsilon} \frac{\partial F_y}{\partial x} = -\frac{\partial \Psi_h}{\partial x} & H_z &= -j \frac{1}{\omega\mu\epsilon} \frac{\partial^2 F_y}{\partial y \partial z} = \frac{1}{\hat{z}} \frac{\partial^2 \Psi_h}{\partial y \partial z} \end{aligned}$$

**TM<sub>y</sub> + TE<sub>y</sub>:**

Let  $\hat{y} = j\omega\epsilon$  ,  $\hat{z} = j\omega\mu$  ,  $k^2 = \omega^2\mu\epsilon$

$$\begin{aligned} E_x &= \frac{1}{\hat{y}} \frac{\partial^2 \Psi_e}{\partial x \partial y} + \frac{\partial \Psi_h}{\partial z} & H_x &= -\frac{\partial \Psi_e}{\partial z} + \frac{1}{\hat{z}} \frac{\partial^2 \Psi_h}{\partial x \partial y} \\ E_y &= \frac{1}{\hat{y}} \left( \frac{\partial^2}{\partial y^2} + k^2 \right) \Psi_e & H_y &= \frac{1}{\hat{z}} \left( \frac{\partial^2}{\partial y^2} + k^2 \right) \Psi_h \\ E_z &= \frac{1}{\hat{y}} \frac{\partial^2 \Psi_e}{\partial y \partial z} - \frac{\partial \Psi_h}{\partial x} & H_z &= \frac{\partial \Psi_e}{\partial x} + \frac{1}{\hat{z}} \frac{\partial^2 \Psi_h}{\partial y \partial z} \end{aligned}$$

Fourier transform pairs:

$$\begin{aligned} F(k_x) &= \int_{-\infty}^{\infty} f(x) e^{jk_x x} dx \\ f(x) &= \frac{1}{2\pi} \int_{-\infty}^{\infty} F(k_x) e^{-jk_x x} dk_x \end{aligned}$$

$$\Psi_e(x, y, z) = \psi_e(x, y) e^{-jk_z z} \xrightarrow{\text{F.T.}} \tilde{\Psi}_e(k_x, y, z) = \tilde{\psi}_e(k_x, y) e^{-jk_z z}$$

$$\frac{\partial \Psi_e}{\partial x} \xrightarrow{\text{F.T.}} -jk_x \tilde{\Psi}_e, \quad \frac{\partial \Psi_e}{\partial z} \xrightarrow{\text{F.T.}} -jk_z \tilde{\Psi}_e$$

$$\Psi_h(x, y, z) = \psi_h(x, y) e^{-jk_z z} \xrightarrow{\text{F.T.}} \tilde{\Psi}_h(k_x, y, z) = \tilde{\psi}_h(k_x, y) e^{-jk_z z}$$

$$\frac{\partial \Psi_h}{\partial x} \xrightarrow{\text{F.T.}} -jk_x \tilde{\Psi}_h, \quad \frac{\partial \Psi_h}{\partial z} \xrightarrow{\text{F.T.}} -jk_z \tilde{\Psi}_h$$

TM<sub>y</sub> + TE<sub>y</sub>  $\xrightarrow{\text{F.T. , neglect } e^{-j\beta z}}$

$$\begin{aligned}\tilde{E}_x &= -j \frac{k_x}{\hat{y}} \frac{\partial \tilde{\psi}^e}{\partial y} - j k_z \tilde{\psi}^h & \tilde{H}_x &= j k_z \tilde{\psi}^e - j \frac{k_x}{\hat{z}} \frac{\partial \tilde{\psi}^h}{\partial y} \\ \tilde{E}_y &= \frac{1}{\hat{y}} \left( \frac{\partial^2}{\partial y^2} + k^2 \right) \tilde{\psi}^e & \tilde{H}_y &= \frac{1}{\hat{z}} \left( \frac{\partial^2}{\partial y^2} + k^2 \right) \tilde{\psi}^h \\ \tilde{E}_z &= -j \frac{k_z}{\hat{y}} \frac{\partial \tilde{\psi}^e}{\partial y} + j k_x \tilde{\psi}^h & \tilde{H}_z &= -j k_x \tilde{\psi}^e - j \frac{k_z}{\hat{z}} \frac{\partial \tilde{\psi}^h}{\partial y}\end{aligned}$$

$$\hat{y} = j\omega\epsilon \quad \hat{z} = j\omega\mu \quad k^2 = \omega^2 \mu\epsilon$$

## Part 2:

$$\begin{aligned}(\nabla^2 + k^2) \begin{pmatrix} \tilde{A} \\ \tilde{F} \end{pmatrix} &= 0 \\ \Rightarrow (\nabla^2 + k^2) \begin{pmatrix} \Psi_e \\ \Psi_h \end{pmatrix} &= 0 \\ \Rightarrow \left( \frac{\partial^2}{\partial x^2} + \frac{\partial^2}{\partial y^2} + \frac{\partial^2}{\partial z^2} + k^2 \right) \begin{pmatrix} \Psi_e \\ \Psi_h \end{pmatrix} &= 0 \xrightarrow{\text{F.T. , neglect } e^{-j\beta z}} \left( -k_x^2 + \frac{\partial^2}{\partial y^2} - \beta^2 + k^2 \right) \begin{pmatrix} \tilde{\psi}_e \\ \tilde{\psi}_h \end{pmatrix} = 0 \\ \Rightarrow \left( \frac{\partial^2}{\partial y^2} - \gamma^2 \right) \begin{pmatrix} \tilde{\psi}_e \\ \tilde{\psi}_h \end{pmatrix} &= 0, \quad \gamma^2 = k_x^2 + \beta^2 - k^2\end{aligned}$$

## APPENDIX B

Apply the boundary conditions to (3-10):

$$\tilde{E}_{x1} = \tilde{E}_{x2} \quad \text{at } y=h$$

$$jk_x \gamma_{y1} A^e - jk_z A^h = -jk_x \gamma_{y2} (B^e \cosh \gamma_2 h + C^e \sinh \gamma_2 h) - jk_z (B^h \cosh \gamma_2 h + C^h \sinh \gamma_2 h) \quad (\text{B-1})$$

$$\tilde{E}_{z1} = \tilde{E}_{z2} \quad \text{at } y=h$$

$$jk_z \gamma_{y1} A^e e^{-\gamma_1} + jk_x A^h e^{-\gamma_1} = -jk_z \gamma_{y2} (B^e \cosh \gamma_2 h + C^e \sinh \gamma_2 h) + jk_x (B^h \cosh \gamma_2 h + C^h \sinh \gamma_2 h) \quad (\text{B-2})$$

$$\tilde{E}_{x2} = \tilde{E}_{x3} \quad \text{at } y=0$$

$$-jk_x \gamma_{y2} B^e - jk_z B^h = -jk_x \gamma_{y3} D^e - jk_z D^h \quad (\text{B-3})$$

$$\tilde{E}_{z2} = \tilde{E}_{z3} \quad \text{at } y=0$$

$$-jk_z \gamma_{y2} B^e + jk_x B^h = -jk_z \gamma_{y3} D^e + jk_x D^h \quad (\text{B-4})$$

$$\tilde{H}_{x2} - \tilde{H}_{x1} = \tilde{J}_z(k_x) \quad \text{at } y=h$$

$$jk_z (B^e \sinh \gamma_2 h + C^e \cosh \gamma_2 h) - jk_x \gamma_{z2} (B^h \sinh \gamma_2 h + C^h \cosh \gamma_2 h) - jk_z A^e - jk_x \gamma_{z1} A^h = \tilde{J}_z(k_x) \quad (\text{B-5})$$

$$\tilde{H}_{z2} - \tilde{H}_{z1} = -\tilde{J}_x(k_x) \quad \text{at } y=h$$

$$-jk_x (B^e \sinh \gamma_2 h + C^e \cosh \gamma_2 h) - jk_z \gamma_{z2} (B^h \sinh \gamma_2 h + C^h \cosh \gamma_2 h) + jk_x A^e - jk_z \gamma_{z1} A^h = -\tilde{J}_x(k_x) \quad (\text{B-6})$$

$$\tilde{H}_{x3} - \tilde{H}_{x2} = 0 \text{ at } y=0$$

$$jk_z D^e - jk_x \gamma_{z3} D^h = jk_z C^e - jk_x \gamma_{z2} C^h \quad (\text{B-7})$$

$$\tilde{H}_{z3} - \tilde{H}_{z2} = 0 \text{ at } y=0$$

$$-jk_x D^e - jk_z \gamma_{z3} D^h = -jk_x C^e - jk_z \gamma_{z2} C^h \quad (\text{B-8})$$

Multiply (B-1) by  $k_x$  and (B-2) by  $k_z$  and add the resulting equations; then multiply (B-1) by  $k_z$  and (B-2) by  $k_x$  and subtract the latter from the former. Similar procedures are also applied to (B-3) and (B-4). The results are

$$\gamma_{y1} A^e = -\gamma_{y2} B^e \cosh \gamma_2 h - \gamma_{y2} C^e \sinh \gamma_2 h \quad (\text{B-9})$$

$$A^h = B^h \cosh \gamma_2 h + C^h \sinh \gamma_2 h \quad (\text{B-10})$$

$$\gamma_{y2} B^e = \gamma_{y3} D^e \quad (\text{B-11})$$

$$B^h = D^h \quad (\text{B-12})$$

From (B-9)-(B-12), derive  $B^e$ ,  $B^h$ ,  $C^e$ ,  $C^h$  in terms of  $A^e$ ,  $A^h$ ,  $D^e$ ,  $D^h$ , and substitute them into Eqs. (B-5)-(B-8) to obtain

$$-jk_z [F_{12} A^e + P_{23} D^e] - jk_x [R_{12} A^h - Q_{23} D^h] = \tilde{J}_z \quad (\text{B-13})$$

$$-jk_x [F_{12} A^e + P_{23} D^e] + jk_z [R_{12} A^h - Q_{23} D^h] = \tilde{J}_x \quad (\text{B-14})$$

$$jk_z [P_{12} A^e + F_{23} D^e] - jk_x [-Q_{12} A^h + R_{23} D^h] = 0 \quad (\text{B-15})$$

$$jk_x [P_{12} A^e + F_{23} D^e] + jk_z [-Q_{12} A^h + R_{23} D^h] = 0 \quad (\text{B-16})$$

where

$$\begin{aligned}
 F_{12} &= \frac{\gamma_{y1}}{\gamma_{y2} \tanh \gamma_2 h} + 1 & F_{23} &= \frac{\gamma_{y3}}{\gamma_{y2} \tanh \gamma_2 h} + 1 \\
 R_{12} &= \frac{\gamma_{z2}}{\tanh \gamma_2 h} + \gamma_{z1} & R_{23} &= \frac{\gamma_{z2}}{\tanh \gamma_2 h} + \gamma_{z3} \\
 P_{12} &= \frac{\gamma_{y1}}{\gamma_{y2} \sinh \gamma_2 h} & P_{23} &= \frac{\gamma_{y3}}{\gamma_{y2} \sinh \gamma_2 h} \\
 Q_{12} &= Q_{23} = \frac{\gamma_{z1}}{\sinh \gamma_2 h}
 \end{aligned}$$

Multiply (B-13) by  $k_z$  and (B-14) by  $k_x$  and add the resulting equations; then multiply (B-13) by  $k_x$  and (B-14) by  $k_z$  and subtract the latter from the former. Similar procedures are also applied to (B-15) and (B-16).

$$-j(k_x^2 + k_z^2)[F_{12}A^e + P_{23}D^e] = k_z \tilde{J}_z + k_x \tilde{J}_x \quad (\text{B-17})$$

$$-j(k_x^2 + k_z^2)[R_{12}A^h - Q_{23}D^h] = k_x \tilde{J}_z - k_z \tilde{J}_x \quad (\text{B-18})$$

$$j(k_x^2 + k_z^2)[P_{12}A^e - F_{23}D^e] = 0 \quad (\text{B-19})$$

$$-j(k_x^2 + k_z^2)[-Q_{12}A^h + R_{23}D^h] = 0 \quad (\text{B-20})$$

From (B-17)-(B-20), we obtain

$$A^e = j \frac{1}{(k_x^2 + k_z^2)\Gamma_e} [F_{23}k_z \tilde{J}_z + F_{23}k_x \tilde{J}_x] \quad (\text{B-21})$$

$$A^h = j \frac{1}{(k_x^2 + k_z^2)\Gamma_h} [R_{23}k_x \tilde{J}_z - R_{23}k_z \tilde{J}_x] \quad (\text{B-22})$$

$$D^e = -j \frac{1}{(k_x^2 + k_z^2)\Gamma_e} [P_{12}k_z \tilde{J}_z + P_{12}k_x \tilde{J}_x] \quad (\text{B-23})$$

$$D^h = j \frac{1}{(k_x^2 + k_z^2)\Gamma_h} [Q_{12}k_x \tilde{J}_z - Q_{12}k_z \tilde{J}_x] \quad (\text{B-24})$$

Where

$$\Gamma_e = F_{12}F_{23} - P_{12}P_{23} \quad \Gamma_h = R_{12}R_{23} - Q_{12}Q_{23}$$

Substitute equations (B-21)-(B-24) into the next equations extracted from (3-10)

$$\begin{aligned}\tilde{E}_{z1} &= \tilde{E}_z(k_x, y=h) = jk_z\gamma_{y1}A^e + jk_xA^h \\ &= -\frac{1}{(k_x^2+k_z^2)}\left[\frac{k_z^2\gamma_{y1}F_{23}}{\Gamma_e} + \frac{k_x^2R_{23}}{\Gamma_h}\right]\tilde{J}_z - \frac{1}{(k_x^2+k_z^2)}\left[\frac{k_xk_z\gamma_{y1}F_{23}}{\Gamma_e} - \frac{k_xk_zR_{23}}{\Gamma_h}\right]\tilde{J}_x\end{aligned}\quad (\text{B - 2 5})$$

$$\begin{aligned}\tilde{E}_{x1} &= \tilde{E}_x(k_x, y=h) = jk_x\gamma_{y1}A^e - jk_zA^h \\ &= -\frac{1}{(k_x^2+k_z^2)}\left[\frac{k_xk_z\gamma_{y1}F_{23}}{\Gamma_e} - \frac{k_xk_zR_{23}}{\Gamma_h}\right]\tilde{J}_z - \frac{1}{(k_x^2+k_z^2)}\left[\frac{k_x^2\gamma_{y1}F_{23}}{\Gamma_e} + \frac{k_z^2R_{23}}{\Gamma_h}\right]\tilde{J}_x\end{aligned}\quad (\text{B - 2 6})$$

When this process is completed, we obtain the relationship between the Fourier transforms of the electric fields and those of the current distributions:

$$\begin{bmatrix} \tilde{E}_{z1} \\ \tilde{E}_{x1} \end{bmatrix} = \begin{bmatrix} -\frac{1}{(k_x^2+k_z^2)}\left(\frac{k_z^2\gamma_{y1}F_{23}}{\Gamma_e} + \frac{k_x^2R_{23}}{\Gamma_h}\right) & -\frac{1}{(k_x^2+k_z^2)}\left(\frac{k_xk_z\gamma_{y1}F_{23}}{\Gamma_e} - \frac{k_xk_zR_{23}}{\Gamma_h}\right) \\ -\frac{1}{(k_x^2+k_z^2)}\left(\frac{k_xk_z\gamma_{y1}F_{23}}{\Gamma_e} - \frac{k_xk_zR_{23}}{\Gamma_h}\right) & -\frac{1}{(k_x^2+k_z^2)}\left(\frac{k_x^2\gamma_{y1}F_{23}}{\Gamma_e} + \frac{k_z^2R_{23}}{\Gamma_h}\right) \end{bmatrix} \cdot \begin{bmatrix} \tilde{J}_z \\ \tilde{J}_x \end{bmatrix} \quad (\text{B-27})$$

Substituting  $F_{23}$ ,  $R_{23}$ ,  $\Gamma_e$  and  $\Gamma_h$  into (B-27), then we obtain (3-13).

## APPENDIX C

$$\int_{-a}^a \frac{1}{\sqrt{a^2 - x^2}} e^{j\alpha x} dx = \pi J_0(a|\alpha|), \quad J_0: \text{zeroth-order Bessel function of the first kind}$$

$$J_{xm}(x) = \frac{\cos[(2m-1)\pi x/w]}{\sqrt{1-(2x/w)^2}}, \quad m=1, 2, \dots, M \quad \text{and} \quad |x| < w/2$$

$$\begin{aligned} \tilde{J}_{xm}(k_x) &= \int_{-\infty}^{\infty} J_{xm}(x) e^{jk_x x} dx \\ &= \int_{-\frac{w}{2}}^{\frac{w}{2}} \frac{\cos[(2m-1)\pi x/w]}{\sqrt{1-(2x/w)^2}} e^{jk_x x} dx \\ &= \int_{-\frac{w}{2}}^{\frac{w}{2}} \frac{\cos[(2m-1)\pi x/w]}{\sqrt{1-(2x/w)^2}} \cos(k_x x) dx + j \int_{-\frac{w}{2}}^{\frac{w}{2}} \frac{\cos[(2m-1)\pi x/w]}{\sqrt{1-(2x/w)^2}} \sin(k_x x) dx \\ &= \frac{1}{2} \int_{-\frac{w}{2}}^{\frac{w}{2}} \frac{\cos\left[\frac{k_x w + (2m-1)\pi}{w} x\right]}{\sqrt{1-(2x/w)^2}} dx + \frac{1}{2} \int_{-\frac{w}{2}}^{\frac{w}{2}} \frac{\cos\left[\frac{k_x w - (2m-1)\pi}{w} x\right]}{\sqrt{1-(2x/w)^2}} dx \\ &= j \frac{1}{2} \int_{-\frac{w}{2}}^{\frac{w}{2}} \frac{\sin\left[\frac{k_x w + (2m-1)\pi}{w} x\right]}{\sqrt{1-(2x/w)^2}} dx + j \frac{1}{2} \int_{-\frac{w}{2}}^{\frac{w}{2}} \frac{\sin\left[\frac{k_x w - (2m-1)\pi}{w} x\right]}{\sqrt{1-(2x/w)^2}} dx \\ &= \frac{1}{2} \int_{-\frac{w}{2}}^{\frac{w}{2}} \frac{e^{j\left[\frac{k_x w + (2m-1)\pi}{w} x\right]}}{\sqrt{1-(2x/w)^2}} dx + \frac{1}{2} \int_{-\frac{w}{2}}^{\frac{w}{2}} \frac{e^{j\left[\frac{k_x w - (2m-1)\pi}{w} x\right]}}{\sqrt{1-(2x/w)^2}} dx \\ &= \frac{1}{2} \int_{-1}^1 \frac{e^{j\left[\frac{k_x w + (2m-1)\pi}{2} t\right]}}{\sqrt{1-t^2}} \frac{w}{2} dt + \frac{1}{2} \int_{-1}^1 \frac{e^{j\left[\frac{k_x w - (2m-1)\pi}{2} t\right]}}{\sqrt{1-t^2}} \frac{w}{2} dt \\ &= \frac{\pi w}{4} \left[ J_0\left(\left|\frac{wk_x + (2m-1)\pi}{2}\right|\right) + J_0\left(\left|\frac{wk_x - (2m-1)\pi}{2}\right|\right) \right] \end{aligned}$$

The other basis functions can be obtained by similar procedure.



## APPENDIX D

First, we will assume that the waves propagate along a uniform guiding structure in the +z direction with a propagation constant  $\gamma = \alpha + j\beta$ . For harmonic time dependence with an angular frequency  $\omega$ , the dependence on  $z$  and  $t$  for all field components can be described by the exponential factor  $e^{-\gamma z} e^{j\omega t} = e^{(j\omega t - \gamma z)} = e^{-\alpha z} e^{j(\omega t - \beta z)}$ . Using a phasor representation in equations relating field quantities we may replace partial derivatives with respect to  $t$  and  $z$  simply by products with  $j\omega$  and  $-\gamma$ , respectively; the common factor  $e^{(j\omega t - \gamma z)}$  can be omitted. Then, let us examine the interrelationships among the six components in Cartesian coordinates by expanding the two source-free ( $\vec{J} = 0, \vec{M} = 0$ ) curl equations.

From $\nabla \times \vec{E} = -j\omega\mu\vec{H}$ $\frac{\partial E_z}{\partial y} + \gamma E_y = -j\omega\mu H_x \quad (\text{D-1a})$	From $\nabla \times \vec{H} = j\omega\varepsilon\vec{E}$ $\frac{\partial H_z}{\partial y} + \gamma H_y = j\omega\varepsilon E_x \quad (\text{D-2a})$
$-\gamma E_x - \frac{\partial E_z}{\partial x} = -j\omega\mu H_y \quad (\text{D-1b})$	$-\gamma H_x - \frac{\partial H_z}{\partial x} = j\omega\varepsilon E_y \quad (\text{D-2b})$
$\frac{\partial E_y}{\partial x} - \frac{\partial E_x}{\partial y} = -j\omega\mu H_z \quad (\text{D-1c})$	$\frac{\partial H_y}{\partial x} - \frac{\partial H_x}{\partial y} = j\omega\varepsilon E_z \quad (\text{D-2c})$

Note that partial derivatives with respect to  $z$  have been replaced by multiplications by  $(-\gamma)$ . All the component field quantities in the equations above are phasors that depend only on  $x$  and  $y$ , the common  $e^{-\gamma z}$  factor for  $z$ -dependence having been omitted. By manipulating these equations we can express the transverse field components  $H_x, H_y, E_x,$  and  $E_y$  in terms of the two longitudinal components  $E_z$  and  $H_z$ .

Then we have

$$H_x = \frac{1}{k_c^2} \left( j\omega\varepsilon \frac{\partial E_z}{\partial y} - \gamma \frac{\partial H_z}{\partial x} \right) \quad (\text{D-3})$$

$$H_y = \frac{1}{k_c^2} \left( -j\omega\varepsilon \frac{\partial E_z}{\partial x} - \gamma \frac{\partial H_z}{\partial y} \right) \quad (\text{D-4})$$

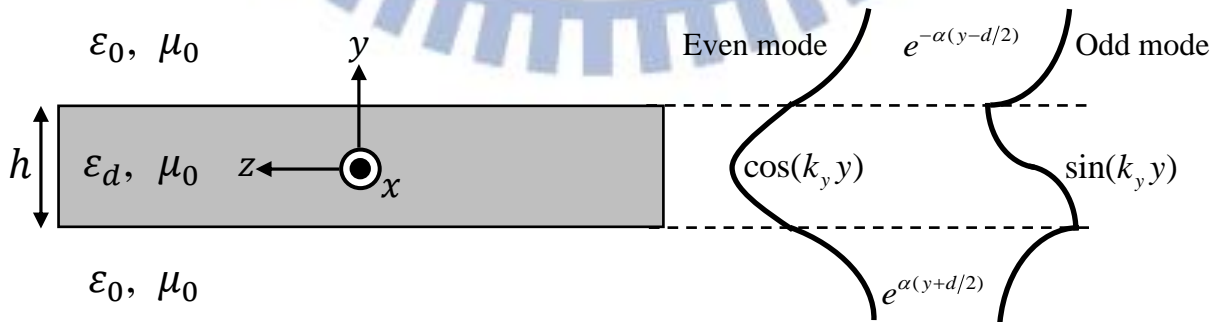
$$E_x = \frac{1}{k_c^2} \left( -\gamma \frac{\partial E_z}{\partial x} - j\omega\mu \frac{\partial H_z}{\partial y} \right) \quad (\text{D-5})$$

$$E_y = \frac{1}{k_c^2} \left( -\gamma \frac{\partial E_z}{\partial y} + j\omega\mu \frac{\partial H_z}{\partial x} \right) \quad (\text{D-6})$$

where

$$k_c^2 = k^2 + \gamma^2 \quad (\text{D-7})$$

Typically the cross section of the dielectric slab waveguide would be rectangular with height  $h$ . To simplify the analysis of this structure, we reduce the problem to a two-dimensional one (its length in the  $x$ -direction is infinite) so that  $\partial/\partial x = 0$ . We also assume that the dielectric is lossless and that waves propagate in the  $+z$ -direction, and the structure is infinite in that direction. Let  $\varepsilon_d = \varepsilon_r \varepsilon_0$  and  $\mu_0$  be the permittivity and permeability, respectively, of the dielectric slab, which is situated in free space  $(\varepsilon_0, \mu_0)$ . The behavior of TM and TE modes will now be analyzed separately.



**Transverse Magnetic (TM<sub>z</sub>) Modes:**  $H_z = 0, H_x(y, z), E_y(y, z), E_z(y, z)$

The TM<sub>z</sub> mode fields that can exist within and outside the dielectric slab. Inside and outside the dielectric region, the fields can be represented by a combination of even and odd modes as shown in the figure above. For transverse magnetic waves,  $H_z = 0$ . Since there is no  $x$ -dependence, we write the phasor  $E_z(y, z)$  as  $E_z(y)e^{-\gamma z}$ . Therefore, we have a second-order differential equation as follows:

$$\frac{d^2 E_z(y)}{dy^2} + \left\{ \begin{matrix} k_y^2 \\ k_{y0}^2 \end{matrix} \right\} E_z(y) = 0 \quad (\text{D-8})$$

where

$$k_y^2 = \gamma^2 + \omega^2 \mu_0 \epsilon_d, \quad k_{y0}^2 = \gamma^2 + \omega^2 \mu_0 \epsilon_0 \quad (\text{D-9})$$

Solutions of Eq. (D-1) must be considered in both the slab and the free-space regions, and they must be matched at the boundaries.

In the slab region we assume that the waves propagate in the  $+z$ -direction without attenuation (lossless dielectric); that is, we assume

$$\gamma = j\beta \quad (\text{D-10})$$

The solution of Eq. (D-1) in the dielectric slab may contain both a sine term and a cosine term, which are an odd and an even function, respectively, of  $y$ :

$$E_z(y) = E_o \sin k_y y + E_e \cos k_y y, \quad |y| \leq \frac{h}{2} \quad (\text{D-11})$$

where

$$k_y^2 = \omega^2 \mu_0 \epsilon_d - \beta^2 \quad (\text{D-12})$$

In the free-space regions ( $y > h/2$  and  $y < -h/2$ ) the waves must decay exponentially so that they are guided along the slab and do not radiate away from it. We have

$$E_z(y) = \begin{cases} C_u e^{-\alpha(y-h/2)}, & y \geq \frac{h}{2} \\ C_l e^{\alpha(y+h/2)}, & y \leq -\frac{h}{2} \end{cases} \quad (\text{D-13a})$$

$$(\text{D-13b})$$

where

$$\alpha^2 = \beta^2 - \omega^2 \mu_0 \epsilon_0 = -k_{y0}^2 \quad (\text{D-14})$$

Equations (D-5) and (D-7) are called dispersion relations because they show the nonlinear dependence of the phase constant  $\beta$  on  $\omega$ .

At this stage we have not yet determined the values of  $k_y$  and  $\alpha$ ; nor have we found the relationships among the amplitudes  $E_o$ ,  $E_e$ ,  $C_u$  and  $C_l$ . In the following, we will consider the odd and even TM modes separately.

**a) Odd TM modes:**

For odd TM modes,  $E_z(y)$  is described by a sine function that is antisymmetric with respect to the  $y=0$  plane. The only other field components,  $E_y(y)$  and  $H_x(y)$ , are obtained from Eqs. (D-3) and (D-6), respectively.

i) In the dielectric region,  $|y| \leq h/2$ :

$$E_z(y) = E_o \sin k_y y \quad (\text{D-15})$$

$$E_y(y) = \frac{-j\beta}{k_y} E_o \cos k_y y \quad (\text{D-16})$$

$$H_x(y) = \frac{j\omega\epsilon_d}{k_y} E_o \cos k_y y \quad (\text{D-17})$$

ii) In the upper free-space region,  $y \geq h/2$ :

$$E_z(y) = \left( E_o \sin \frac{k_y h}{2} \right) e^{-\alpha(y-h/2)} \quad (\text{D-18})$$

$$E_y(y) = -\frac{j\beta}{\alpha} \left( E_o \sin \frac{k_y h}{2} \right) e^{-\alpha(y-h/2)} \quad (\text{D-19})$$

$$H_x(y) = \frac{j\omega\epsilon_0}{\alpha} \left( E_o \sin \frac{k_y h}{2} \right) e^{-\alpha(y-h/2)} \quad (\text{D-20})$$

Where  $C_u$  in Eq. (D-13a) has been set to equal  $E_o \sin \frac{k_y h}{2}$ , which is the value of  $E_z(y)$

in Eq. (D-15) at the upper interface,  $y = h/2$ .

iii) In the lower free-space region,  $y \leq -h/2$ :

$$E_z(y) = - \left( E_o \sin \frac{k_y h}{2} \right) e^{\alpha(y+h/2)} \quad (D-21)$$

$$E_y(y) = - \frac{j\beta}{\alpha} \left( E_o \sin \frac{k_y h}{2} \right) e^{\alpha(y+h/2)} \quad (D-22)$$

$$H_x(y) = \frac{j\omega\epsilon_0}{\alpha} \left( E_o \sin \frac{k_y h}{2} \right) e^{\alpha(y+h/2)} \quad (D-22)$$

Where  $C_1$  in Eq. (D-13b) has been set to equal  $-E_o \sin \frac{k_y h}{2}$ , which is the value of  $E_z(y)$  in Eq. (D-15) at the lower interface,  $y = -h/2$ .

Now we must determine  $k_y$  and  $\alpha$  for a given angular frequency of excitation  $\omega$ .

The continuity of  $H_x$  at the dielectric surface requires that  $H_x(h/2)$  computed from Eqs. (D-17) and (D-20) be the same. We have

$$\frac{\alpha}{k_y} = \frac{jk_{y0}}{k_y} = \frac{1}{\epsilon_r} \tan \frac{k_y h}{2} \quad (\text{Odd TM modes}) \quad (D-23)$$

#### b) Even TM modes:

For even TM modes,  $E_z(y)$  is described by a cosine function that is symmetric with respect to the  $y=0$  plane:

$$E_z(y) = E_o \cos k_y |y|, \quad |y| \leq \frac{h}{2} \quad (D-24)$$

The other nonzero field components,  $E_y$  and  $H_x$ , both inside and outside the dielectric slab can be obtained in exactly the same manner as in the case of odd TM modes. Instead of Eq. (D-23), the characteristic relation between  $k_y$  and  $\alpha$  now becomes

$$\frac{\alpha}{k_y} = \frac{jk_{y0}}{k_y} = - \frac{1}{\epsilon_r} \cot \frac{k_y h}{2} \quad (\text{Even TM modes}) \quad (D-25)$$

From Eqs. (D-12) and (D-14) it is easy to see that the phase constant,  $\beta$ , of propagating TM waves lies between the intrinsic phase constant of the free space,  $k_0 = \omega\sqrt{\mu_0\epsilon_0}$ , and that of the dielectric,  $k_d = \omega\sqrt{\mu_0\epsilon_d}$ ; that is,

$$\omega\sqrt{\mu_0\epsilon_0} < \beta < \omega\sqrt{\mu_0\epsilon_d}$$

As  $\beta$  approaches the value of  $\omega\sqrt{\mu_0\epsilon_0}$ , Eq. (D-14) indicates that  $\alpha$  approaches zero. An absence of attenuation means that the waves are no longer bound to the slab. The limiting frequencies under this condition ( $\beta = \omega\sqrt{\mu_0\epsilon_0}$ ) are called **cutoff frequencies** of the dielectric waveguide. From Eq. (D-12) we have  $k_y = \omega_c\sqrt{\mu_0\epsilon_d - \mu_0\epsilon_0}$  at cutoff. Substitution into Eqs. (D-23) and (D-25) with  $\alpha$  set to zero yields the following relations for TM modes.

At cutoff:

Odd TM Modes	Even TM Modes
$\tan\left(\frac{\omega_{co}h}{2}\sqrt{\mu_0\epsilon_d - \mu_0\epsilon_0}\right) = 0$	$\cot\left(\frac{\omega_{ce}h}{2}\sqrt{\mu_0\epsilon_d - \mu_0\epsilon_0}\right) = 0$
$2\pi f_{co}h\sqrt{\mu_0\epsilon_d - \mu_0\epsilon_0} = n\pi, \quad n = 0, 2, 4, \dots$	$2\pi f_{ce}h\sqrt{\mu_0\epsilon_d - \mu_0\epsilon_0} = n\pi, \quad n = 1, 3, 5, \dots$
$f_{co} = \frac{nc}{2h\sqrt{\epsilon_r - 1}}, \quad n = 0, 2, 4, \dots \quad (D-26)$	$f_{ce} = \frac{nc}{2h\sqrt{\epsilon_r - 1}}, \quad n = 1, 3, 5, \dots \quad (D-27)$
where $c = 3 \times 10^8 \text{ m/s}$	where $c = 3 \times 10^8 \text{ m/s}$

It is seen that  $f_{co} = 0$  for  $n = 0$ . This means that **the lowest-order odd TM mode (TM<sub>0</sub>)** can propagate along a dielectric-slab waveguide regardless of the thickness of the slab. As the frequency of a given TM wave increases beyond the corresponding cutoff frequency,  $\alpha$  increases and the wave clings more tightly to the slab.

**Transverse Electric (TE<sub>z</sub>) Modes:**  $E_z = 0, E_x(y, z), H_y(y, z), H_z(y, z)$

For transverse electric waves,  $E_z = 0$ . Since there is no  $x$ -dependence, we write the phasor  $H_z(y, z)$  as  $H_z(y)e^{-\gamma z}$ . Therefore, we have a second-order differential equation as follows:

$$\frac{d^2 H_z(y)}{dy^2} + \left\{ \begin{matrix} k_y^2 \\ k_{y0}^2 \end{matrix} \right\} H_z(y) = 0 \quad (\text{D-28})$$

where  $k_y^2$  and  $k_{y0}^2$  are the same as that given in Eq. (D-9). The solution for  $H_z(y)$  may also contain both a sine term and a cosine term:

$$H_z(y) = H_o \sin k_y y + H_e \cos k_y y, \quad |y| \leq \frac{h}{2} \quad (\text{D-29})$$

where  $k_y$  has been defined in Eq. (D-12). In the free-space regions ( $y > h/2$  and  $y < -h/2$ ) the waves must decay exponentially. We write

$$H_z(y) = \begin{cases} C_u e^{-\alpha(y-h/2)}, & y \geq \frac{h}{2} \\ C_l e^{\alpha(y+h/2)}, & y \leq -\frac{h}{2} \end{cases} \quad (\text{D-30a})$$

$$(\text{D-30b})$$

where  $\alpha$  is defined in Eq. (D-14). Following the same procedure as used for TM waves, we consider the odd and even TE modes separately. Besides  $H_z(y)$ , the only other field components are  $H_y(y)$  and  $E_x(y)$ , which can be obtained from Eqs. (D-4) and (D-5).

**a) Odd TE modes:**

i) In the dielectric region,  $|y| \leq h/2$ :

$$H_z(y) = H_o \sin k_y y \quad (\text{D-31})$$

$$H_y(y) = \frac{-j\beta}{k_y} H_o \cos k_y y \quad (\text{D-32})$$

$$E_x(y) = -\frac{j\omega\mu_d}{k_y} H_o \cos k_y y \quad (\text{D-33})$$

ii) In the upper free-space region,  $y \geq h/2$ :

$$H_z(y) = \left( H_o \sin \frac{k_y h}{2} \right) e^{-\alpha(y-h/2)} \quad (\text{D-34})$$

$$H_y(y) = -\frac{j\beta}{\alpha} \left( H_o \sin \frac{k_y h}{2} \right) e^{-\alpha(y-h/2)} \quad (\text{D-35})$$

$$E_x(y) = -\frac{j\omega\mu_0}{\alpha} \left( H_o \sin \frac{k_y h}{2} \right) e^{-\alpha(y-h/2)} \quad (\text{D-36})$$

iii) In the lower free-space region,  $y \leq -h/2$ :

$$H_z(y) = -\left( H_o \sin \frac{k_y h}{2} \right) e^{\alpha(y+h/2)} \quad (\text{D-37})$$

$$H_y(y) = -\frac{j\beta}{\alpha} \left( H_o \sin \frac{k_y h}{2} \right) e^{\alpha(y+h/2)} \quad (\text{D-38})$$

$$E_x(y) = -\frac{j\omega\mu_0}{\alpha} \left( H_o \sin \frac{k_y h}{2} \right) e^{\alpha(y+h/2)} \quad (\text{D-39})$$

A relation between  $k_y$  and  $\alpha$  can be obtained by equating  $E_x(y)$ , given in Eqs. (D-33) and (D-36), at  $y = h/2$ . Thus,

$$\frac{\alpha}{k_y} = \frac{jk_{y0}}{k_y} = \tan \frac{k_y h}{2} \quad (\text{O d d T E m o d e}) \quad (\text{D-40})$$

which is seen to be closely analogous to the characteristic equation, Eq. (D-23), for odd TM modes.

#### b) Even TE modes:

For even TE modes,  $H_z(y)$  is described by a cosine function that is symmetric with respect to the  $y = 0$  plane.

$$H_z(y) = H_e \cos k_y y, \quad |y| \leq \frac{h}{2} \quad (\text{D-41})$$

The other nonzero field components,  $H_y(y)$  and  $E_x(y)$  both inside and outside the



dielectric slab can be obtained in the same manner as for odd TE modes. The characteristic relation between  $k_y$  and  $\alpha$  is closely analogous to that for even TM modes as given in Eq.

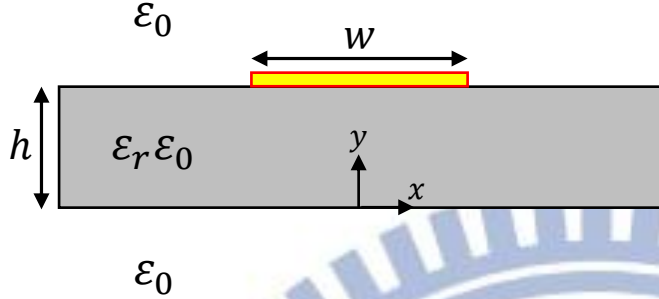
(D-25):

$$\frac{\alpha}{k_y} = \frac{jk_{y0}}{k_y} = -\cot \frac{k_y h}{2} \quad (\text{Even TE mode}) \quad (\text{D-42})$$

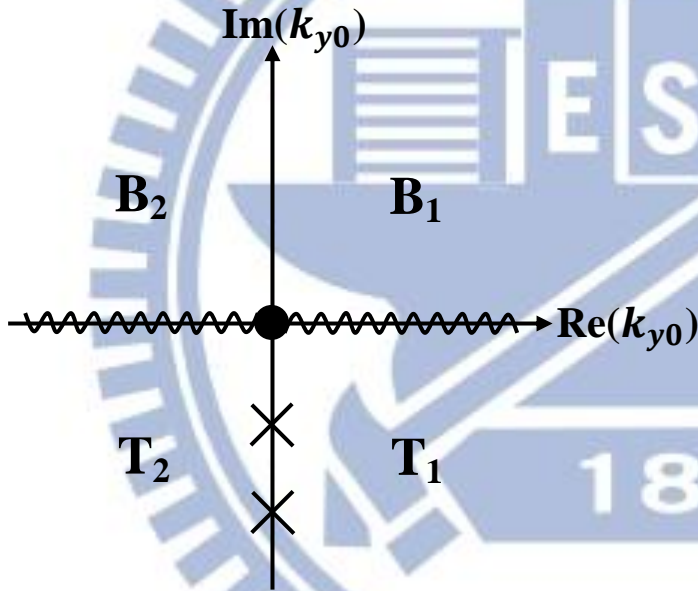
It is easy to see that the expressions for the cutoff frequencies given in Eqs. (D-26) and (D-27) apply also to TE modes. Like the lowest-order ( $n=0$ ) TM mode, **the lowest-order odd TE mode ( $\text{TE}_0$ )** has no cutoff frequency.

Odd TE Modes	Even TE Modes
$f_{co} = \frac{nc}{2h\sqrt{\epsilon_r - 1}}, \quad n = 0, 2, 4, \dots \quad (\text{D-43})$	$f_{ce} = \frac{nc}{2h\sqrt{\epsilon_r - 1}}, \quad n = 1, 3, 5, \dots \quad (\text{D-44})$
where $c = 3 \times 10^8 \text{ m/s}$	where $c = 3 \times 10^8 \text{ m/s}$

## APPENDIX E



**Step1:**



✕ : proper surface wave poles (TM<sub>0</sub>, TE<sub>0</sub>)

● : branch point,  $k_{y0} = 0$

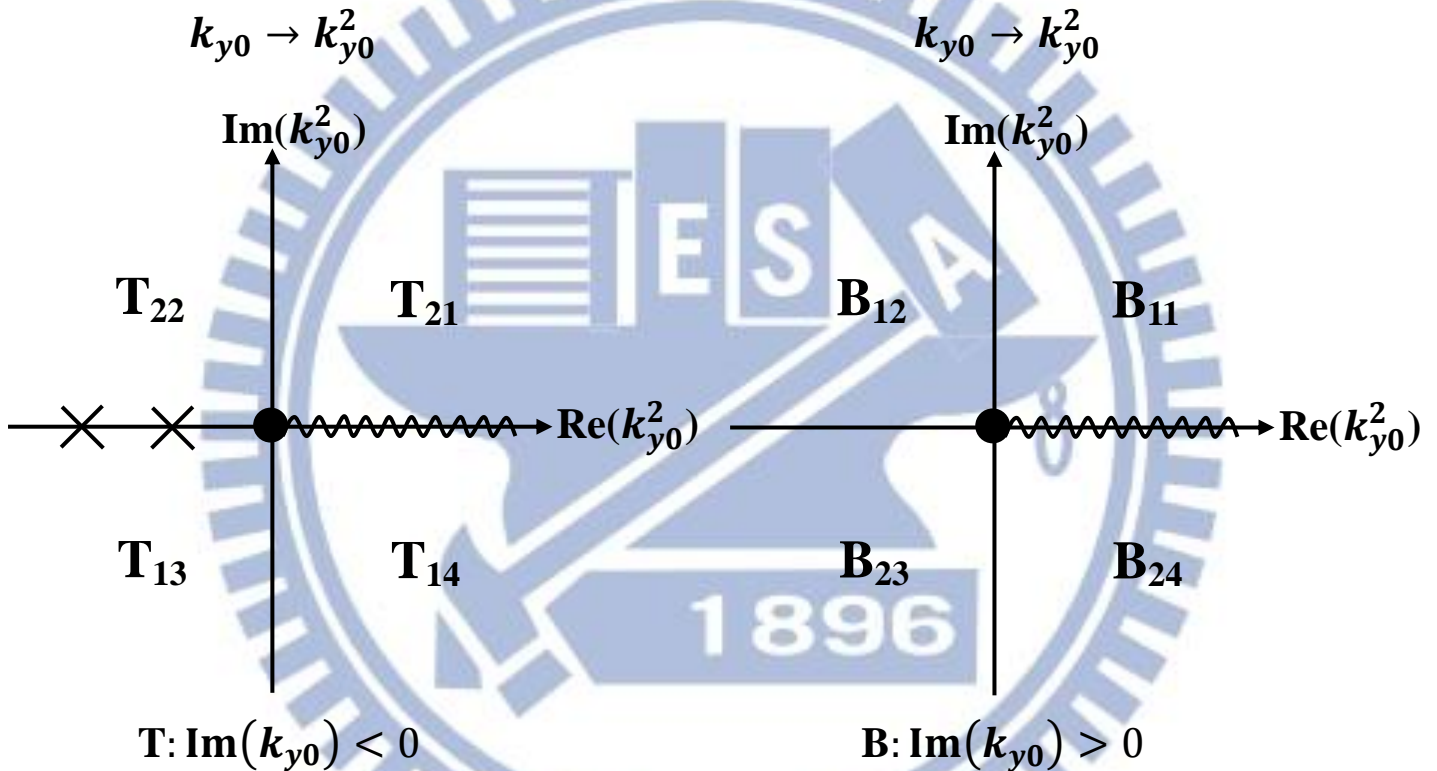
~~~~~ : branch cut,  $\text{Im}(k_{y0}) = \text{Im}\sqrt{k_0^2 - k_x^2 - k_z^2} = 0$

- 1) Let  $\text{Im}(k_{y0}) > 0$ :  $\left| e^{-jk_{y0}y} \right| = \left| e^{-j[\text{Re}(k_{y0}) + j\text{Im}(k_{y0})]y} \right| = e^{\text{Im}(k_{y0})y} \rightarrow \infty$  as  $y \rightarrow \infty$
- 2) Let  $\text{Im}(k_{y0}) > 0$ :  $\left| e^{+jk_{y0}y} \right| = \left| e^{+j[\text{Re}(k_{y0}) + j\text{Im}(k_{y0})]y} \right| = e^{-\text{Im}(k_{y0})y} \rightarrow \infty$  as  $y \rightarrow -\infty$
- 3) Let  $\text{Im}(k_{y0}) < 0$ :  $\left| e^{-jk_{y0}y} \right| = \left| e^{-j[\text{Re}(k_{y0}) + j\text{Im}(k_{y0})]y} \right| = e^{\text{Im}(k_{y0})y} \rightarrow 0$  as  $y \rightarrow \infty$
- 4) Let  $\text{Im}(k_{y0}) < 0$ :  $\left| e^{+jk_{y0}y} \right| = \left| e^{+j[\text{Re}(k_{y0}) + j\text{Im}(k_{y0})]y} \right| = e^{-\text{Im}(k_{y0})y} \rightarrow 0$  as  $y \rightarrow -\infty$

B<sub>1</sub>&B<sub>2</sub>: The E and H fields propagate along the  $\pm y$ -direction and the amplitudes increase exponentially with distance along the direction of propagation, respectively.

T<sub>1</sub>&T<sub>2</sub>: The E and H fields propagate along the  $\pm y$ -direction and the amplitudes decay exponentially with distance along the direction of propagation, respectively.

### Step2:



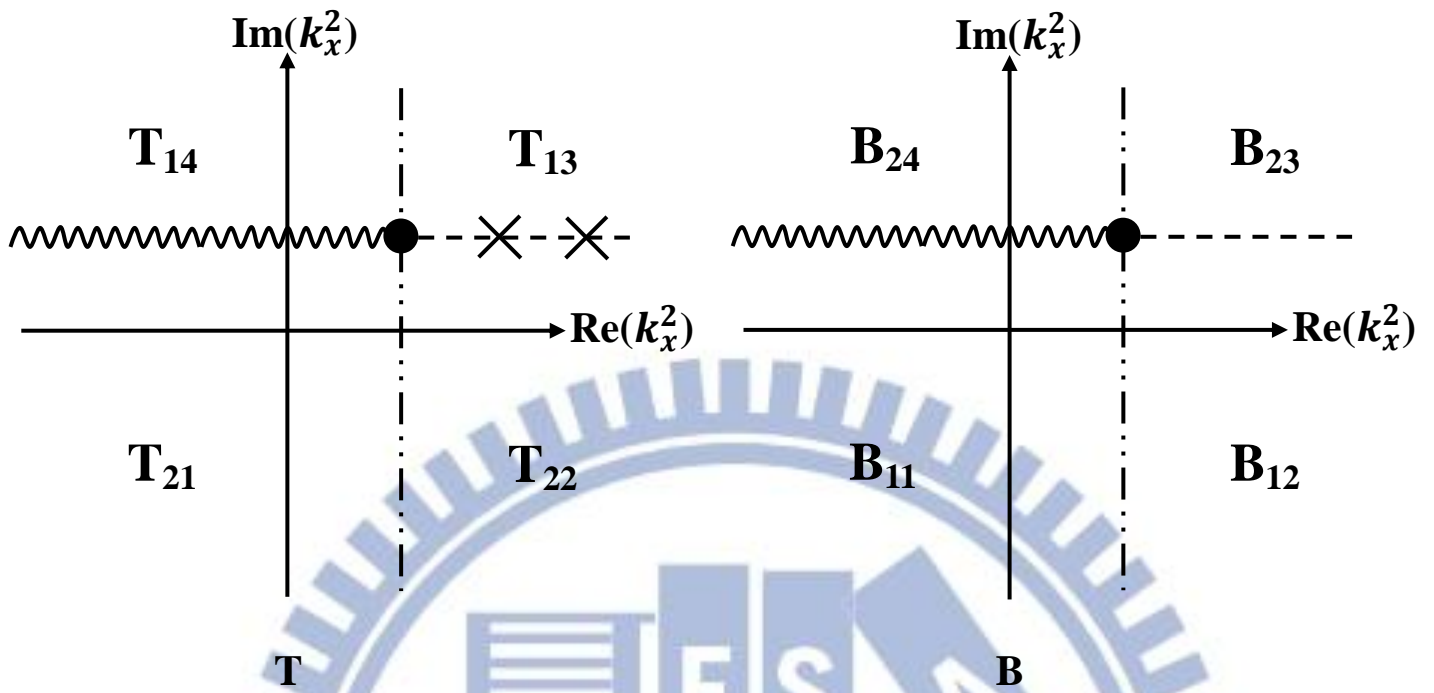
### Step3:

1)  $k_x^2 = k_0^2 - k_{y0}^2 - k_z^2 = k_0^2 - \beta^2 + \alpha^2 - k_{y0}^2 + j2\alpha\beta$ , where  $k_z = \beta - j\alpha$

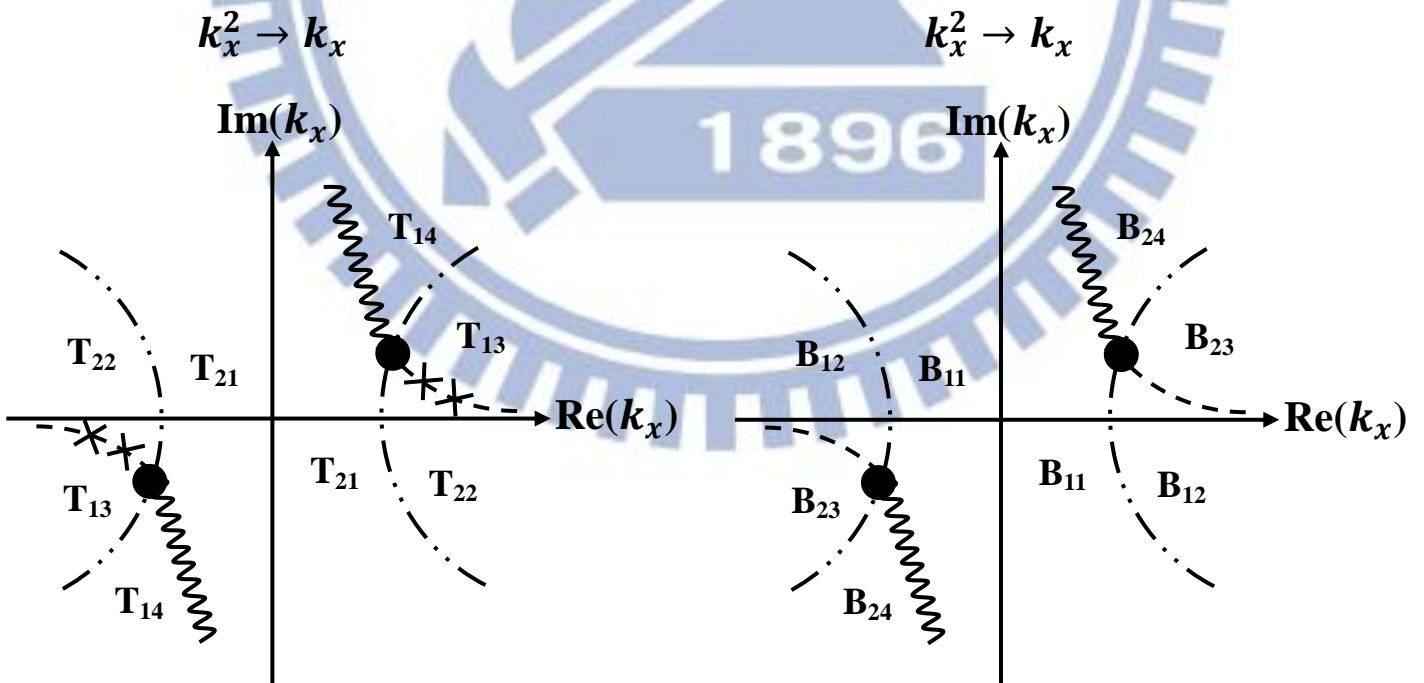
When  $k_{y0} = 0$  (branch point),  $\text{Re}(k_x^2) = k_0^2 - \beta^2 + \alpha^2 > 0$ ,  $\text{Im}(k_x^2) = 2\alpha\beta > 0$

2)  $k_{xp}^2 = k_s^2 - k_z^2 = k_s^2 - \beta^2 + \alpha^2 + j2\alpha\beta$ , where  $k_z = \beta - j\alpha$

$\text{Re}k_{xp}^2 \cong k_s^2 - \beta^2 + \alpha^2$ ,  $\text{Im}(k_{xp}^2) = 2\alpha\beta > 0$



Step4:



Top sheet:  $\text{Im}(k_{y0}) < 0$

Bottom sheet:  $\text{Im}(k_{y0}) > 0$

$T_{13}, T_{14}$ :  $\text{Re}(k_{y0}) > 0$  ;  $T_{21}, T_{22}$ :  $\text{Re}(k_{y0}) < 0$

$B_{11}, B_{12}$ :  $\text{Re}(k_{y0}) > 0$  ;  $B_{23}, B_{24}$ :  $\text{Re}(k_{y0}) < 0$